DYNAMICS OF THE REACTION
$Ba + HI \rightarrow BaI + H$

A DISSERTATION
SUBMITTED TO THE DEPARTMENT OF CHEMISTRY
AND THE COMMITTEE ON GRADUATE STUDIES
OF STANFORD UNIVERSITY
IN PARTIAL FULFILLMENT OF THE REQUIREMENTS
FOR THE DEGREE OF
DOCTOR OF PHILOSOPHY

By
Athanassios A. Tsekouras
June 1992

I certify that I have read this dissertation and that in my opinion it is fully adequate, in scope and quality, as a dissertation for the degree of Doctor of Philosophy.

Richard N. Zare (Principal Advisor)

I certify that I have read this dissertation and that in my opinion it is fully adequate, in scope and quality, as a dissertation for the degree of Doctor of Philosophy.

Wesley D. Allen

I certify that I have read this dissertation and that in my opinion it is fully adequate, in scope and quality, as a dissertation for the degree of Doctor of Philosophy.

Robert Pecora

Approved for the University Committee
on Graduate Studies:

ABSTRACT

The reaction Ba + HI $\rightarrow$ BaI + H was studied under single collision conditions using high resolution laser spectroscopy to determine rotational population distributions of BaI in specific vibrational levels. Laser-induced fluorescence spectra of the BaI $C^2\Pi$ - $X^2\Sigma^+$ (v,v) band system provided the means for measuring the rotational and vibrational excitation of BaI. In the process many low vibrational bands were rotationally assigned and a set of Dunham coefficients was determined from all observed rovibronic transitions that could reproduce all the data. Velocity distributions of the reagents were measured using Doppler spectroscopy for Ba and time-of-flight methods for the supersonic HI beam. The rotational distributions for BaI (v=0) peaked at J=420 for center-of-mass collision energies of 30 kJ mol^{-1} achieved under crossed-beam conditions. Rotational distributions of BaI(v) for v=0, 4, 8, 12, 16, 18 formed under beam-gas conditions were found to peak at J=438, 286, 220, 150, 127, and 106 respectively. The corresponding full-width-at-half-maximum was approximately 150.

The above reaction is the prototypic example of a kinematically constrained system where the mass combination of reagents and products requires that all reagent angular momentum appear as rotation of the diatomic product. The reagents carry orbital angular momentum because of their relative motion which is the product of their reduced mass, their relative velocity, and the impact parameter of the collision. Thus impact parameter values leading to the formation of BaI in the vibrational levels listed above were determined. The impact parameter distribution for the formation of BaI (v=0) was found to peak at 4.5 Å with a very small spread. Higher vibrational levels arose from lower impact parameters with larger spreads indicating a strong correlation between impact parameter and product vibrational state.

Table of Contents

Chapter 5. BaI Product State Distributions

Chapter 6. Specific Opacity Functions

List of Tables

List of Figures

PREFACE

The present thesis contains the distillate of more than four years of work in the Zarelab at Stanford. Left out of this volume are all the human interactions and emotions caused by daily progress and setbacks. The reader will not find information on how a disaster on the experimental apparatus is dealt with or how the same system is induced in generating exciting results. This kind of information can not be included in a strictly scientific publication. Suffice it to say that all happy and bad moments of a graduate student career are not to be missed.

A brief word about the people who made this work possible is most appropriate here. From the very beginning it did not take Dick Zare a lot of effort to convince me how exciting the project I had decided to work on was. Since then he has always been a source of inspiration and encouragement. Not one of his least achievements is that of bringing together in his research group a number of nice people and good scientists. As mentioned by all contemporary members of the group, Pat Vaccaro, a postdoctoral fellow, was the best example of these unique individuals. I was fortunate to work with him on the same project for more than two years and benefited in many respects from that collaboration. During the same time, Daqing Zhao, a graduate student, complemented our efforts in the experiment. Later, I had a very pleasant and fruitful cooperation with Christine Leach who was a postdoctoral fellow in our group. Finally, for the last year I enjoyed working with Kostas Kalogerakis who, apparently, will be able to experiment under progressively more sophisticated conditions so that he will not get the chance to study a different reaction system.

Work in the lab also defined to a large extend many aspects of life as a whole. Interactions with other members of the group were amicable and discussions with them useful. To single out specific people would do injustice to the others. The enumeration of key elements to my life in graduate school would not be complete without mentioning the people and the facilities of Stanford University which made life easier and more enjoyable. From a longer distance, but only physically so, I experienced the continuous support from my parents and my family. To all these people I express my thanks for helping me complete my graduate studies.

Chapter 1. Introduction

Reaction Dynamics

Gas-phase reaction studies has been a very powerful tool for the investigation of elementary processes of simple or complex systems. Since the first crossed-beam experiment [1] in 1954, the methods for reagent preparation and product detection have advanced considerably. The invention and fast development of lasers has played an important role in both aspects of the experiments. The different quantities controlled or measured in a reaction vary from detailed knowledge of the energy content of a molecule or a cluster to their average orientation or specific mode excitation. The goal of all experiments is to determine a reaction cross section under certain conditions or constraints usually included in the term "state-to-state" reaction dynamics.

The low pressure conditions achieved in a vacuum apparatus provide an ideal environment with the least possible interferences from multiple processes, energy quenching, and wall reactions. The disadvantage often associated with low pressures is very small product yield which requires the implementation of very sophisticated detection equipment. Complex hardware as a rule in research is custom designed. The more equipment needed to conduct an experiment, the more prone it is to fail. Despite all problems the field of reaction dynamics is evolving and advancing thanks to the persistence of researchers and the advancement of technology.

One quantity associated with a reaction process is the impact parameter. It is a measure of how closely one reagent molecule needs to be targeting the other molecule for the reaction to occur. It is not the absolute distance at which the molecules start interacting; almost certainly the impact parameter is shorter than the initial interaction distance otherwise no reaction would occur. This quantity cannot be controlled in a gas-phase reaction because the position of the molecules is only known macroscopically. The impact parameter cannot be measured either because of its size, which is expected to be of the order of a few Ångstrom. It is related to the angular momentum of the reaction system as will be discussed in detail in Chapter 6. Both the impact parameter and angular momentum are invariants of an isolated system, but the impact parameter changes magnitude when the chemical transformation occurs, because it is defined with respect to a certain pair of particles.

The angular momentum after the reaction can be determined with the exception of the portion related to the recoil of the products. A reaction can be chosen to suppress the latter quantity [2]. Such a system should belong to the family of reactions symbolically written as

$$\mathrm{H} + \mathrm{H'L} \rightarrow \mathrm{HH'} + \mathrm{L} \tag{1.1}$$

where H and H' are heavy atoms and L is a light atom.

One reaction of this kind is the reaction

$$\mathrm{Ba} + \mathrm{HI} \rightarrow \mathrm{BaI} + \mathrm{H} \tag{1.2}$$

The work presented in this dissertation is exclusively devoted to the study of this reaction. The ultimate goal was to determine the impact parameter dependence for the formation of specific product states.

The same reaction has been studied by different research groups a few times in the past 20 years. The first work [3] made use of crossed-beams and was based on mass spectrometric detection of the products. It provided information on product angular distribution but not the internal states of the products. Shortly after, another crossed-beam study [4] that made use of the then new technique of laser-induced fluorescence (LIF) was able to provide a crude product vibrational distribution. More recently, this reaction was studied under beam-gas conditions with the explicit intention of determining the impact parameter dependence of product formed in the $v = 8$ vibrational level [5]. That study concluded that the quantity sought was 2.6 Å with a width of 1 Å.

Our study is the cross-beam evolution of the previous work. It covered many product vibrational levels and used diverse collision conditions. Chapter 2 describes in great detail the apparatus used in the experiments. The quality of the particle beams generated in the vacuum chamber was measured in detail as shown in Chapter 3 because of the importance of the reagent velocities in the data analysis. The tool for the measurement of populations of BaI internal states was the BaI C -X electronic transition. Our contributions in that field, that were an indispensable byproduct of our reactive studies, are included in Chapter 4. The main body of our results consists of rotational state distributions for BaI product molecules in several virational levels; these results are presented in Chapter 5. Their analysis in Chapter 6 allowed us to determine the values of the collision impact parameter that gave products in specific vibrational levels.

References

1 E. H. Taylor and S. Datz, *J. Chem. Phys.* **23**, 1711 (1955).

2 D. R. Herschbach, *Faraday Discuss. Chem. Soc.* **33**, 281 (1962); D. R. Herschbach, *Adv. Chem. Phys.* **10**, 319 (1966).

3 C. A. Mims, S.-M. Lin, and R. R. Herm, *J. Chem. Phys.* **57**, 3099 (1972).

4 H. W. Cruse, P. J. Dagdigian, and R. N. Zare, *Farad. Disc. Chem. Soc.* **55**, 277 (1973)

5 C. Noda, J. S. McKillop, M. A. Johnson, J. R. Waldeck, and R. N. Zare, *J. Chem. Phys.* **85**, 856 (1986).

Chapter 2. The Apparatus

Introduction

All our experiments were conducted in a newly constructed, crossed-beam reaction chamber [1]. A laser system was used to electronically excite BaI molecules or Ba atoms. The fluorescence detection system comprised of optics and electronics that varied with the detection scheme. A chopper/mass spectrometer combination coupled with the necessary electronic equipment was used to monitor the supersonic HI beam. Each part of the apparatus is described below in detail. An approximate perspective view of the whole laboratory configuration is shown in Fig. 2.1.

Vacuum System

The vacuum system was an assembly of eight differentially pumped, interconnected chambers grouped in four units to accomplish different functions. The four units were the main reaction chamber, the HI beam source, the Ba beam source, and the mass spectrometer chamber. A cross section of the system is shown in Fig. 2.2.

Main Scattering Chamber

The main scattering chamber consisted of an 18"-diameter stainless steel cylinder with o-ring sealed flanges providing vacuum integrity at the upper and lower surfaces (see Fig. 2.2). Background pressures of approximately 5×10^{-8} Torr were achieved by evacuating the vessel with a liquid-nitrogen-baffled 6" diffusion pump (Varian VHS-6). This pumping system was mounted directly onto an 11" ASA tee piece that served to connect the main chamber to a differentially pumped quadrupole mass spectrometer utilized for HI beam analysis. A liquid-nitrogen trap located within the scattering region provided additional pumping speed for condensable reagent gases (e.g., HI). This

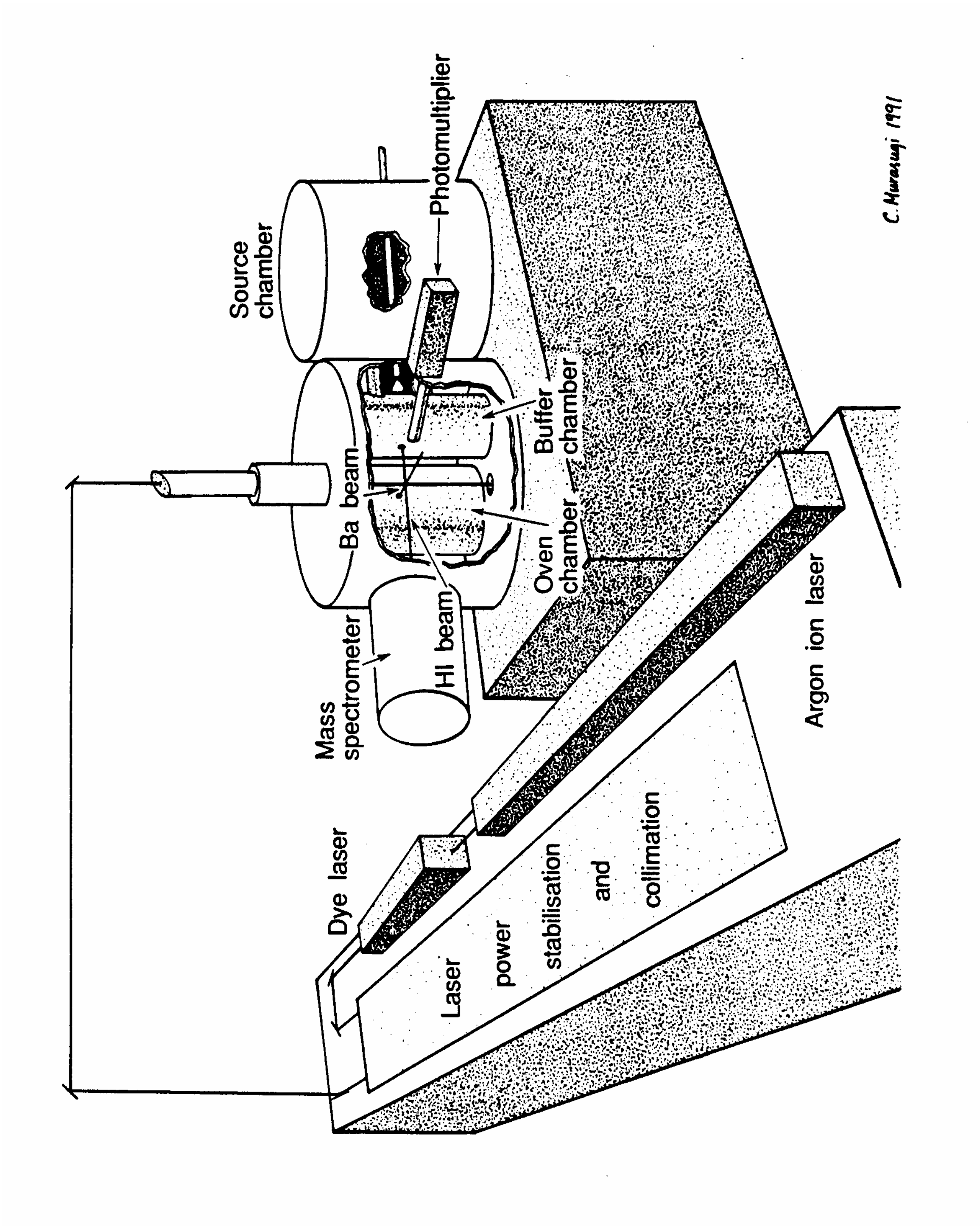

Figure 2.1. Artist's rendition of the laboratory configuration. [Reproduced with kind permission from the artist.]

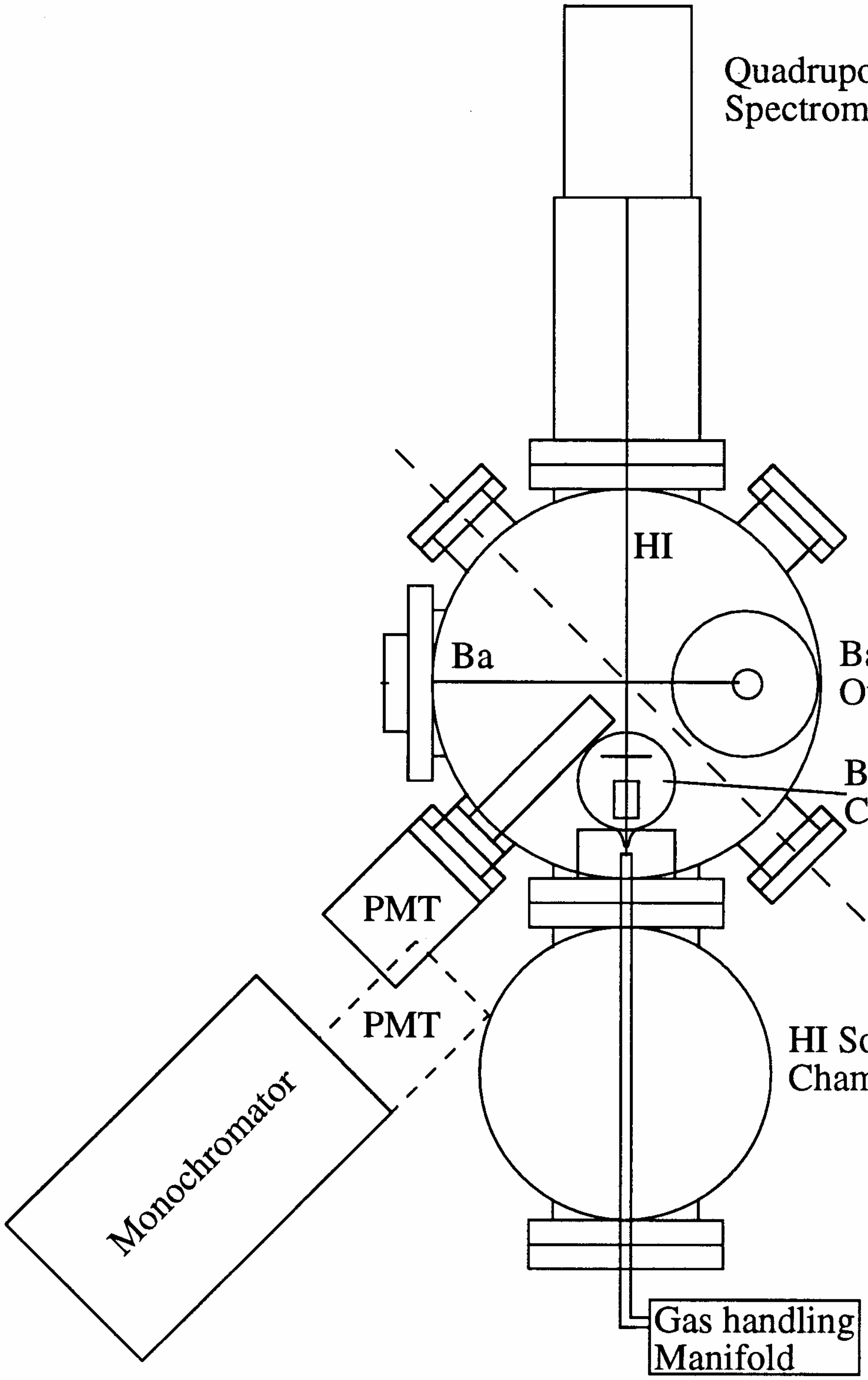

Figure 2.2. The Ba + HI reaction chamber. The probe laser beam intersects the plane of the figure at the crossing point of the two particle beams.

configuration enabled the pressure to be maintained in the low 10^{-6} Torr range when experiments were done under crossed-beam conditions.

The Ba and HI sources were each collimated to yield beams of circular cross section that exhibited a nominal diameter of 1.0 cm at their point of mutual intersection (i.e., at the center of the main scattering chamber). Product molecules formed within the 0.7 cm^3 interaction volume were directly probed by means of a high-resolution laser. For the purpose of conducting beam-gas experiments a needle valve was attached to the side of the chamber to deliver HI at very low flow rates from a HI lecture bottle at 195 K. The pumping speed of the diffusion pump was reduced by throttling a gate valve separating the pump from the tee piece.

The chamber was equipped with several windows. Two, located at 94 cm above and below the center plane, were mounted at the end of triply baffled arms at Brewster's angle to allow the propagation of the probe laser beam with a minimal amount of scattered light [2]. One window was used for general inspection of the interior of the chamber. A second set of windows, located on the center plane, was used for the propagation of a laser beam in the plane of the molecular beams and the detection axis. The optical detection system was mounted in the center plane at the end of a recessed tube to provide close approach to the fluorescing region.

HI Reagent Source

Sample gas manipulations for the HI source were performed entirely in a custom stainless steel and tantalum manifold. This apparatus, continuously maintained at low pressures through use of a liquid-nitrogen-and molecular-sieve-trapped mechanical pump, was thoroughly baked out (at approximately 420 K) prior to each experiment. Hydrogen iodide was obtained commercially (Matheson) with 98% minimum purity and subjected to several freeze-pump-thaw cycles with liquid nitrogen to remove H_2 formed by the decomposition of HI. The temperature of the HI vessel was subsequently maintained at 273 K, in order to condense the I_2 contaminant, while a preselected quantity of hydrogen iodide vapor was permitted to enter a 1-gallon reservoir (Whitey). Nitrogen (Liquid Carbonic; 99.998%) and/or helium (Liquid Carbonic; 99.995%) and/or argon (Liquid Carbonic; 99.998%) was then admitted to the manifold to prepare the desired seed-to-carrier concentration ratio (typically approximately 6% HI). The long duration of individual experimental runs performed during our studies (18 ± 10 hours), in conjunction with the continuous nature of the supersonic source, required the limited volume of the reservoir to be filled to total pressures as high as 1000 psig. With the reservoir sealed off from the rest of the manifold, the enclosed gas sample was vigorously mixed through use of a magnetically coupled, teflon-coated stirring bar. The HI mixture subsequently passed through tandem, single-stage regulators (Matheson), designed to maintain a preset stagnation pressure (typically 250 kPa absolute), and a 15-μm high-flow, in-line filter (Nupro) before entering the tantalum tube of the nozzle assembly.

The HI supersonic nozzle consisted of a 100-μm-diameter tantalum aperture (Ted Pella, Inc.) that had been carefully welded onto a length of tantalum tubing. Where possible, tantalum was selected as the material of choice for construction because of its superior resistance to corrosion by hydrogen halides [3]. The source assembly was designed to permit three-dimensional translation, from outside the vacuum, with respect to the 0.98-mm-diameter orifice of a molecular beam skimmer (Beam Dynamics). The nozzle was typically heated to 323 K by means of thermocoax (Amperex) tightly wrapped around the final 8-cm portion of its tip. Stagnation temperatures were regulated to ±1 K through a microprocessor-based controller (Omega; CN 9000) that utilized a metal-clad thermocouple, inserted directly into the nozzle tube, as a feedback sensor.

The chamber housing the supersonic HI source was evacuated by a water-baffled 10" diffusion pump (Varian; VHS-10 with Dow Corning 705 oil) that was backed by a two-stage mechanical pump (Sargent-Welch 1398). Liquid-nitrogen-filled cold traps were incorporated into all vacuum forelines to prevent the contamination and subsequent deterioration of mechanical pump fluid by the highly corrosive HI reagent. Once skimmed, the HI beam propagated through a buffer region, pumped by a water-baffled 4" diffusion pump (CVC PMCS-4B),which provided for differential pumping between the source and main scattering chambers. This differentially pumped region also contained a mechanical chopper that could be rotated into the beam for both TOF velocity measurements and, when desired, lock-in detection of BaI laser-induced fluorescence signal (i.e., based on phase-sensitive demodulation of the chopped Ba + HI reaction yield). Collimation of the HI source to its final half-angle of 1.18^o was performed by a circular aperture located on the exit face of the buffer chamber. Typical background pressures were in the mid-10^{-8} Torr range. Under operating conditions appropriate for a mixture of 6 % HI in N_2, the source and buffer chamber pressures increased to roughly 10^{-4} and 10^{-5} Torr, respectively, while pressures in the main scattering vessel remained in the high 10^{-7} to low 10^{-6} Torr scale.

The beam chopper housed in the buffer chamber was mounted on a rotatable top flange. The custom designed mount was made out of nickel-plated copper and provided mechanical support, heat sinking, and electrical connections to the motor located at the bottom of the mount. A small a.c. hysterisis motor (TRW Globe type SC 115 V 2-phase) designed to operate at 400 Hz was used to turn a thin (0.13 mm, 3" diameter) beryllium-copper chopper blade at 300 Hz. Power was provided from a sine wave generator (Krohn-Hite; model 4200), amplified by an audio amplifier (Realistic; MPA-25 20 W), and its voltage doubled by a step-up transformer (Stancor; P8603). The second phase required was generated by using a matched capacitor. After brief application of as high a voltage as 90 $V_{a.c.}$ for initial acceleration the operating voltage was set in the range 30 - 40 $V_{a.c.}$ which provided more even rotation and caused less pick-up noise to the photodiode monitoring the position of the chopper blade than the high drive voltage value did. Two designs of blades were built. One, used for HI time-of-flight (TOF) [4] measurements, had two narrow (1 mm wide), antipodal slits to allow the propagation of short gas pulses. The other had 8 slits that provided a 50 % duty cycle. The disadvantage of using the 8-slit blade was that the HI beam velocity distribution could not be determined, because no meaningful TOF spectrum could be recorded. A high brightness, directional light-emitting diode (Hewlett-Packard; HLMP-0363) and a photodiode (EG&G Photon Devices; FFD-200 without window) were located one on each side of the plane of the blade at a position symmetric of the supersonic beam path with respect to the blade axis. The photodiode signal indicated the position of the blade and was used as a trigger for timing the HI pulses or for phase-sensitive detection of the BaI fluorescence signal.

The source configuration had a total distance from nozzle orifice to interaction region of approximately 20 cm and produced a flux of roughly 10^{17} particles cm^{-2} s^{-1} as measured for a pure beam of N_2. Mass spectrometric analysis of the HI-seeded beam revealed no significant concentration of HI dimers, regardless of variations in either the ionization current (0 - 20 mA) or the electron bombardment energy (3 - 100 eV) employed for creation of the measured ion signal. Possible contamination of the HI source with residual I_2 was examined through the use of high-resolution LIF spectroscopy. No evidence for this impurity was found, despite spectral searches performed over a wide range of rovibronic transitions in the I_2 $B^3\Pi_{0_u^+}$ - $X^1\Sigma_g^+$ system.

Ba Reagent Source

The Ba source utilized in our studies was essentially a modified version of the high-temperature oven previously described by Rettner, Wöste, and Zare [5]. A cylindrical stainless steel crucible, with a 0.8-mm-diameter orifice, was filled with approximately 60 g of barium rod (Alfa; 99.5% purity) and sealed by means of a tapered, press-fitted cap. Great care was taken to remove any residual oxide coating from the barium metal prior to its use. This greatly alleviated orifice clogging problems that were believed to stem from the presence of such refractory oxide material. Three 1/8"-diameter ceramic rods served to support the barium-containing vessel above a water-cooled and radiatively baffled baseplate. This entire assembly was designed to be rotated and translated from outside the vacuum to permit fine positioning of the Ba source. Oven temperatures were measured via a W/5% Re vs W/26% Re thermocouple (Omega; type C) that was inserted through one of the supporting ceramic rods to a point within 1 mm of the crucible orifice. Oftentimes, temperature readings were obviously in error and lower than the expected value. This effect was attributed to poor electrical contact between the thermocouple wires and their extensions; exposure of these contacts to high temperatures created secondary thermocouples.

The barium crucible assembly was placed into a high-temperature furnace consisting of three cylindrical layers of tantalum sheet surrounded by a water-cooled copper jacket. The tantalum functioned as a heat shield designed to contain and distribute thermal radiation within the oven. Three tungsten hairpin filaments (1.5-mm diameter), driven by a high-current/low-voltage a.c. supply (Allen-Jones Electronics) to eliminate discharge-related formation of metastable atoms [6], served to radiatively heat the crucible and vaporize the barium metal. Wired in parallel via a water-cooled and radiation-baffled connector block, the filaments produced the requisite operating temperature of approximately 1320 K with input powers typically of the order of 1 kW (at 5.6 $V_{a.c.}$). A hole cut through both the tantalum heat shields and the outer water jacket enabled the resulting Ba beam to emerge from the furnace assembly. In order to minimize corrosion problems, such as those that might stem from contact with the HI reagent, all copper components of the metal atom source were electrolytically plated with nickel.

As shown in Fig. 2.2, the Ba source was housed in a differentially pumped, cylindrical partition that was situated directly within the confines of the main scattering chamber. This configuration ensured that the total distance from crucible orifice to interaction region was kept to a bare minimum (i.e., 10.6 cm). Evacuated by means of a water-baffled, 4" diffusion pump (CVC PMCS-4B), the source chamber exhibited a background pressure of roughly 10^{-8} Torr. Following an initial period of outgassing, operating pressures within this region could readily be maintained in the 10^{-6} to 10^{-7} Torr range.

Before entering the main scattering chamber, the atomic beam produced by the Ba source was collimated to a half-angle of 2.82° via a custom-made set of apertures and baffles. Designed primarily with our fluorescence product detection scheme in mind, this configuration of baffles also served to trap a considerable portion of the unwanted blackbody radiation emerging from the high-temperature oven. After traversing the Ba + HI interaction region, the barium atoms impinged upon a conical catcher block that could by manually rotated into and out of the beam path. The latter position, in conjunction with a judiciously placed optical viewport and precision telescope, permitted line-of-sight alignment of the barium crucible orifice with respect to the baffle assembly. Typical Ba beam fluxes, estimated on the basis of experimentally measured velocity distributions and an assumed vapor pressure of roughly 10 Torr [7] for barium at 1320 K, were on the order of 10^{16} - 10^{17} particles cm^{-2} s^{-1}. Ba_2 has been observed in a BaS beam at very high temperature (2100 K) [8] and in excimer states in a Ba oven [9]. While not explicitly examined, barium dimerization seems to be highly unlikely due both to the mild expansion conditions employed for our “effusive” source and to the closed-shell nature of Ba atoms.

Mass Spectrometer and Associated Electronics

A flange-mounted quadrupole mass spectrometer (Extrell) was used to monitor the HI beam. Two stages of differential pumping ensured that the pressure in the mass spectrometer always remained in the 10^{-8} torr range. The first stage of differential pumping was accomplished with the use of a 4" diffusion pump (Edwards; Diffstac 63-

150 charged with Santovac 5 oil). This chamber was connected to the tee piece through a 0.750-µm platinum aperture (Ted Pella, Inc.; 60750) and to the mass spectrometer chamber through a 2-mm aperture. The second chamber was evacuated by a turbomolecular pump (Leybold-Heraeus; Turbovac 150 CVS) backed by a molecular-sieve-trapped mechanical pump.

The mass spectrometer consisted of an electron-impact ionizer, a quadrupole with 200-mm-long, 9.5-mm-diameter rods, and a Channeltron electron multiplier (Galileo; 4816). Typical values for the electrical settings were 15 mA for ionization electron current, 100 V for the electron acceleration, 25 V for the ion acceleration, and 1500 V for the detector. The ion signal was coupled into a high-speed, high-gain transimpedance amplifier (Keithley 427) before being directed to the input stage of a gated integrator/boxcar averager (EG&G PAR 162 with 164 integrator modules). TOF spectra were obtained by utilizing a microcomputer (Apple IIe) to scan the boxcar gate repetitively over a preselected time interval. Timing of these scans was triggered by the photodiode monitoring the chopper position. Absolute time calibration was provided by a concurrently digitized train of 50-µs-long pulses from a pulse generator (Hewlett-Packard; 8011A).

Laser System

The spectroscopy of BaI needs to be done at very high resolution to allow the determination of intensities of individual rovibronic transitions. This resolution is provided only by continuous-wave lasers. The excitation source for our LIF detection scheme was provided by a single-mode, actively-stabilized, cw ring dye laser (Coherent 699-29) containing Rhodamine 560 dye (Exciton) dissolved in ethylene glycol. An integral wavemeter, in conjunction with computer-controlled frequency scanning and data acquisition, enabled high-resolution, continuous-stream spectra to be recorded over essentially the entire tuning range available to a given dye. Pumped by approximately 6.1

W of the 5145 Å emission from a mainframe argon-ion laser (Spectra Physics 171-17), this configuration produced a peak output power of 1.2 W with an actively stabilized linewidth specified to be less than 1 MHz. Single-frequency operation of the dye laser was continuously monitored by means of a 2-GHz scanning interferometer (Spectra Physics 470).

While the normal tuning range of Rhodamine 560 dye was more than adequate for the majority of our BaI studies, measurements performed on the high vibrational levels of the $C^2\Pi$-$X^2\Sigma^+$ $\Delta v=0$ sequence required that the peak of the laser curve be shifted to the blue. This was accomplished by careful addition of a saturated KOH/methanol solution to the dye mixture. Dye half life, determined to be on the order of 150-200 Watt-hours, was greatly enhanced by replacing all brass components in the commercial dye circulator with comparable parts made from stainless steel and teflon.

The dye laser power was maintained at a constant preset value (± 0.5 %; d.c. to 3 kHz bandwidth) by means of a homemade active stabilization system based on a servo-locked acousto-optic modulator (IntraAction AOM-40). The intensity of the undeflected laser beam (zero order of the AOM) was adjusted by varying the depth of modulation of the AOM grating. A Keplerian telescope/spatial filter assembly served to expand and collimate the output light while simultaneously converting any movements in beam position, such as those that might accompany frequency scanning, into amplitude fluctuations that could subsequently be corrected for by the power stabilization loop. This optical configuration provided a source of tunable cw radiation that exhibited superior amplitude and frequency stability, as well as an exceptionally uniform Gaussian spatial profile (approximately 0.8-cm diameter). Following attenuation by a pair of polarization cubes (Karl Lambrecht), the probe light propagated through the Ba + HI interaction region in a direction perpendicular to the plane defined by the crossed reagent beams (see Fig. 2.3).

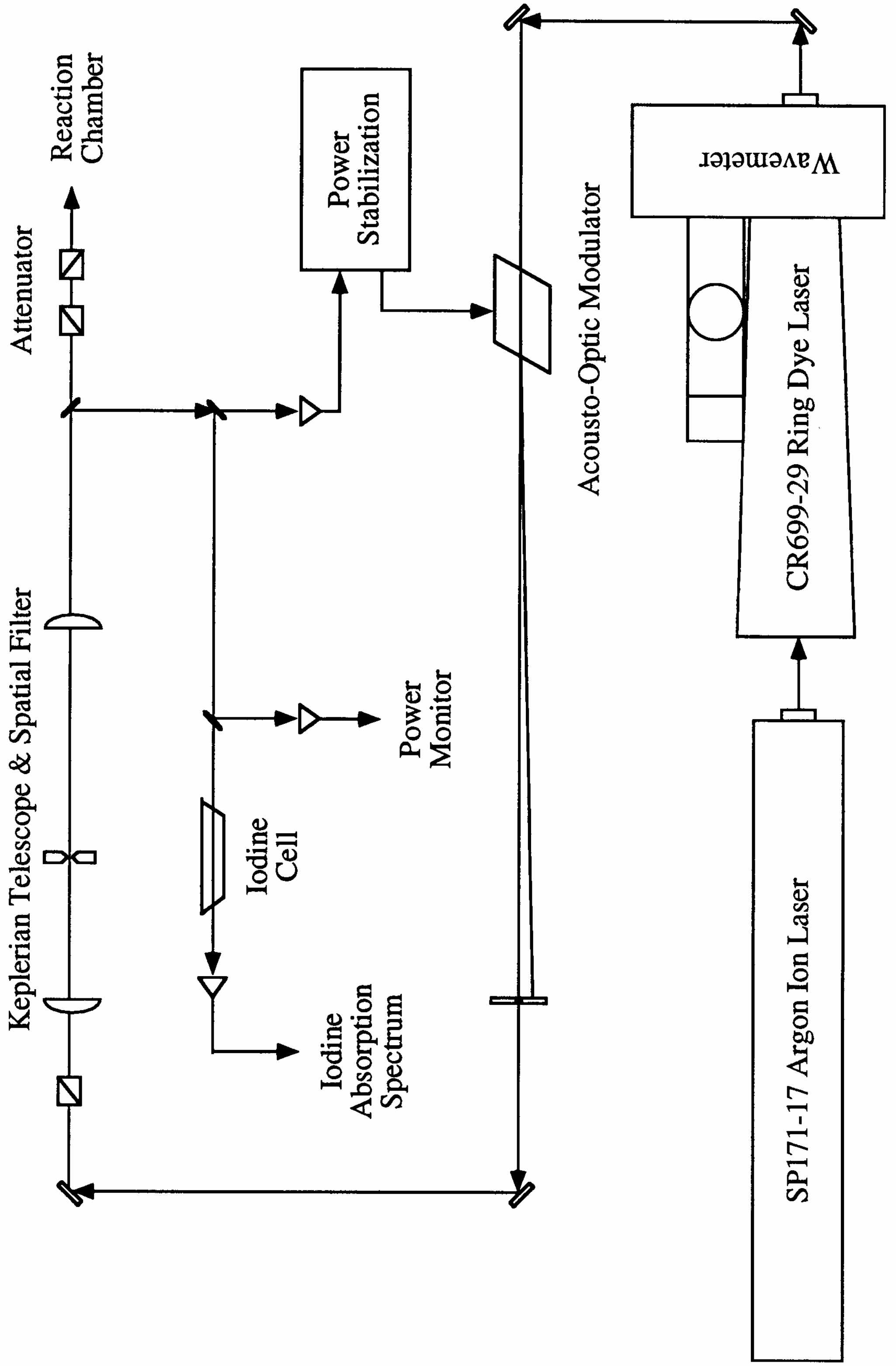

Figure 2.3. Probe laser beam source.

In order to minimize saturation effects in the observed BaI $C^2\Pi$ - $X^2\Sigma^+$ transitions, the intensity of the probe laser entering the reaction chamber was typically attenuated to less than 10 mW. The direction of linear polarization for the LIF excitation beam could be readily varied through appropriate adjustment of the optics employed in the polarization-based light attenuator.

LIF Detection Optics and Electronics

A set of three (30-mm diameter) closely-spaced lenses was located 4.5 cm away from the center of the reaction chamber to collect light in a solid angle with 20^o half angle. BaI fluorescence was imaged on a rectangular slit to reject any unwanted background light (e.g., from the oven) and was recollimated appropriately to traverse a narrow bandpass filter. In the case of crossed-beam experiments when total fluorescence was monitored, an interference filter was used to admit light of wavelength similar to that of the BaI spin-orbit subband excited (Oriel; 5600-2-4779-CC or 57180 #5) or the emitting Ba transition (Ditric Optics; D.D. 15-30190 YRR 9-8). In the case of beam-gas experiments, the fluorescence was imaged at f/7 on the entrance slit of a 1-m monochromator (Interactive Technology; model CT 103, 11.6 x 13.6 cm grating with 1200 gr mm^{-1}) (SDLIF measurements). The imaging sharpness was checked by visual inspection of the image of the interaction region being illuminated by Ba $^1P^o$ - ^1S LIF. In both cases light was converted to electrical signal with a cooled photomultiplier tube (PMT) (Centronic Q4283 RA at -20 ^oC) biased by a high voltage power supply (Pacific Photometric Instruments; model 204) in the range 1000 -1700 V.

Undispersed fluorescence was monitored with lock-in detection (PAR 124A with 116 preamplifier), based on modulation of either the probe laser or the HI source, that enabled the LIF signal to be effectively discriminated from residual background noise.

For our studies, the major noise source was found to entail blackbody emission from the high-temperature barium oven. Signal limitations required that SDLIF signal be monitored with a photon counting system which consisted of a 10x fast preamplifier (Ortec 9301), a timing-filter amplifier (Ortec 454) used at its non-modulating mode to amplify the signal 20 times, a discriminator (Ortec 436) set usually at 83 mV, and a ratemeter (Ortec 449-2). The output signal from either piece of equipment was amplified by a custom made, medium-speed, variable-gain, three-channel amplifier and sent to one of the three analog input channels of the computer (Apple IIe) controlling the dye laser.

BaI excitation spectra were obtained by scanning the laser frequency under computer control while simultaneously digitizing and recording the processed output of the photomultiplier tube. Concurrent measurement of the I_2 absorption spectrum provided a convenient absolute frequency reference when used in conjunction with the Fourier transform atlas of Gerstenkorn and Luc [10].

Monochromator transmission spectra were recorded every time the monochromator settings were changed. Typically, the entrance and exit slits were set to a width of 250 μm and the maximum available entrance slit height was used, viz., 50 mm, because it did not increase the bandwidth of the spectrum while providing maximum transmission intensity. These spectra were generated by scattering a very weak, diffuse laser beam off a black baffle situated in front of the Ba source chamber. The center of the scattering target was in the line of sight of the LIF collection optics and very close to the reaction region. The PMT signal was monitored by phase-sensitive detection. Separate tests were performed to check that this detection scheme could determine the true transmission spectrum. Ba $^1P^o$ - ^1S LIF was used successfully to confirm both the position and the shape of the transmission peak.

References

1 P. H. Vaccaro, D. Zhao, A. A. Tsekouras, C. A. Leach, W. E. Ernst, and R. N. Zare, *J. Chem. Phys.* **93**, 8544 (1990).

2 J. G. Pruett and R. N. Zare, *J. Chem. Phys.* **64**, 1774 (1976).

3 W. Braker and A. L. Mossman, "Matheson Gas Data Book," Matheson Gas Products, Secaucus, 1980.

4 D. J. Auerbach, Velocity Measurements by Time-of-Flight Methods, in "Atomic and Molecular Beam Methods," G. Scoles, ed., Oxford University Press, New York, 1988.

5 C. T. Rettner, L. Wöste, and R. N. Zare, *Chem. Phys.* **58**, 371 (1981).

6 R. C. Estler and R. N. Zare, *Chem. Phys.* **28**, 253 (1978).

7 H. Hartmann and R. Schneider, *Z. Anorg. Allgem. Chemie* **180**, 275 (1929); *Industrial and Engineering Chemistry* **39**, 517 (1947); "CRC Handbook of Chemistry and Physics," CRC Press, Boca Raton, 1984.

8 R. M. Clements and R. F. Barrow, *J. Chem. Soc. Faraday Trans. 2* **81**, 625 (1985).

9 D. Wu, Y. Yang, and G.-z. Lu, *Chinese Physics* **10**, 181 (1990).

10 S. Gerstenkorn and P. Luc, "Atlas du Spectre d'Absorption de la Molécule d'Iode," Centre Nationale de la Recherche Scientifique, Paris, France, 1978; S. Gerstenkorn and P. Luc, *Rev. Phys.* Appl. **14**, 791 (1979).

Chapter 3. Reagent Velocity Distributions

Introduction

The characterization of the beam velocities was of great importance to our studies. The conservation principles of both energy and angular momentum play a central role in the interpretation of the experimental data. Both are directly related to the relative velocity of the reagents. The relative velocity can be calculated from the three-dimensional reagent velocity distributions. In addition, the magnitude of the reagent velocities determines the velocity of the center of mass of the collision pair, which relates directly to the velocity of the reaction products. Although theoretical models exist to predict the velocity distribution of an atomic or a supersonic beam, they are not accurate enough and, as will be shown below, may be in error on the shape of the distribution. The objective of this chapter is to describe how we were able to determine experimentally the velocity distributions of the reagents Ba and HI and how the relative velocity distribution was constructed.

The Ba Beam

The first-order Doppler effect can be used to determine the projection of the velocity of a particle along the laser propagation direction, because [1]

$$\omega = \omega_0 + \mathbf{k} \cdot \mathbf{v} \tag{3.1}$$

where ω is the observed cyclic frequency of a transition, ω_0 is that for a stationary particle, $\mathbf{k}$ is the light wave vector, and $\mathbf{v}$ is the velocity of the particle. When a well-collimated beam of particles intersects a laser beam at right angles, $\omega = \omega_0$ and no shift is observed in the absorption or LIF spectrum of the particles. When a monoenergetic, collimated beam intersects the laser beam at an angle other than 90^o, the previous spectrum will appear shifted by the amount $\mathbf{k} \cdot \mathbf{v}$. If the beam velocities follow a distribution that is not a δ function, the spectrum will appear broadened, but its peak value will be shifted with respect to the spectrum observed at 90^o of incidence. Such a spectrum we expect to see when we cross the Ba beam with a laser beam at 135^o. The resultant spectrum is the convolution of the Doppler-free spectrum and the beam velocity distribution.

The Ba velocity measurement had always been thought as tractable with the means available in our laboratory. The presence of a high resolution laser and the existence of a very strong atomic Ba line within the tuning range of the laser dye used in the BaI spectroscopy made a velocity measurement based on the Doppler effect the one of choice. Yet, for reasons that will be presented below in detail this approach had to be replaced by one more challenging and experimentally more demanding. This method was based on the Doppler effect, but the Ba transition chosen was a two-photon process induced by our cw laser.

The Ba $^1P_1^o$ - $^1S_0$ Transition

The Ba $^1P_1^o$ - $^1S_0$ line (See Fig. 3.1a) has been the subject of numerous studies. The 553.6 nm Ba line - the so-called Ba resonance line - is used in flame analysis techniques and is the reason for the use of Ba compounds in green fireworks. A recent paper [2] has been devoted to the interpretation of the full line structure and its polarization dependence. This structure arises from the existence of several stable Ba isotopes and their different nuclear spin values. A list of these isotopes and their properties is given in Table 4.4. The even-mass isotopes can undergo only one transition, because their nuclear spin is 0. All odd-mass isotopes have spin of $^3/_2$. The total angular momentum quantum number, F, ($\mathbf{F} = \mathbf{J} + \mathbf{I}$) is $^3/_2$ in the ^1S state, but can have the values $^1/_2$, $^3/_2$, or $^5/_2$ in the ^1P state. The selection rule is $\Delta F = 0, \pm 1$ for a one-photon, dipole transition [3] and, thus, three transitions exist for each odd-mass isotope as shown in Fig. 3.1a.

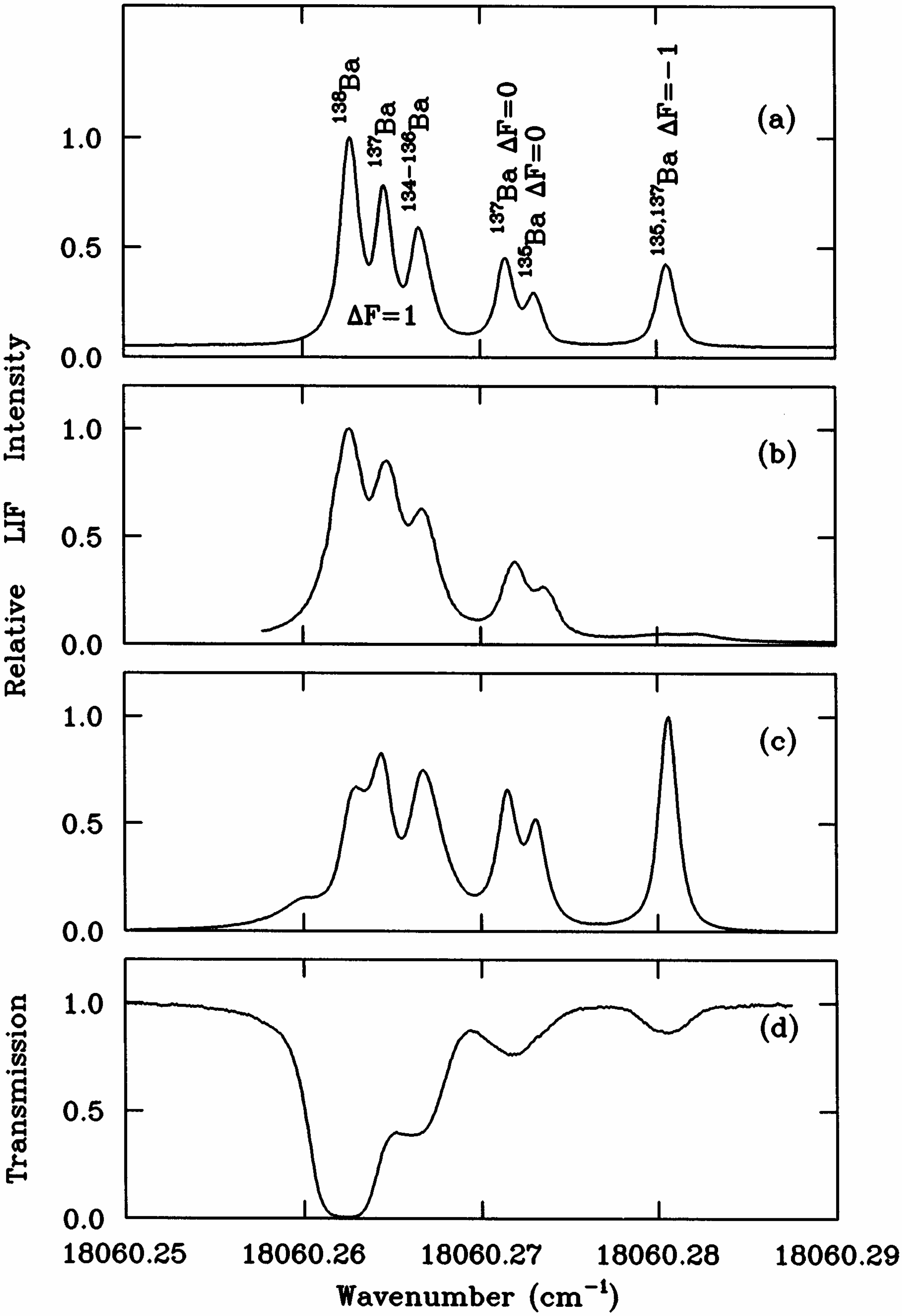

^{138}Ba
^{137}Ba
$^{134-136}$Ba
^{137}Ba ΔF=0
^{135}Ba ΔF=0
^{135,137}Ba ΔF=−1
ΔF=1
(a)
(b)
(c)
(d)
Relative LIF Intensity
Transmission
0.0
0.5
1.0
18060.25
18060.26
18060.27
18060.28
18060.29
Wavenumber (cm^{-1})

Figure 3.1. (Shown on the previous page) (a) Ba $^1P_1^o$ - $^1S_0$ LIF spectrum. Each peak has been identified by the corresponding Ba isotope and the change in total angular momentum quantum number, F. The detector axis was parallel to the electric field vector of the excitation laser beam. (b) The same spectrum as in (a) recorded under higher excitation laser power. Optical pumping decreases the relative intensity of the peaks with ΔF = -1. (c) The same spectrum as in (a) recorded at higher Ba number density corresponding to the operating oven temperature. Radiation trapping of the fluorescence from the strongest peaks in the spectrum distorts the shape of the spectrum severely. (d) Transmission spectrum of the same transition as in (a) recorded under conditions similar to those in (c). The optical density of the Ba beam is so high that all light is absorbed when the incident radiation is on resonance with the strongest transition. The increased linewidths are attributed to residual Doppler-broadening.

Overlooking subtle details in the experimental procedure can result in spectra that differ from the one shown in Fig. 3.1a. When the excitation laser power is not maintained at very low values, the ΔF = -1 transitions disappear from the spectrum (see Fig. 3.2b). The linearly-polarized laser light can only excite the m = $\pm^1/_2$ sublevels of the ground state to the F = $^1/_2$ states of the odd-mass isotopes, because of the Δm = 0 selection rule. Spontaneous emission can be linearly or circularly polarized (Δm = 0 or ±1). A Δm = ±1 fluorescence process can result in the atom being in an m = $\pm^1/_2$ state or an m = $\pm^3/_2$ state. Under high laser power, the m = $^1/_2$ population of odd-mass atoms can be depleted by the process called optical pumping. The effect observed in the LIF spectrum is that the peak corresponding to the ΔF = -1 transition reaches a limiting value as excitation power is increased and is consequently dwarfed by the other transitions that gain intensity.

Another difficulty also arises from the large transition dipole moment of the Ba $^1P^o$ - ^1S process [4] that manifests itself in different ways in absorption or LIF measurements. Under our experimental conditions the number density of Ba atoms is high enough to cause 100 % absorption of the incident light (see Fig. 3.1d). This effect distorts the absorption spectrum, because Beer's law does not hold at such high optical densities. The LIF spectrum is distorted more severely (see Fig. 3.c). Because of the finite size of the Ba beam, fluorescence is absorbed by Ba atoms before it is detected by the PMT thus causing a dip at the top of the absorption peaks. This effect is called self-absorption or radiation trapping [5]. We attempted to model this process on computer for the Doppler-free and Doppler-broadened spectra with partial success only. We were able to simulate the shape of the observed spectra, but the agreement was only qualitative.

The Ba $^3D_2$ - $^1S_0$ Transition

Two-photon transitions have considerably lower line strengths than their one-photon counterparts. They require high excitation power provided by either a pulsed laser or a focused cw laser beam. The low transition probability precludes two-photon emission, although two-photon stimulated emission has been observed for Ba [6]. Consequently, the resulting fluorescence is weak, but differs in wavelength from the excitation source. This difference can help minimize the effect of scattered laser light. The Ba $^3D_2$ - $^1S_0$ transition [7] located at 32200.4 cm^{-1} was chosen for the excitation step. Fluorescence was observed from the Ba $^3D_2$ - $^3P^o$ transition located at 440 nm.

A typical example of both a Doppler-free and a Doppler-broadened spectrum are shown in Fig. 3.2. The latter peaks at lower wavenumber than the former, because the laser beam is directed opposite to the Ba beam at a 45^o angle. The Doppler-broadened spectrum appears to have higher intensity because the beam splitter diverted more power

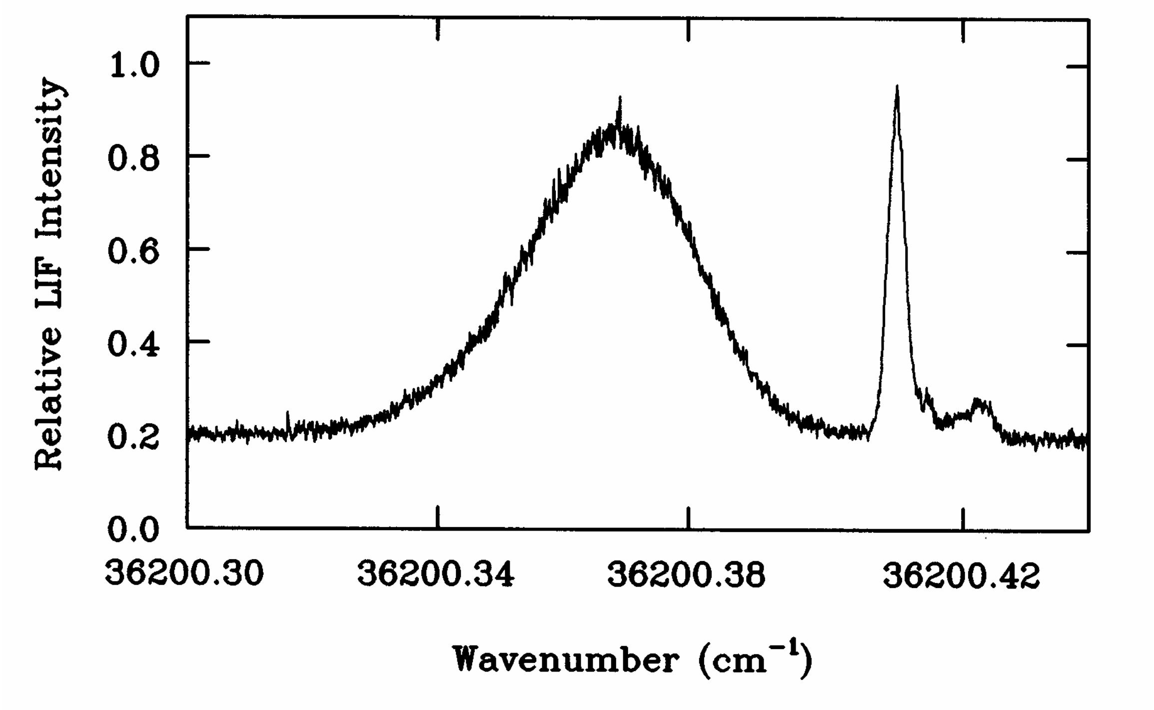

Figure 3.2. Ba $^3D_2$ - $^1S_0$ LIF Doppler-free (right) and Doppler-broadened spectra.

to the horizontal beam and because that beam is focused more sharply with a lens of shorter focal length than the lens located almost 1 m away from the sampled region. The spectra were recorded simultaneously by dividing the laser output in two beams with a beam splitter. The attenuating polarizers (see Chapter 2) had been removed from the beam path, but the power stabilization system was in operation. Neither the I_2 spectrum [8] nor the reference fringes from a monitor etalon (part of the integral wavemeter of the laser) recorded routinely during these scans could provide the degree of precision for the absolute calibration required to determine the Ba beam velocity distribution. Thus, the Doppler-free spectrum was used as an internal reference in the scan. It is the wavenumber shift, $\Delta\sigma$, that is related to the velocity, v_{Ba}, through the expression

$$\Delta\sigma = \sigma\, v_{Ba}\, c^{-1} \cos\theta \tag{3.2}$$

where σ is the transition wavenumber, θ is the angle between the beam axes (in all cases 135°), and c is the speed of light. The laser wavenumber calibration is not specified to be better than 0.0016 cm^{-1}. Such an error corresponds to an uncertainty of 18.7 m s^{-1}. Successive scans were often found to have even larger errors in the calibration. Recording both traces simultaneously circumvented the need for absolute calibration, because only the wavenumber shift was important in the determination of the beam velocity.

Ba Beam Velocity Distributions

The Doppler-broadened spectrum, $I(\sigma)$, is the result of the convolution of the Doppler-free spectrum, $I_0(\sigma)$, with the Ba beam velocity distribution, $f(v_{Ba})$, viz.,

$$I(\sigma) = A\int_{-\infty}^{+\infty} I_0(\sigma')\ f(v_{Ba})\ d\sigma' \qquad (3.3)$$

where A is a scaling factor. The integration is performed under the constraint :

$$v_{Ba} = \frac{c}{\cos\theta}\ \frac{\sigma - \sigma'}{\sigma'} \qquad (3.4)$$

Two approaches were attempted for the deconvolution of $f(v_{Ba})$. One involved Fourier transforms and the other a fit with an incorporated convolution. In the first approach, both spectra were Fourier transformed, their transforms were divided point by point, and the inverse transform of the division result gave the velocity distribution. Another step became essential, namely the multiplication of the division result by a low-pass filter function to eliminate all high-frequency noise [9]. The resulting $f(v_{Ba})$ thus determined was defined by discrete points and a fit by some function of v_{Ba} was necessary to provide a more compact description the velocity distribution. The results of this procedure were not very satisfactory and a different, less elegant approach was followed.

In the second approach, a non-linear least squares fit [10] was performed to determine the parameters of $f(v_{Ba})$ by calculating $I(\sigma)$ according to Eq. 3.3. In both approaches it was found that the following form for the velocity distribution could give a good fit.

$$f(v_{Ba}) = N\,(v_{Ba} - v_0)^2 \exp\left[-\frac{(v_{Ba} - v_s)^2}{\alpha_s^2}\right] \tag{3.5}$$

where v_{Ba}, v_s, and α_s were fitting parameters, $v_{Ba} > v_0$, and N was the normalization constant. The chosen form differs from the expressions for a thermal beam (Eq. 3.6) or a supersonic beam [11,12] (Eq. 3.7), because neither gave a satisfactory fit, although the latter was better than that for a thermal beam.

$$f(v_{Ba}) = N\,v_{Ba}^2 \exp\left[-\frac{v_{Ba}^2}{\alpha_s^2}\right] \tag{3.6}$$

$$f(v_{Ba}) = N\,v_{Ba}^2 \exp\left[-\frac{(v_{Ba} - v_s)^2}{\alpha_s^2}\right] \tag{3.7}$$

Figure 3.3 shows the fits using the three models for the velocity distribution and Figure 3.4a contrasts the corresponding distributions. Models used for oven beams [13] predict a deviation from a pure "thermal" distribution, but the adjustable parameters they contain can not predict the complete elimination of the very low velocities.

It should be noted that the velocity distribution determined for the Ba beam was not affected by the presence of other gases, e.g., HI, because the measurements were usually taken in the absence of other gases. In the case of the crossed-beam experiments no noticeable effect on the Ba beam was expected because of the very low collision rate. In the case of the beam-gas experiments the intensity of the Ba beam was found to be reduced, but no significant change in the shape of the distribution could be determined.

The only way we could affect the Ba velocity distribution was by varying the oven temperature. The temperature range used was not very wide, because a reduction in temperature resulted in a decrease in beam density. Increase of the temperature above the usual values was not practical, because the glow from the oven increased the fluorescence background levels. Over the range of temperatures used it was observed that the velocity

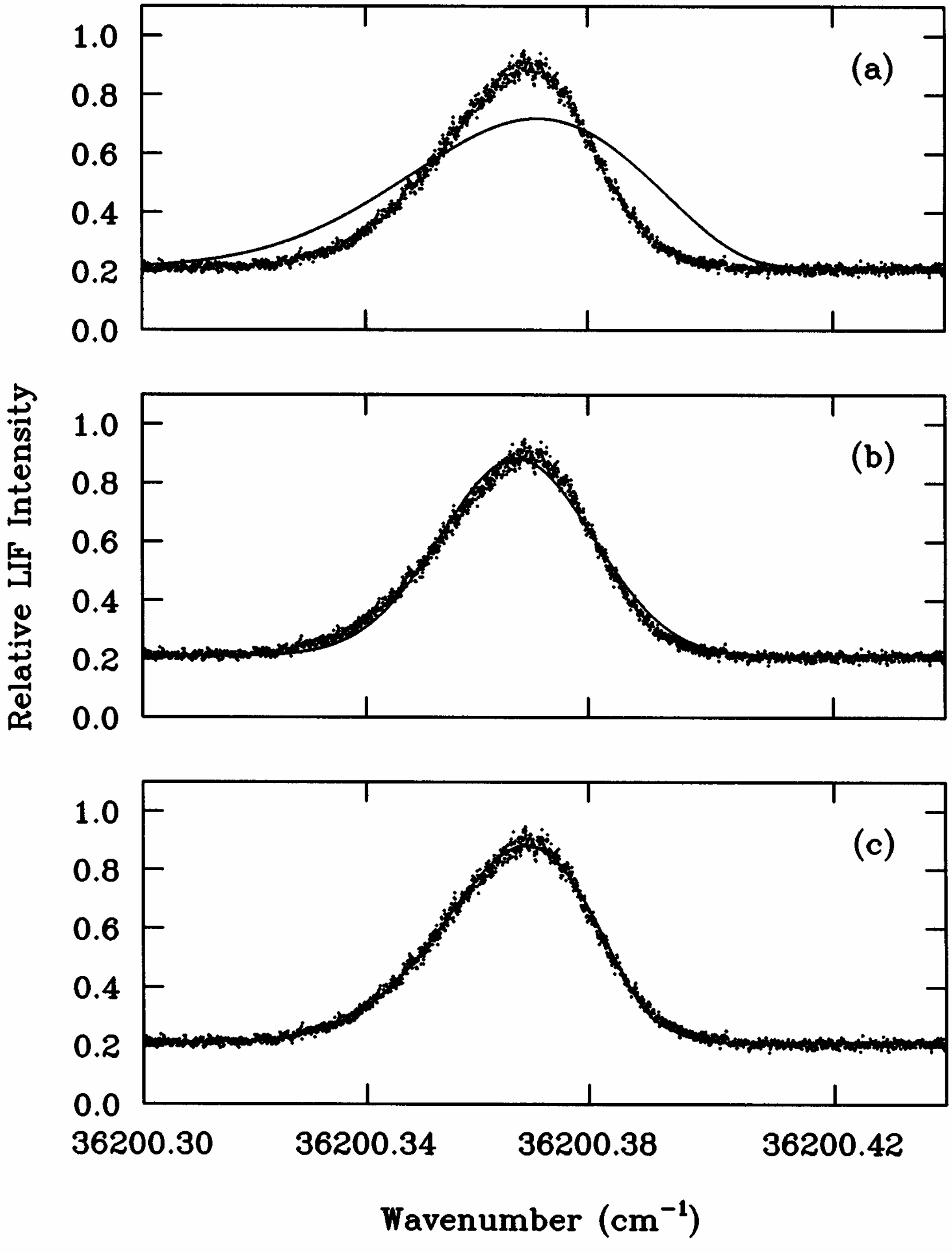

Figure 3.3. Best fit simulations of the Ba $^3D_2$ - $^1S_0$ Doppler-broadened spectrum based on (a) a thermal Boltzmann velocity distribution with a_s = 497 (2) m s^{-1} (cf. Eq. 3.6), (b) a supersonic beam velosity distribution with v_s = 441.2(1) m s^{-1} and a_s = 230.0 (1) m s^{-1} (cf. Eq. 3.7), and (c) a modified supersonic beam velosity distribution with v_0 = 226.6 (14) m s^{-1}, v_s = 169 (8) m s^{-1}, and a_s = 322 (2) m s^{-1} (cf. Eq. 3.5)

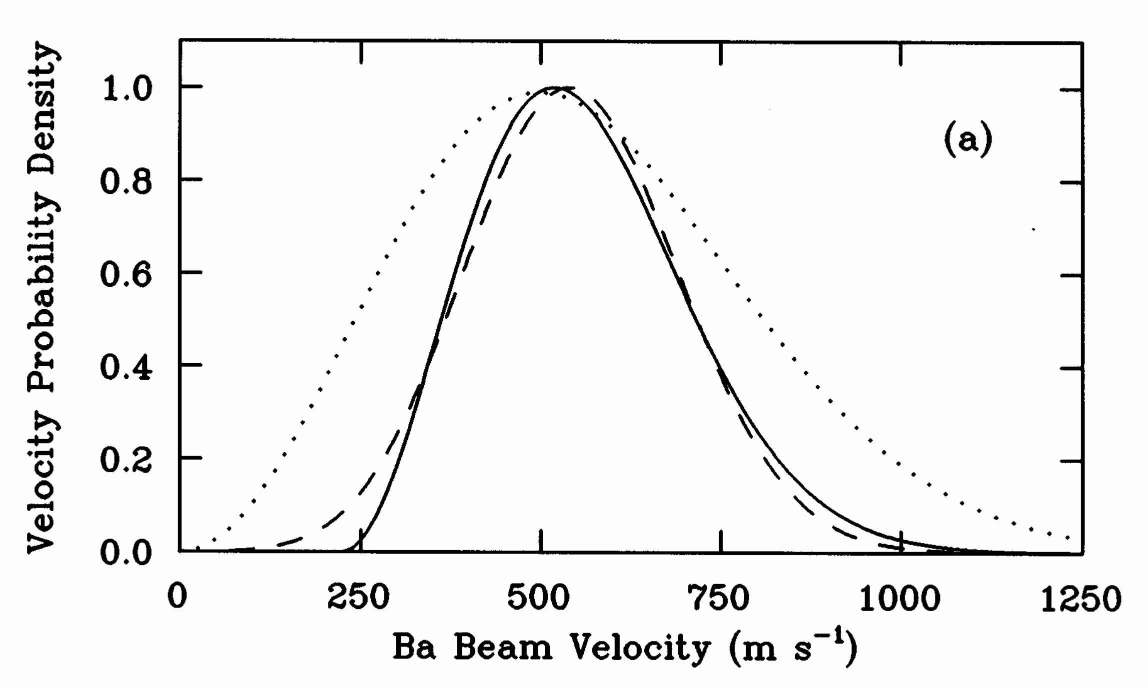

Figure 3.4. Ba beam velocity distributions based on the fits shown in Fig. 3.3, viz., a thermal distribution (dotted curve), a supersonic distribution (dashed curve), and a modified supersonic distribution (solid line).

distribution became narrower and its peak shifted to higher velocities (it became more "supersonic-like") as the temperature increased.

In all cases we assumed that the transverse velocity components were negligible. The assumption is well justified considering the geometrical constraints imposed on the beam. Given that the beam is collimated to a half-angle of 2.82^o (see Chapter 2), the ratio of the transverse component to the longitudinal velocity is less than 0.05.

The HI Beam

The HI beam velocity distribution could not be determined by means of the Doppler effect, because HI molecules do not absorb visible light. A more direct timing method - a standard time-of-flight (TOF) method [12] - was preferred for this beam. Since individual molecules cannot be tagged and monitored as they travel over a known distance, a rotary chopper was used to generate short pulses of gas that propagated through the vacuum chamber like the uninterrupted beam. After traversing an accurately measured flight path on the order of 80 cm, HI pulses, now temporally broadened because of the spread in velocities, reached the ionizer of the mass spectrometer and were detected by the ion detector. The final signal recorded by the computer was the convolution of the chopper shutter function, the beam velocity distribution, and the response function of the detector and amplifier. The shutter function was known from the geometrical and mechanical characteristics of the chopper. The response function was not known a priori, but was assumed to have a simple exponential form.

After preliminary numerical processing of the time markers to determine the absolute time calibration of the TOF scan, the mass spectrometer signal was fit [10] by the double convolution integral that simulated the experimental signal. The velocity distribution was assumed to have the standard form for a supersonic beam, viz.,

$$f\left(v_{HI}\right) = N\ v_{HI}^{2} \exp\left[-\frac{\left(v_{HI} - v_{s}\right)^{2}}{\alpha_{s}^{2}}\right] \tag{3.8}$$

This form provided a satisfactory fit. An example is shown in Fig. 3.4b.

The same experimental and fitting procedure had to be followed prior to the HI measurements for the calibration of the ion mass-dependent ion flight time inside the quadrupole filter. For these measurements a dilute mixture of SF_6 in N_2 carrier gas was used. SF_6 fragments upon ionization to a wide range of ion masses that are known to have resulted from the one species with a single velocity distribution. In principle, the same calibration could be accomplished with HI which could yield HI^+, I^+, or H^+ ions. In practice this calibration was not feasible with our mass spectrometer. H^+ could not be

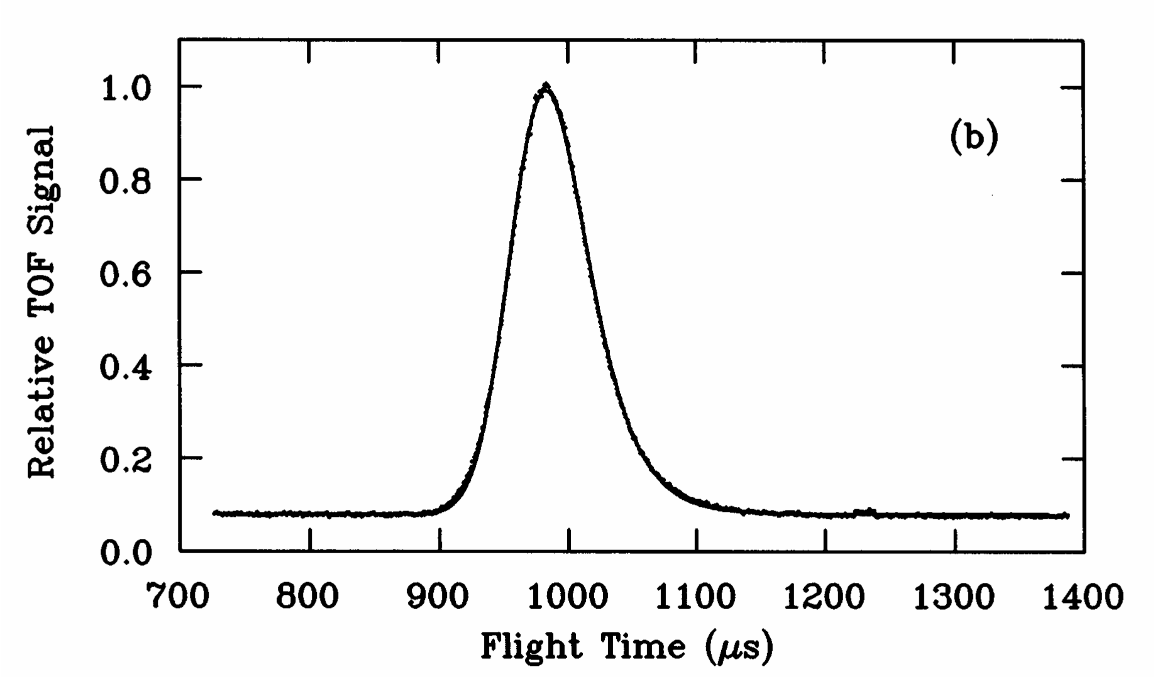

Figure 3.5. Time-of-flight scan for the HI/N_2/He supersonic beam and corresponding fit (smooth solid curve). The flight path was 79.3 cm and the ion monitored was HI^+. The fitting parameters were v_s = 785.2 (1) m s^{-1} and a_s = 31.1 (1) m s^{-1}.

detected under normal operating conditions and the remaining two ions have very similar masses to allow the determination of the mass dependence of the ion flight time.

It is interesting to note that in the few cases the velocity distribution of the carrier gas was also determined, no significant velocity slip between the heavy seed and the lighter carrier gas could be established.

The wide range of average carrier gas masses from a combination of N_2 in any proportion with Ar or He provided a variation of the beam velocities that ranged from 650 m s^{-1} to 1200 m s^{-1}. H_2 was never used as carrier gas because for the most part of our crossed-beam studies we could not use spectroscopic data from very fast collision conditions.

Relative Velocity Distributions

Relative velocity, $\mathbf{v}_{rel}$, of the colliding particles is the velocity of one collision partner in the frame of reference of the other particle [11]. If $\mathbf{v}_{Ba}$ and $\mathbf{v}_{HI}$ are the velocities of the two particles, then

$$\mathbf{v}_{rel} = \mathbf{v}_{Ba} - \mathbf{v}_{HI} \tag{3.9}$$

In a well-defined experiment the relative orientation of the reagent velocities is known and $\mathbf{v}_{rel}$ can be calculated.

In the crossed-beam experiments we assumed that both beams were one-dimensional and that the angle between them was exactly 90°. Then

$$v_{rel} =: |\mathbf{v}_{rel}| = \sqrt{v_{Ba}^2 + v_{HI}^2} \tag{3.10}$$

The relative velocity distribution is given by the following convolution integral:

$$f(v_{rel}) = \int_0^{+\infty} \int_0^{+\infty} f(v_{Ba})\; f(v_{HI})\; \delta\left(v_{rel} - \sqrt{v_{Ba}^2 + v_{HI}^2}\right) dv_{Ba}\; dv_{HI} \tag{3.11}$$

which can be simplified to:

$$f(v_{rel}) = \int_0^{v_{rel}} f(v_{Ba})\; f\left(v_{HI} = \sqrt{v_{rel}^2 - v_{Ba}^2}\right) \frac{\partial v_{HI}}{\partial v_{rel}}\; dv_{Ba} \tag{3.12}$$

This integral cannot be calculated analytically. A typical example of all three velocity distributions is shown in Fig. 3.6a.

In the beam-gas experiments we have to take into account the three-dimensional motion of the HI molecules. Analytical expressions for the relative velocity distribution in an experiment involving a supersonic beam and a Boltzmann gas were derived by two research groups [14,15] at the same time. These expressions correspond to a Ba velocity distribution that follows Eq. 3.6. We believe that the error introduced by the use of an

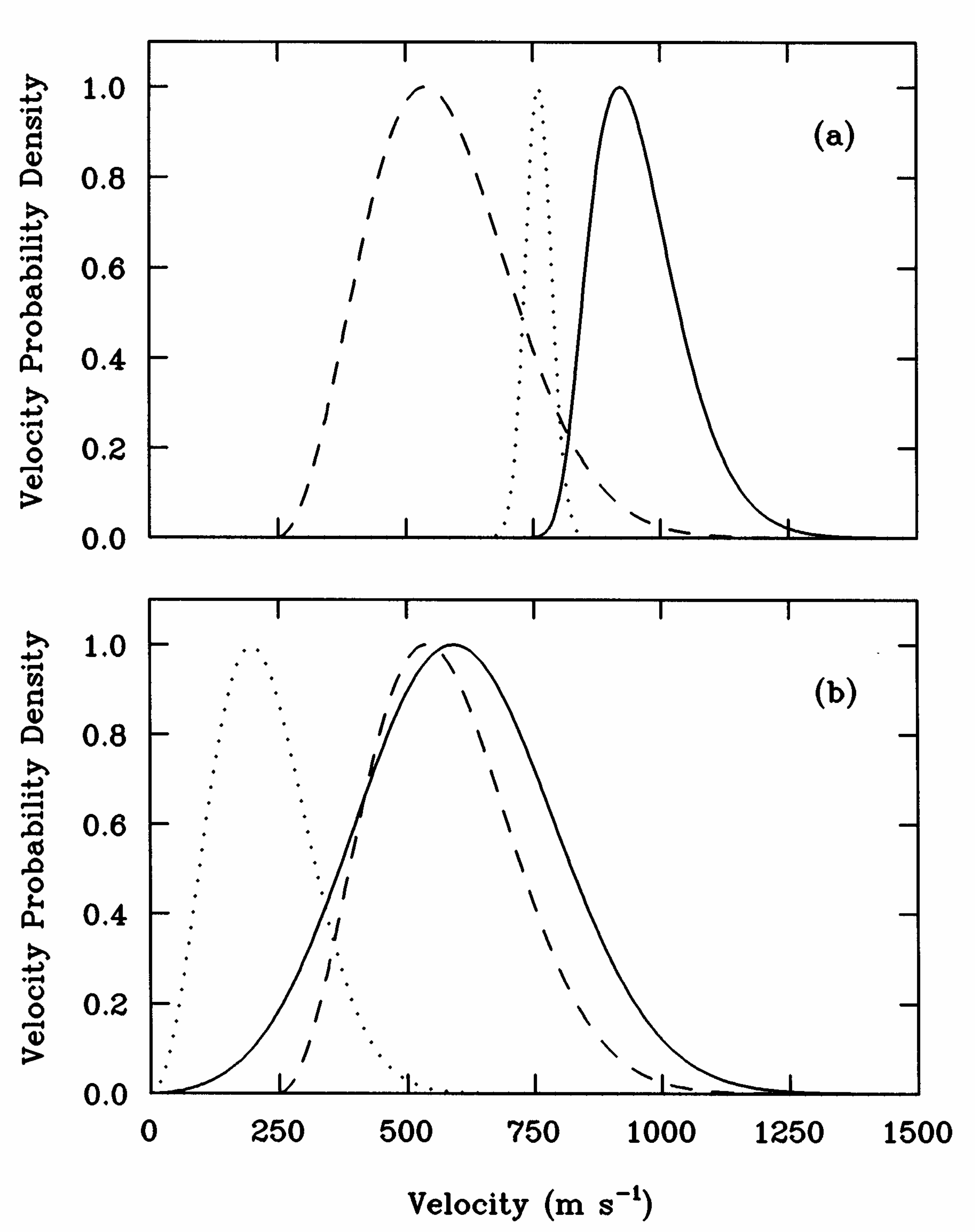

Figure 3.6. Reagent velocity distributions and relative velocity distributions for (a) a crossed-beam experiment and (b) a beam-gas experiment. The velocity distributions of Ba are represented by the dashed curves, those of HI by the dotted curves, and the corresponding relative velocity distributions by the solid curves.

imperfect beam velocity distribution is not significant when compared to the width of the relative velocity distribution and errors in other quantities of importance in the beam-gas experiments.

The velocity distributions of the reagents and their relative velocity distribution in a beam-gas experiment are presented in Fig. 3.6b. It should be noted that because of the narrow range of the HI velocities, the relative velocity follows closely the Ba beam velocity distribution. Under these conditions the possible variations in the relative velocity are very limited. Despite this limitation, experimental conditions were not sufficiently reproducible from run to run requiring Ba velocity measurements during each experiment.

Table 3.1 shows the experimentally determined parameters for the reagent velocity distributions and resulting relative velocity distributions and collision energy distributions for a series of crossed-beam experiments. Reagent velocity parameters for a representative beam-gas experiment were as follows. For the barium beam, $v_s = 451$ m s^{-1} and $\alpha_s = 237$ m s^{-1} which corresponded to $v_{mean} = 561$ m s^{-1} and FWHM = 198 m s^{-1}; for the HI gas, $\alpha_s = 198$ m s^{-1} which corresponded to $v_{mean} = 223$ m s^{-1} and FWHM = 222 m s^{-1}; for the relative velocity, $v_{mean} = 599$ m s^{-1} and FWHM = 468 m s^{-1}; and for the collision energy, $E_{mean} = 13.1$ kJ mol^{-1} and FWHM = 16.7 kJ mol^{-1};

References

1 W. Demtröder, "Laser Spectroscopy," Springer-Verlag, Berlin, 1988.

2 P. E. G. Baird, R. J. Brambley, K. Burnett, D. N. Stacey, D. M. Warrington, and G. K. Woodgate, *Proc. R. Soc. Lond. A* **365**, 567 (1979).

3 I. I. Sobelman, "Atomic Spectra and Radiative Transitions," Springer-Verlag, Berlin, 1979.

4 S. Niggli and M. C. E. Huber, *Phys. Rev. A* **39**, 3924 (1989).

5 C. J. Cannon, "The Transfer of Spectral Line Radiation," Cambridge University Press, Cambridge, 1985.

6 D. J. Gauthier, Q. Wu, S. E. Morin, and T. W. Mossberg, *Phys. Rev. Lett.* **68**, 464 (1992).

7 W. Jitschin and G. Meisel, *Z. Physik A* **295**, 37 (1980).

8 S. Gerstenkorn and P. Luc, "Atlas du Spectre d'Absorption de la Molécule d'Iode," Centre Nationale de la Recherche Scientifique, Paris, France, 1978; S. Gerstenkorn and P. Luc, *Rev. Phys. Appl.* **14**, 791 (1979).

9 J. D. Morrison, *J. Chem. Phys.* **39**, 200 (1963); G. K. Wertheim, *J. Electron Spectrosc.* **6**, 239 (1975).

10 D. W. Marquardt, *J. Soc. Ind. Appl. Math.* **11**, 431 (1962).

11 R. D. Levine and R. B. Bernstein, "Molecular Reactions Dynamics and Chemical Reactivity," Oxford University Press, New York, 1987.

12 D. J. Auerbach, Velocity Measurements by Time-of-Flight Methods, in "Atomic and Molecular Beam Methods," G. Scoles, ed., Oxford University Press, New York, 1988.

13 H. Pauly, Other Low-Energy Beam Sources, in "Atomic and Molecular Beam Methods," G. Scoles, ed., Oxford University Press, New York, 1988; W. J. Siekhaus, R. H. Jones, and D. R. Olander, *J. Appl. Phys.* **41**, 4392 (1970).

14 R. C. Estler and R. N. Zare, *Chem. Phys.* **28**, 253 (1978).

15 A. E. Redpath, M. Menzinger, and T. Carrington, *Chem. Phys.* **27**, 409 (1978).

Table 3.1. Beam velocity parameters for crossed-beam experiments and resulting relative velocity and collision energy distributions. Units used are m s^{-1} and kJ mol^{-1}. Experiments are listed in order of increasing values of mean relative velocity.

Label	Ba Beam Velocity					HI Beam Velocity				Relative Velocity		Collision Energy	
	v_0	v_s	α_s	v_{mean}	FWHM	v_s	α_s	v_{mean}	FWHM	v_{mean}	FWHM	E_{mean}	FWHM
a[1]	227.1	267.6	295.2	579.1	341.5	645.8	31.9	647.4	53.1	875.3	234.3	25.7	14.2
b	253.2	177.4	323.5	585.6	343.0	693.5	30.9	694.9	51.4	915.4	229.5	28.1	14.6
c	183.3	241.8	306.0	556.4	358.3	720.7	30.1	721.9	50.0	919.3	226.6	28.3	14.4
d	259.0	310.6	282.3	602.0	329.9	736.5	35.8	738.2	59.5	958.7	217.1	30.7	14.3
e	247.6	234.6	296.9	576.8	329.5	758.9	36.5	760.7	60.7	961.0	209.6	30.8	13.8
f	250.6	391.7	251.8	607.2	317.9	741.2	32.9	742.6	54.7	965.0	207.9	31.1	13.7
g	276.3	451.0	224.2	623.2	294.5	769.8	30.8	771.0	51.2	996.2	191.0	33.1	12.9
h	182.9	281.5	295.6	564.7	356.7	785.2	31.1	786.4	51.8	975.8	216.6	31.8	14.5
i	233.5	267.5	291.7	578.5	335.9	849.2	34.9	850.7	58.1	1035.3	200.3	35.7	14.1
	222.6	169.2	321.6	562.2	346.8	574.8	26.9	576.1	44.7	811.7	248.0	22.2	14.1

[1] Experiment labels used in Figs. 5.4, 5.5, 5.6, 6.3, 6.4, and 6.5.

Chapter 4. The BaI $C^2\Pi$ - $X^2\Sigma^+$ Band System

Introduction

The objective of our experiments has been the determination of specific opacity functions, which requires that product rotational population distributions be measured. Given that BaI is formed in its ground electronic state, a spectroscopic probe is needed to measure the rovibrational distributions.

Spectral lines attributed to BaI were first recognized in 1906 [1] in what is now called the $C^2\Pi$ - $X^2\Sigma^+$ band system. Since then, the following states (with corresponding term energies in cm^{-1} given in parentheses) have been identified [2-8]: $A'^2\Delta_{3/2}$, $A^2\Pi$ (9595), $B^2\Sigma^+$ (10417), $C^2\Pi$ (18188), $D^2\Sigma^+$ (25774), $E^2\Sigma^+$ (26754), and $^2\Pi$ (49698) . The ground state, $X^2\Sigma^+$, remains the one best studied, mostly by microwave and electronic spectroscopy. The C - X band has always been the one known to the highest degree of detail relative to other bands. It is located in the green region of the visible spectrum where very high resolution lasers existed for over ten years. These facts were the reasons for choosing to use the BaI C - X band system to study the products of the Ba + HI reaction.

At the early stages of the studies undertaken in our laboratory very little was known about the rotational structure of the BaI spectrum. The first investigations [9] were able to assign rovibronic transitions using population-labeling optical-optical double resonance in a molecular beam of BaI. In the (0,0) and (8,8) bands the transitions studied were assigned J values less than 60. Subsequent studies were able to record and assign line positions for some of the branches in the (0,0) [10] and (8,8) [11] bands using SDLIF (see next section for definition). The set of available data was expanded when the reaction forming BaI was first studied under crossed-beam conditions [12]. The highly excited, narrow rotational distributions observed were assigned by extrapolating the known branches. Finally, beam - gas studies using SDLIF added a large number of line positions in a wide range of vibrational bands [13].

Previous spectroscopic studies had yielded sets of spectroscopic constants that were necessary to simulate the observed transitions in the (0,0) and (8,8) bands only [10-12]. In the latest stage [13], we were able to reproduce all transitions in all bands with one set of constants. This achievement greatly facilitated our attempts to record BaI(v) rotational distributions with v between 0 and 24.

The BaI $C^2\Pi$ - $X^2\Sigma^+$ Band System and SDLIF

Energy levels in the ground electronic state of BaI ($X^2\Sigma$) are characterized mainly by the vibrational and the rotational quantum numbers. Coupling between the electronic spin and the molecule's rotation causes each rotational level to split in two closely spaced sublevels [14]. Levels in the $C^2\Pi$ state are separated in two spin-orbit subterms ($^2\Pi_{1/2}$, $^2\Pi_{3/2}$) that differ in energy by 756 cm^{-1}. Λ-doubling splits the energy levels further in two sublevels. For a given set of values of the vibrational and rotational quantum numbers, there are two energy levels in the $X^2\Sigma$ state and four in the $C^2\Pi$ state. Most electronic transitions of BaI are attributed to transfer of an electron between orbitals with predominantly Ba-atom character [15]. The parity-allowed electric-dipole transitions between the C and X states give rise to 12 branches (see Fig. 1). In order of increasing wavenumber they are called P_{12}, P_1, Q_{12}, Q_1, R_{12}, R_1, P_2, P_{21}, Q_2, Q_{21}, R_2, and R_{21}.

The P_{12}, P_1, Q_{12}, P_2, P_{21}, and Q_2 branches of the diagonal transitions ($\Delta v=0$) form bandheads shading to the blue. The Q_1, R_{12}, Q_{21}, and R_2 branches rise very steeply in the Fortrat diagram. [A Fortrat diagram is a map indicating transition wavenumbers as a function of the quantum numbers of the upper and lower rovibronic states (see Fig. 4.2a).]

BaI has an exceptionally large moment of inertia among diatomic molecules. Consequently, its rotational constant B is very small (approximately 0.027 cm^{-1}).

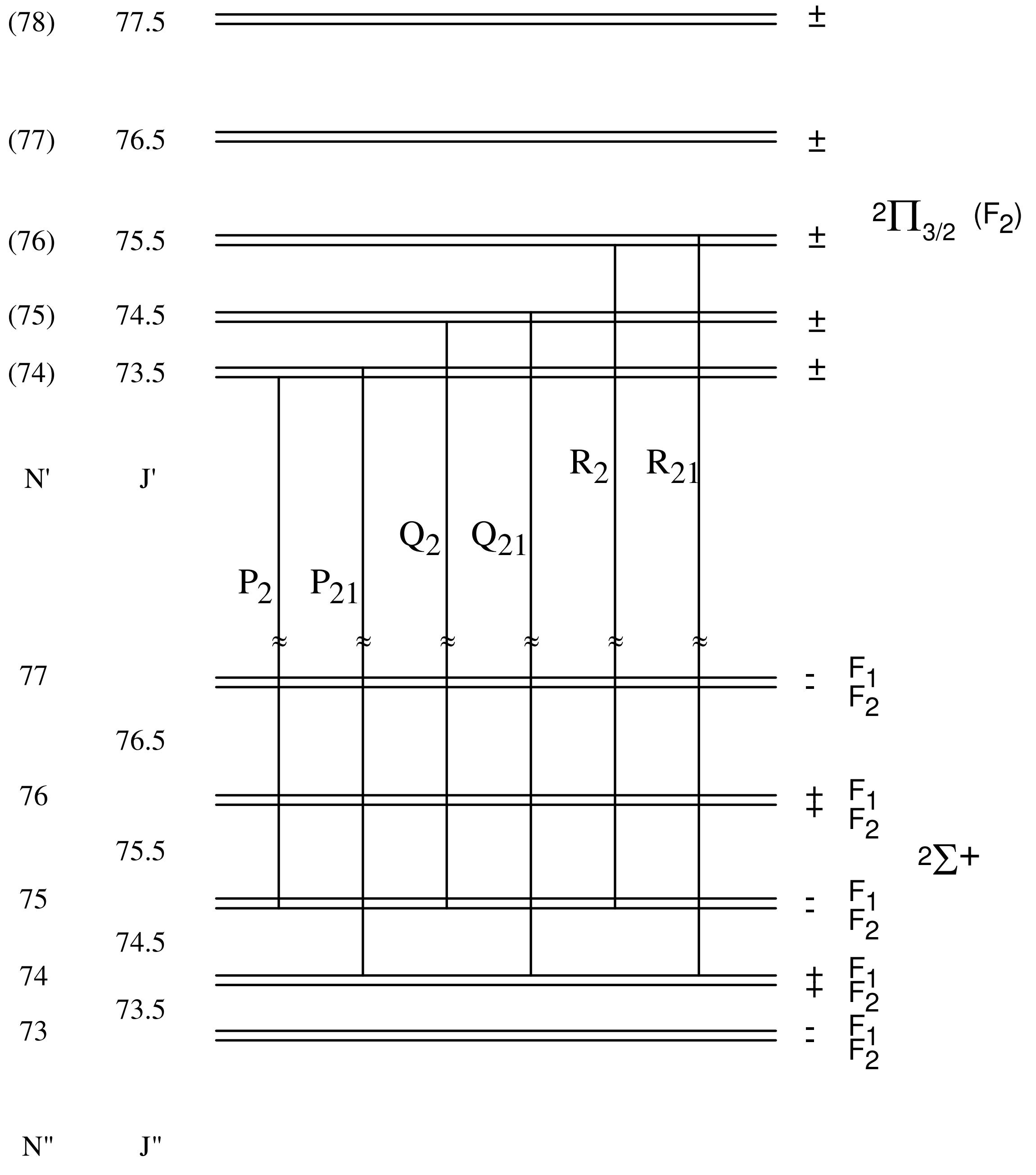

Figure 4.1. Energy levels and transitions in the BaI $C^2\Pi_{3/2}$ and $X^2\Sigma^+$ states. The simplified rotational energy manifold for the C state ignores the other spin-orbit state, $C^2\Pi_{1/2}$. No vibrational levels are shown for either state.

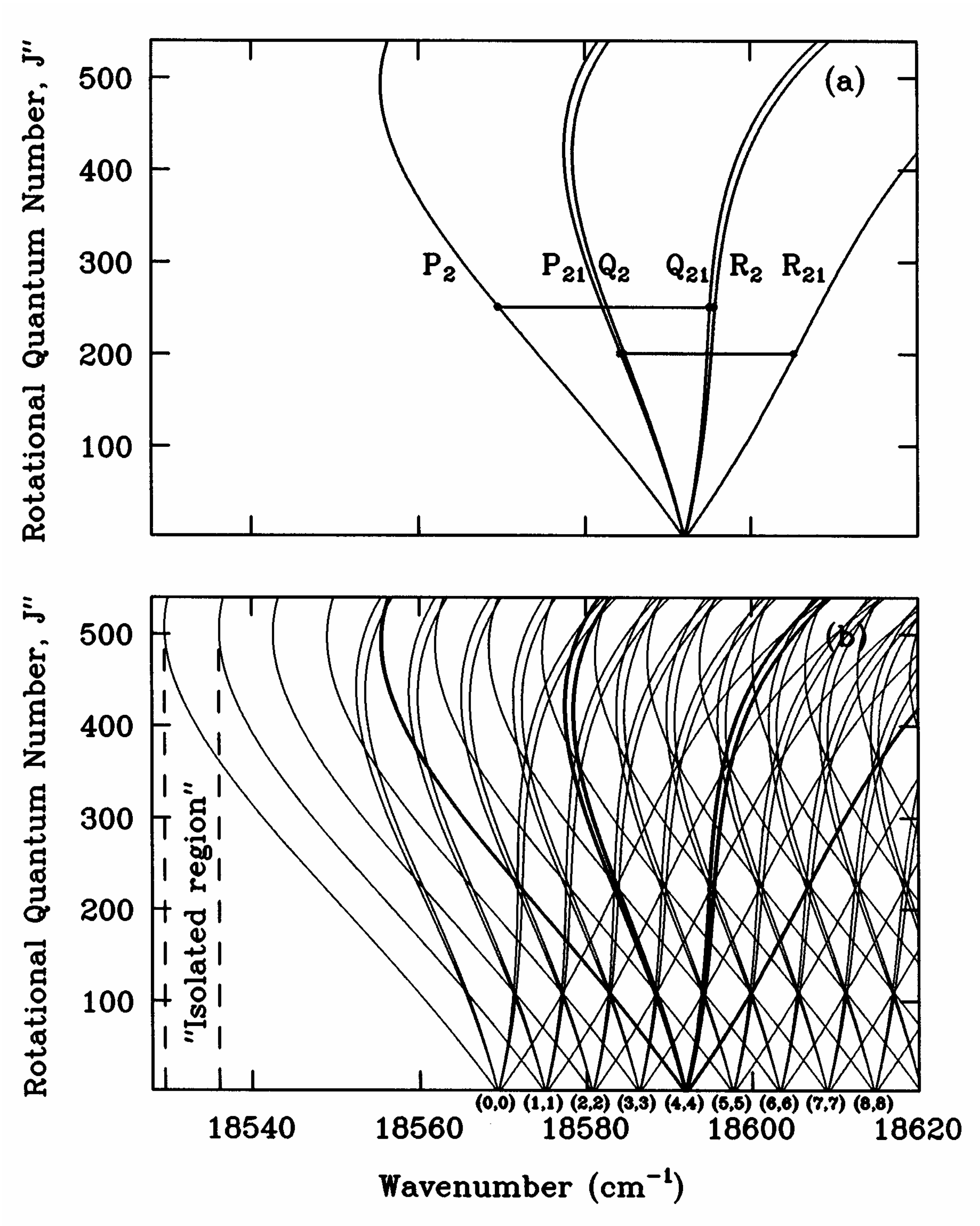

Figure 4.2. (a) Fortrat diagram for the BaI $C^2\Pi_{3/2}$ - $X^2\Sigma^+$ (4,4) subband. Branches connected with a horizontal line share the same upper state levels.
(b) Fortrat diagram for the BaI $C^2\Pi_{3/2}$ - $X^2\Sigma^+$ (Δv=0) sequence. The Fortrat diagram for the other subband is almost identical, but is displaced to lower wavenumbers by 756 cm^{-1}.

Moreover, the C and X states have almost identical potential energy curves. This similarity causes (v,v) transitions to be very strong and vibrational and rotational constants to have almost the same values in both states. Accordingly, all bands are closely spaced and branches are very dense and overlap extensively (see Fig. 4.2b). Finally, each line has hyperfine structure [16] caused by coupling of the molecular angular momentum to the nuclear spin of I ($I_I = {}^5/_2$). As a result, one branch can have as many as 30 lines per 1 cm^{-1} and each line can have a width of 0.02 cm^{-1}. At any given wavenumber, many transitions belonging to different bands or branches can occur. The resulting LIF spectrum is very hard to assign. Only features like bandheads or inflection points in branches stand out because of their compounded intensities.

Selectively detected laser-induced fluorescence (SDLIF) [17] is a technique applied to reduce the complexity of the LIF spectra by preferentially observing fluorescence from a band of interest. The underlying principle is that a molecule can fluoresce via any of three branches, viz., the P, Q, or R branches (see Fig. 1). The following sets of branches share excited levels of the same parity and both excitation and emission can occur in any of the three branches in each set: (P_{12}, Q_1, R_{12}), (P_1, Q_{12}, R_1), (P_2, Q_{21}, R_2), (P_{21}, Q_2, R_{21}). If a narrow bandpass filter (in our experiments it was a 1-m monochromator) is tuned to the wavenumber at which a molecule can emit after it has been excited at a different wavenumber (via a different branch), then only a few molecular states can fulfill the condition for detection.

As seen from a Fortrat diagram, there are places where branches from different bands cross. If these branches, that provide the excitation step, cross and their conjugate branches, that provide the fluorescence step, also cross, then transitions from both bands are observed and interpretation of that section of the spectrum becomes more difficult.

The exact effect of these interferences in the spectra depends on the relative slope of the corresponding branches in the Fortrat diagram. It can be easily confirmed that a branch that has many transitions over a short range of wavenumbers (i.e., has a large slope) causes a sharp rise in the baseline of the co-observed branch. Individual line positions of the interfering branch will not be resolved, because they overlap, but the ones of the other branch will be easy to locate. This is the reason why we took most of our SDLIF data for BaI rotational distributions by scanning along the R_{21} branch and collecting fluorescence from the P_{21} and Q_2 branches. The upper spin-orbit subband was preferred over the lower one because lines profiles in the P and R branches of the $C^2\Pi_{3/2}$ - $X^2\Sigma^+$ subband are half as wide as the ones of the $C^2\Pi_{1/2}$ - $X^2\Sigma^+$ subband. This effect arises from differences in hyperfine splitting in the two spin-orbit states [16].

Experimental

The chamber and laser system described in Chapter 2 were used throughout the measurements presented here. In all cases, BaI was formed in the reaction Ba + HI ∅ BaI + H. A Ba beam reacted with (a) a crossed supersonic HI beam or (b) with HI background gas. BaI molecules were excited in the $C^2\Pi$ - $X^2\Sigma^+$ band system by a ring dye laser with only a fraction of its output power directed to the molecules to avoid saturation of the transitions. BaI fluorescence was admitted to a photomultiplier tube (PMT) through (a) a bandpass interference filter or (b) through a monochromator acting as a very narrow bandpass filter. The PMT signal was monitored (a) with phase sensitive detection or (b) with photon counting. The output signal from either device was recorded on a computer as a function of the excitation laser wavenumber. Two input channels of the computer were used to record the stabilized laser power and the absorption spectrum of I_2 at room temperature.

Results

Crossed beam experiments yielded LIF spectra of isolated branches in the following bands: the branches P_{12} (see Fig. 4.3a), P_1, Q_{12}, P_2, P_{21}, and Q_2 in the (0,0) band and the P_{12} and P_2 branches (see Fig. 4.4) in the (1,1), (2,2), and (3,3) bands. Also

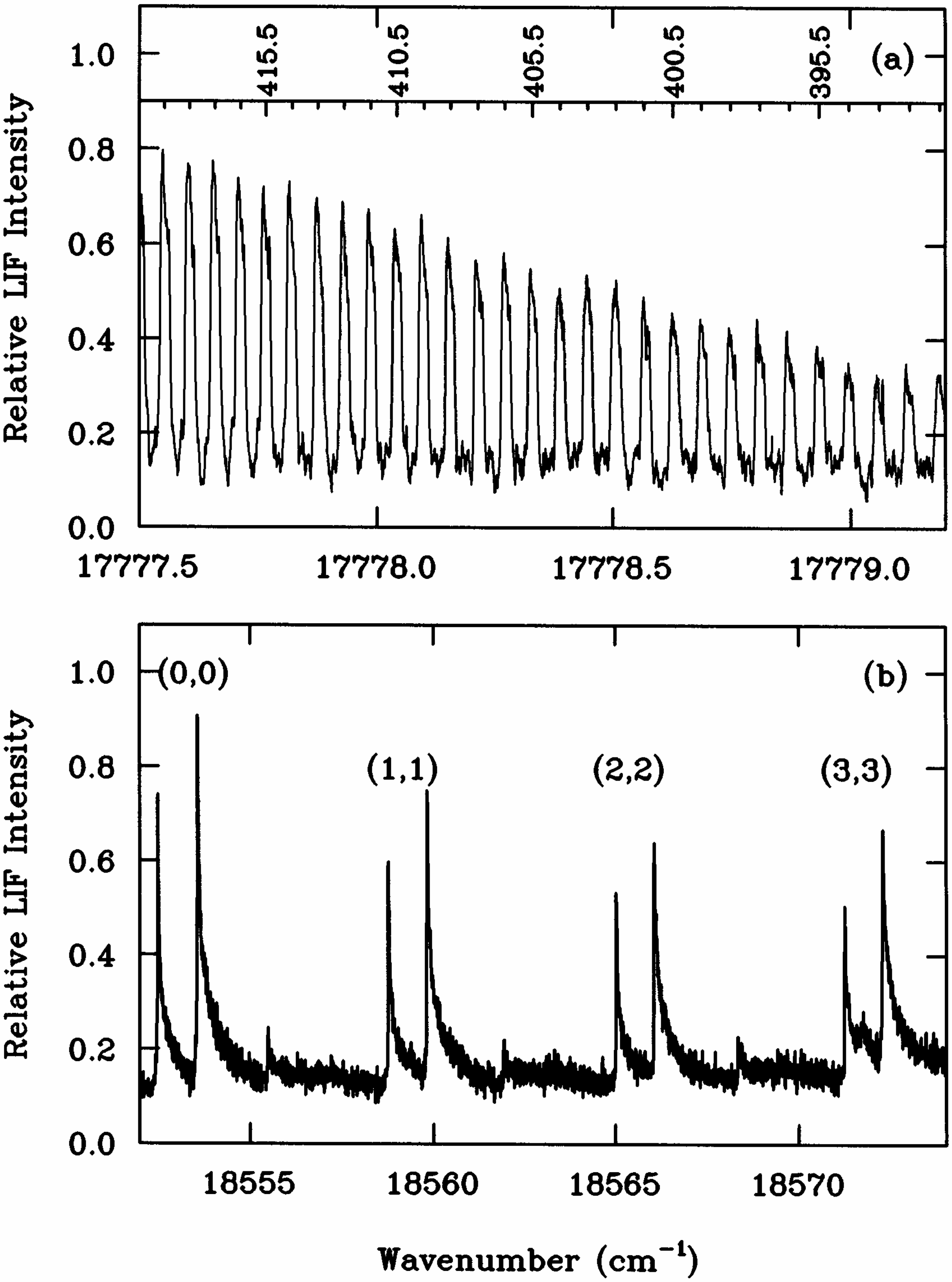

Figure 4.3. (a) BaI $C^2\Pi_{1/2}$ - $X^2\Sigma^+$ (0,0) P_{12} branch members. No other band or branch of the $\Delta v=0$ sequence overlaps in the same range of wavenumbers. (b) BaI $C^2\Pi_{3/2}$ - $X^2\Sigma^+$ (v,v) P_{21} and Q_2 bandheads for v=0, 1, 2, 3, and 4.

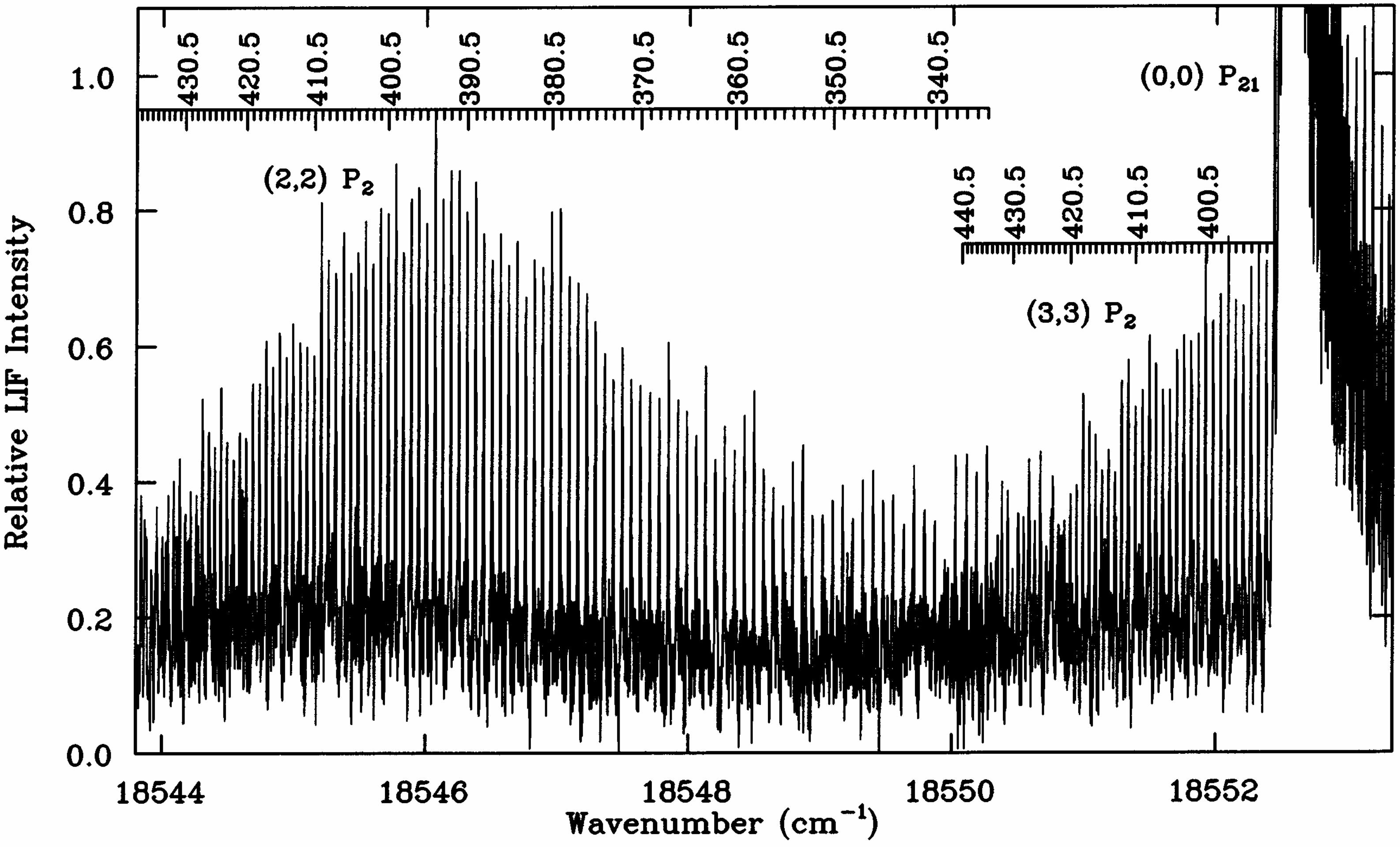

Figure 4.4. Undispersed fluorescence spectrum of the BaI $C^2\Pi_{3/2}$ - $X^2\Sigma^+$ (v,v) subband showing P_2 branch members of the (2,2) and (3,3) bands and the strong (0,0) P_{21} bandhead.

Table 4.1. Wavenumbers of experimental bandhead positions and differences from calculated positions.

Branch	(v,v)	Expt (cm^{-1})	Expt–Calc. (cm^{-1})	Branch	(v,v)	Expt (cm^{-1})	Expt–Calc. (cm^{-1})
P_{12}	0	17775.076	0.005	P_{21}	0	18552.498	0.008
	1	17781.361	0.000		1	18558.765	0.007
	2	17787.637	0.005		2	18565.014	0.007
	3	17793.881	-0.003		3	18571.249	0.011
	4	17800.125	0.007		4	18577.462	0.012
P_1	0	17795.127	0.010		5	18583.655	0.011
	1	17801.232	0.006		6	18589.832	0.012
	2	17807.322	0.008		7	18595.988	0.010
	3	17813.388	0.005		8	18602.126	0.009
	4	17819.441	0.007		9	18608.245	0.006
	5	17825.473	0.007		10	18614.341	-0.003
	6	17831.482	0.003		11	18620.430	-0.002
	7	17837.477	0.004		12	18626.492	-0.010
	8	17843.455	0.006		13	18632.535	-0.020
	9	17849.416	0.010		14	18638.562	-0.030
	10	17855.348	0.003		15	18644.568	-0.044
	11	17861.263	-0.003		16	18650.555	-0.061
	12	17867.163	-0.005		17	18656.524	-0.080
	13	17873.044	-0.009		18	18662.473	-0.103
	14	17878.908	-0.013		19	18668.403	-0.129
	15	17884.749	-0.021		20	18674.311	-0.163
	16	17890.572	-0.030		21	18680.203	-0.197
	17	17896.377	-0.041		22	18686.071	-0.239
	18	17902.161	-0.055		23	18691.921	-0.286
Q_{12}	0	17796.210	0.000		24	18697.751	-0.338
	1	17802.301	-0.002		25	18703.559	-0.399
	2	17808.376	-0.001		26	18709.338	-0.473
	3	17814.431	0.000		27	18715.113	-0.540
	4	17820.465	-0.001		28	18720.859	-0.621
	5	17826.481	-0.003		29	18726.583	-0.712
	6	17832.480	-0.001		30	18732.280	-0.816
	7	17838.458	-0.002		31	18737.953	-0.932
	8	17844.419	-0.003		32	18743.607	-1.055
	9	17850.361	-0.002		33	18749.235	-1.193
	10	17856.282	-0.005		34	18754.834	-1.347
	11	17862.186	-0.008		35	18760.407	-1.517
	12	17868.072	-0.010	Q_2	0	18553.569	0.001
	13	17873.937	-0.015		1	18559.823	0.004
	14	17879.786	-0.019		2	18566.054	0.002
	15	17885.613	-0.027		3	18572.267	0.001
	16	17891.421	-0.037		4	18578.466	0.004
	17	17897.212	-0.047		5	18584.643	0.004
	18	17902.984	-0.058		6	18590.804	0.006
P_2	0	18529.547	0.009		7	18596.941	0.001
	1	18536.062	0.014		8	18603.063	0.000
	2	18542.555	0.015		9	18609.171	0.002

Table 4.1. (Continued).

Branch	(v,v)	Expt (cm^{-1})	Expt–Calc. (cm^{-1})	Branch	(v,v)	Expt (cm^{-1})	Expt–Calc. (cm^{-1})
P2	3	18549.029	0.016	Q2	10	18615.252	-0.005
	4	18555.485	0.014		11	18621.318	-0.010
	5	18561.921	0.007		12	18627.365	-0.017
	6	18568.334	0.006		13	18633.414	-0.005
	7	18574.735	0.007		14	18639.410	-0.030
	8	18581.115	0.006		15	18645.501	0.057
	9	18587.475	-0.006		16	18651.363	-0.068
	10	18593.819	-0.012				

bandheads for the branches P_{12}, P_1, Q_{12}, P_2, P_{21}, and Q_2 were recorded for the (v,v) bands with v between 0 and 35 (see Fig. 4.3b). Table 4.1 lists the observed bandhead positions.

Beam - gas experiments yielded SDLIF spectra of individual P_{12}, R_1, P_2, and R_{21} branches in the (0,0), (1,1), (4,4), (8,8), and (12,12) bands. Those scans were often interrupted by branches belonging to other bands that fulfilled the same conditions for excitation and emission as the ones under study (see Fig 4.5).

Line positions were determined from the spectra by locating the center of gravity of each line profile. These direct measurements were corrected by the amount of shift required to make our measurements of the I_2 transitions in the $B^3\Pi_{0_u}^+$ - $X^1\Sigma_g^+$ band system coincide with the published values [18]. We estimated the overall error in the line positions to be 0.003 cm^{-1} for most transitions.

Despite the fact that the probe beam was always perpendicular to the reagent beams, hyperfine structure was hard to observe, because the angular spread in the molecular beams caused some Doppler-broadening. Moreover, it was of no consequence to our studies which aimed to record rotational population distributions. Hyperfine structure was observed in a few occasions and was resolved only in the (0,0) P_{12} branch during a crossed beam experiment (see Fig. 4.6).

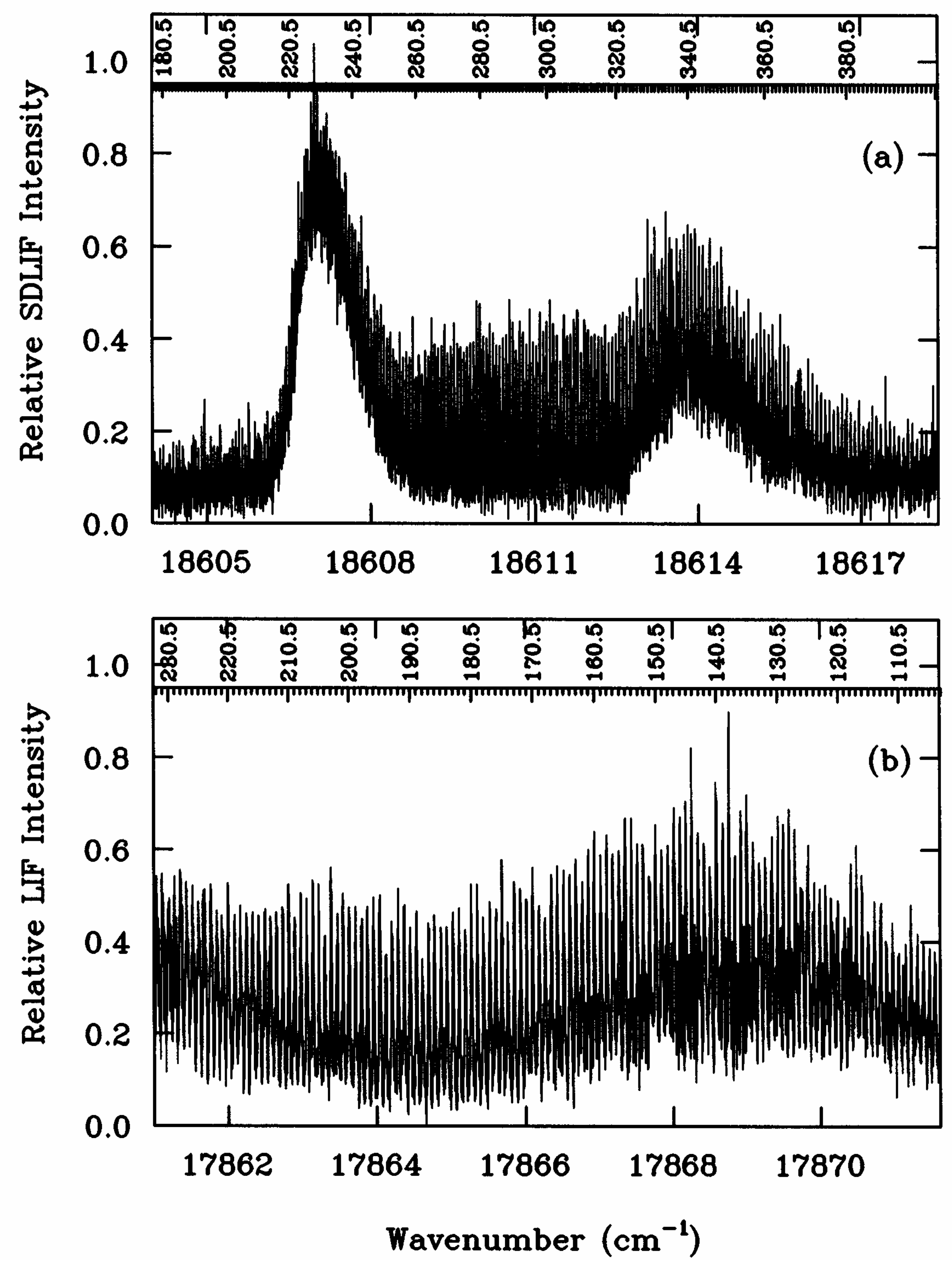

Figure 4.5. SDLIF spectra of BaI $C^2\Pi$ - $X^2\Sigma^+$ (v,v) sequence. (a) (4,4) R_{21}(J) branch members for J values in the range and (b) (12,12) P_{12} branch members for J values between . The broad features are characteristic of interference from "crossing" branches.

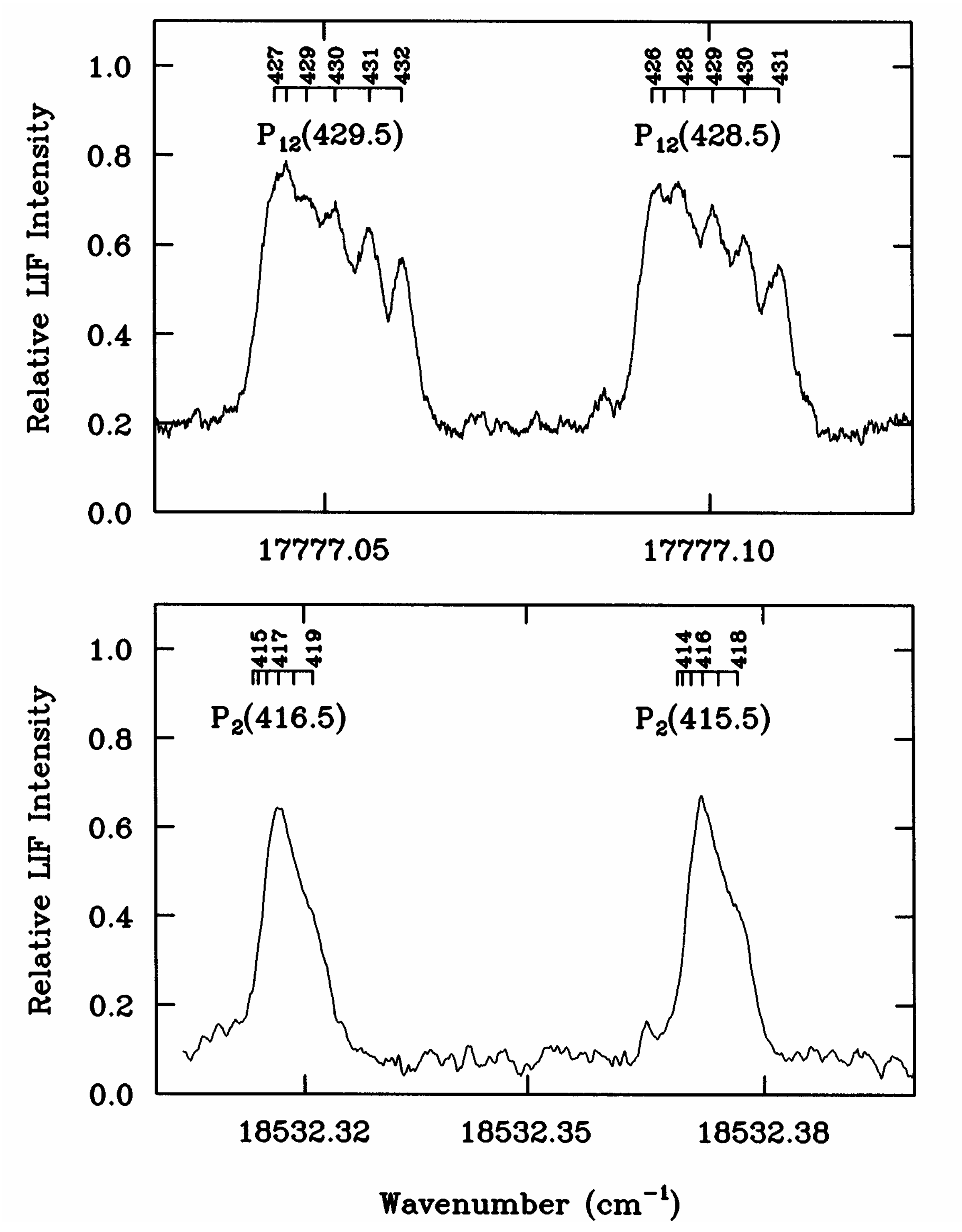

Figure 4.6. Hyperfine structure of (a) (0,0) P_{21} and (b) (0,0) P_2 branch members. These spectra were recorded during separate crossed-beam experiments. P_2 lines are not resolved because hyperfine splittings in the $C^2\Pi_{3/2}$ levels are smaller than in the $C^2\Pi_{1/2}$ levels.

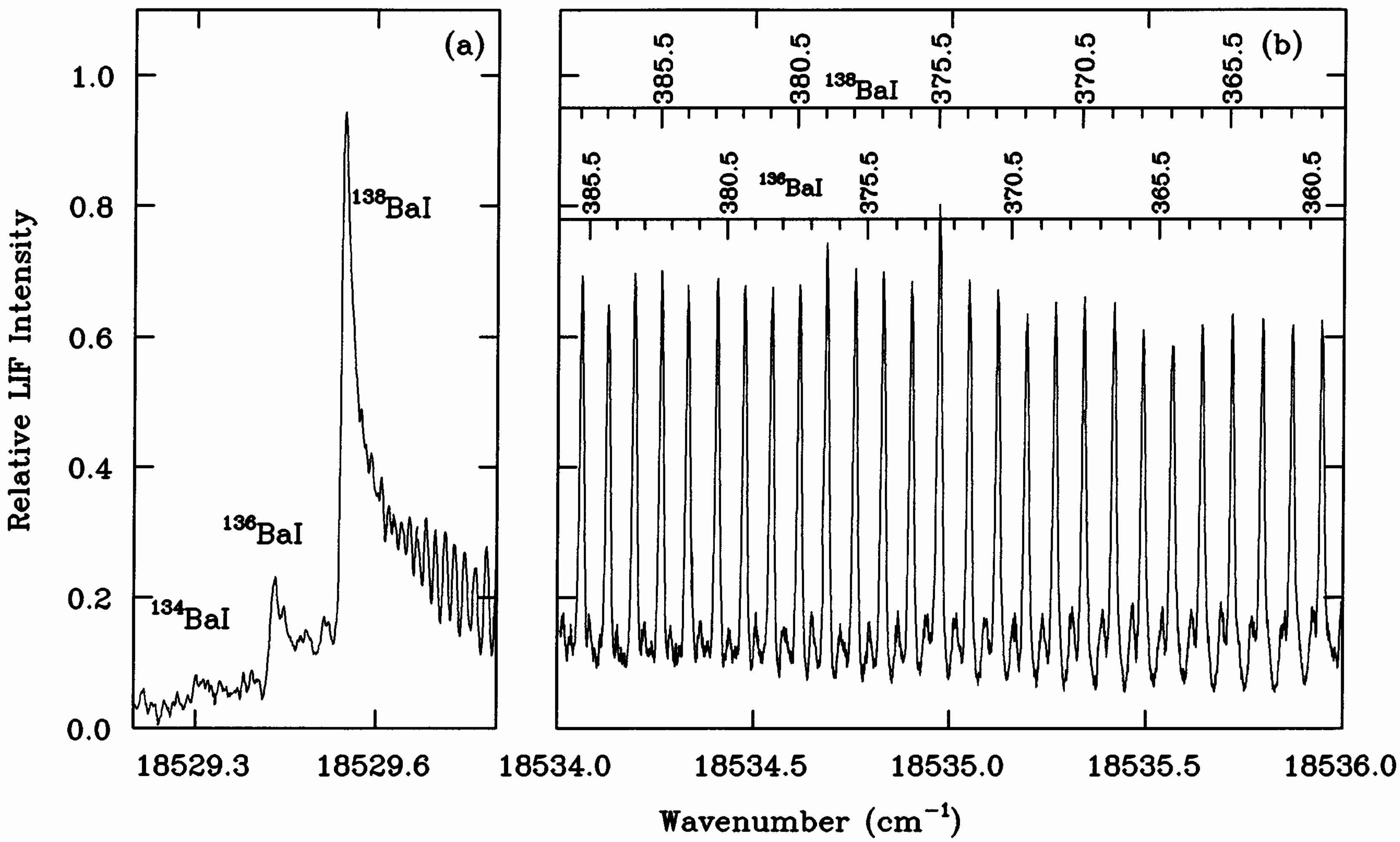

Figure 4.7. Spectra of BaI isotopomers. (a) ^{A}Ba^{127}I $C^2\Pi_{3/2}$ - $X^2\Sigma^+$ (0,0) P_2 bandheads for A = 134, 136, and 138.

(b) ^{136}Ba^{127}I $C^2\Pi_{3/2}$ - $X^2\Sigma^+$ (0,0) P_2 branch members interspersed between ^{138}Ba^{127}I lines of the same branch.

Of great interest were transitions which were attributed to isotopomers of BaI, viz. ^{136}BaI and ^{134}BaI. Such individual transitions were identified in the (0,0) P_{12} and P_2 branches as well as bandheads of the same branches (see Fig. 4.7).

A brief survey of off-diagonal transitions (i.e., with $\Delta v \neq 0$) was done, but they were not included in the following analysis. Bandheads of the $C^2\Pi_{3/2}$ - $X^2\Sigma^+$ ($\Delta v = -1$) were recorded at the following wavenumbers: (7,8) P_{21} at 18455.894 cm^{-1}, (7,8) Q_2 at 18456.544 cm^{-1}, and (3,4) Q_2 at 18430.804 cm^{-1}.

Spectroscopic Constants

The first stage of the analysis of the data required assigning rotational quantum numbers to the observed transitions. An approximate assignment was achieved by simulating line positions using the constants that had been previously determined based on previous, limited data sets. This assignment was checked and refined by fitting all available data to model Hamiltonians [19-21](See Appendix A). The process was repeated each time a set of new data became available. Each time we made sure that no patterns appeared in the fit residuals that would indicate an error in the assignment or a high-order constant missing from the Hamiltonian.

The procedure described above applies to the (0,0) and (8,8) bands for which preliminary constants were available. A similar procedure was followed when data from other bands were included. Then, the constants specific to a vibrational band were expressed as a power series of the vibrational quantum number, in a manner similar to the Dunham expansion [22] of rovibrational energy levels of a $^1\Sigma^+$ diatomic molecule.

Depending on the range of rotational lines in each band and the effect in the quality of fit higher order terms were added or not. All available data are outlined in Table 4.2. They comprise a compilation of the data from Refs. [10-13]. Included in the fit were microwave transitions by Törring and Döbl [23] and bandhead positions from Table 4.1 for $v \leq 12$. The derived set of spectroscopic constants is given in Table 4.3.

Table 4.2. Optical transitions that were available for the determination of the spectroscopic constants of the BaI $C^2\Pi$ - $X^2\Sigma^+$ band system.

Band	Branch	Members	Range of J"
(0,0)	P_{12}	239	22.5-155.5, 341.5-491.5
	P_1	30	46.5-48.5, 404.5-431.5
	Q_{12}	227	4.5-90.5, 353.5-428.5, 462.5-531.5
	Q_1	93	20.5-112.5
	R_{12}	4	42.5-45.5
	R_1	303	31.5-377.5
	P_2	308	6.5, 8.5, 43.5-49.5, 61.5-127.5, 214.5-490.5
	P_{21}	75	7.5, 10.5, 16.5, 40.5-54.5, 373.5-430.5
	Q_2	79	37.5-53.5, 359.5-423.5
	Q_{21}	7	41.5-47.5
	R_2	3	43.5-45.5
	R_{21}	202	41.5-48.5, 124.5-210.5, 237.5-370.5
(1,1)	P_{12}	113	351.5-465.5
	P_2	383	44.5-468.5
(2,2)	P_{12}	111	337.5-447.5
	P_2	113	327.5-440.5
(3,3)	P_{12}	69	356.5-424.5
	P_2	34	392.5-432.5
(4,4)	P_2	302	114.5-423.5
	R_{21}	259	123.5-411.5
(8,8)	P_{12}	148	36.5-190.5
	P_1	2	50.5, 54.5
	Q_{12}	151	29.5-186.5
	Q_1	218	13.5-271.5
	R_{12}	2	49.5, 53.5
	R_1	291	47.5-341.5
	P_2	269	41.5-354.5
	P_{21}	1	51.5
	Q_2	1	50.5
	Q_{21}	2	49.5, 51.5
	R_2	2	48.5, 50.5
	R_{21}	229	49.5, 117.5-359.5
(12,12)	P_{12}	127	104.5-232-5
	P_1	172	122.5-302.5
	R_2	245	57.5-298.5
	R_{21}	218	67.5-286.5

Table 4.3. Spectroscopic constants in cm^{-1} for the BaI $C^2\Pi$ - $X^2\Sigma^+$ band system.

$\Delta\nu$	$18188.4943(3)$	q'_{00}	$-1.374(328) \times 10^{-6}$
$\Delta\omega_e$	$5.63482(13)$	q'_{10}	$5.43(398) \times 10^{-8}$
$\Delta\omega_e x_e$	$2.5283(116) \times 10^{-3}$	q'_{01}	$7.76(183) \times 10^{-12}$
A'_{00}	$7.560594(5) \times 10^{+2}$	p'_{00}	$7.0247(39) \times 10^{-3}$
A'_{10}	$1.09045(148) \times 10^{-1}$	p'_{10}	$-4.235(40) \times 10^{-5}$
A'_{20}	$1.676(11) \times 10^{-3}$	p'_{01}	$-3.224(31) \times 10^{-9}$
A'_{01}	$-4.0716(108) \times 10^{-6}$	Y''_{01}	$2.6805878(8) \times 10^{-2}$
A'_{11}	$3.8206(107) \times 10^{-7}$	Y''_{11}	$-6.6342(3) \times 10^{-5}$
A'_{02}	$7.253(51) \times 10^{-12}$	Y''_{21}	$3.397(32) \times 10^{-8}$
Y'_{01}	$2.672800(17) \times 10^{-2}$	Y''_{02}	$-3.3288(10) \times 10^{-9}$
Y'_{11}	$-6.3610(22) \times 10^{-5}$	Y''_{12}	$-1.31(29) \times 10^{-12}$
Y'_{21}	$2.50(5) \times 10^{-8}$	Y''_{03}	$-1.272(80) \times 10^{-16}$
Y'_{02}	$-3.0726(14) \times 10^{-9}$	g''_{02}	$2.53294(36) \times 10^{-3}$
Y'_{12}	$-1.693(295) \times 10^{-12}$	g''_{10}	$-1.124(11) \times 10^{-5}$
Y'_{22}	$1.06(22) \times 10^{-14}$	g''_{01}	$-3.82(11) \times 10^{-10}$
Y'_{03}	$-1.032(80) \times 10^{-16}$		
ω'_e	157.775	ω''_e	152.140
$\omega'_e x'_e$	0.2771	$\omega''_e x''_e$	0.2746

Numbers in parentheses represent two standard deviations in units of the last figure quoted. Values for ω'_e and $\omega'_e x'_e$ were calculated based on ω''_e and $\omega''_e x''_e$ taken from Ref. [23] and $\Delta\omega_e$ and $\Delta\omega_e x_e$.

Discussion

The sizes of most of spectroscopic constants come as no surprise considering what was known about them before our studies. The C and X states have very similar potential energy surfaces. The small differences in the values of ω_e, $\omega_e x_e$, B, D, and H in the two states attests to that fact. The large value of the ration A/B for the vibrational levels of the C state makes that state a very good example of Hund's case a coupling scheme.

The success of the fit to the generalized Hamiltonians (see Eqs. A.1-9) confirm the inherent assumptions that no frequency perturbations are present in the data and that all constants vary smoothly with v. Another implicit assumption is the separability of the vibrational and rotational energy terms. The validity of this assumption is surprising in light of the following observation. When a molecule is at the ($X^2\Sigma^+$, v=0, N=494) level, it has 76 cm^{-1} and 6388 cm^{-1} of vibrational and rotational energy respectively. Its rotational period is about 1.3 ps long which is merely 6 times longer than its vibrational period. For the ($X^2\Sigma^+$, v=0, N=1) state the same ratio is close to 2000. Yet, the model Hamiltonians which are based on perturbation expansions simulate the data within experimental error.

Two spectroscopic constants are worthy of special comment. $Y'_{2\,2}$ was included in the fit but not $Y''_{2\,2}$ because the two parameters are highly correlated when both are included. The value of $Y'_{2\,2}$ should be regarded as $Y'_{2\,2}$ - $Y''_{2\,2}$ because their difference is determined better than either separately. The differences between the same upper and lower state rotational constant are all better determined than the absolute values of the rotational constants, which is why more significant figures are included in the results than justified by their uncertainties [24]. The value of q'_0 obtained from the fit is determined to be -1.3×10^{-6} cm^{-1} which is a factor of seven smaller than the value determined previously in fitting the (0,0) band [12]. This is a consequence of including more data in the present analysis. Previously no high J" data were included in the (0,0) Q_{12}, P_1, R_1, Q_2, and P_{21} branches; thus q'_v is shown to be very sensitive to the exact data included. The new value is closer to the order of magnitude expected from the value of p'_0 and an estimate from the unique perturber approximation [11,12,24].

The data analyzed are only a sample of all the possible transitions in the twelve branches of each Δv=0 band between v=0 and 12. They are also strongly biased in favor of the branches that can be measured by SDLIF (P_{12}, R_1, P_2, and R_{21}). The parameters in Table 4.3 should give good predictions for these four branches at intermediate v values in Δv=0 bands. Accurate predictions of the other eight branches are not guaranteed.

In addition to the experimental bandhead positions of the P_{12}, P_1, Q_{12}, P_2, P_{21}, and Q_2 branches, Table 4.1 lists the differences between experimental and calculated bandhead positions. The calculated bandhead positions for the (0,0) band compare very well with experiment, considerably better than in our earlier analysis [12] which only included high J" data on two of the branches. We now have data close to the bandheads in all six branches which form bandheads including some Q_{12} branch members that are above the bandhead. The agreement between theory and experiment deteriorates progressively as v increases but is still good until above v = 18 (see Table 4.1). Calculations of the bandhead positions of each branch show that as v increases the J" value at the bandhead decreases.

Törring and Döbl had calculated the vibrational constants for the $X^2\Sigma^+$ state. We combined their values with the values we determined for $\Delta\omega_e$ and $\Delta\omega_e x_e$ and calculated the vibrational constants for the $C^2\Pi$ state. Knowledge of the individual vibrational constants in both states allows us to calculate any off-diagonal transition. The following observations confirm the precision of this calculation. The (7,8) P_{21} bandhead was observed at 18455.894 cm^{-1} and the calculated value was 18455.996 cm^{-1}. Similarly, the corresponding values for the (7,8) Q_2 bandhead were 18456.544 cm^{-1} and 18456.645 and for the (3,4) Q_2 bandhead 18430.804 cm^{-1} and 18430.856 cm^{-1}.

The derived set of Dunham coefficients can be used to predict the wavenumbers of rovibronic transitions of the other isotopomers of BaI. Only ^{127}I exists naturally, with mass 126.9044 and spin $^5/_2$. Five barium isotopes have natural abundances greater than 1 %, as given in Table 4.4. Transitions that can be attributed to isotopomers other than ^{138}BaI have been observed. A regular sequence of lines has been recorded in the (0,0) P_{12} and P_2 branches that coincide with the predicted line positions of ^{136}BaI (see Fig. 4.7b). In the vicinity of 18535.0 cm^{-1} the P_2 (372.5) line of ^{136}BaI is between the P_2 (374.5) and P_2 (375.5) lines of ^{138}BaI.

Table 4.4. Properties of Ba isotopes and BaI isotopomers.

Isotope	Abundance %	Atomic Mass (amu)	μ(BaI) (amu)	ρ	I
^{130}Ba	0.1	129.9062	64.1939	1.014647	0
^{132}Ba	0.1	131.9057	64.6784	1.010839	0
^{134}Ba	2.4	133.9043	65.1552	1.007134	0
^{135}Ba	6.6	134.9056	65.3914	1.005313	3/2
^{136}Ba	7.9	135.9044	65.6251	1.003521	0
^{137}Ba	11.2	136.9055	65.8577	1.001748	3/2
^{138}Ba	71.7	137.9055	66.0881	1.000000	0

Table 4.5. Experimental bandhead shifts of BaI isotopomer and differences from calculated values.

	(138)–(136)		(138)–(134)	
Branch	Expt (cm^{-1})	Expt–Calc. (cm^{-1})	Expt (cm^{-1})	Expt–Calc. (cm^{-1})
P_{12}	0.1125	-0.0034	0.2314	-0.0035
P_1	0.0337	-0.0031	0.0718	-0.0029
Q_{12}	0.0265	-0.0062	0.0640	-0.0022
P_2	0.1147	-0.0033	0.2374	-0.0018
P_{21}	0.0264	-0.0024	0.0554	-0.0030
Q_2	0.0210	-0.0037		

More pronounced is the isotopic shift of bandheads. The effect on the (0,0) P_{12} and P_2 branches is easiest to observe because the shifted bandheads appear before the onset of branches of the most abundant isotopomer. Figure 4.7a shows the (0,0) P_2 bandheads for ^{138}BaI, ^{136}BaI, and ^{134}BaI. All six bandheads for ^{136}BaI and five for ^{134}BaI have been observed in the (0,0) band, and the isotopic shifts are given in Table 4.5.

Isotopic shifts were calculated using ρ values given in Table 4.4, where ρ is defined as $(\mu/\mu^i)^{1/2}$, μ is the reduced mass of ^{138}BaI, and μ^i is that of the isotopomer of interest . The following powers of ρ were used to adjust the Dunham coefficients: 0 for Δν, A_{00}; 1 for A_{10}, Y_{10}; 2 for A_{20}, A_{01}, Y_{20}, Y_{01}, p_{00}, γ_{00}; 3 for A_{11}, Y_{11}, p_{10}, γ_{01}; 4 for A_{21}, A_{02}, Y_{21}, Y_{02}, q_{00}, p_{01}, γ_{01}; 5 for Y_{12}, q_{10}, p_{11}; 6 for Y_{22}, Y_{03}, q_{01} [25]. The calculated shifts are also presented in Table 4.5. The agreement is good though there appears to be a small constant offset. The relative intensities of those bandheads follow the order of natural abundance of the corresponding Ba isotopes, but the bandheads of the less abundant isotopomers appear stronger than expected. P_2 and P_{21} bandheads of higher (v,v) bands have been observed, but no detailed study has been attempted.

None of the observed transition wavenumbers could be assigned to ^{137}BaI or ^{135}BaI. We believe this absence is because odd-mass Ba isotopes have nuclear spin $^{3}/_{2}$ so that hyperfine coupling would split each energy level into four. Although no Ba hyperfine coupling constants are available for any BaX (X = F, Cl, Br) $C^2\Pi$ state, the largest hyperfine interaction of the BaX $X^2\Sigma^+$ state arises from the Fermi contact constant, that has an average value of 2307 MHz [26]. In the event that the energy level splitting in the $C^2\Pi$ state were negligible compared to that of the $X^2\Sigma^+$ state, adjacent hyperfine components of $C^2\Pi$ - $X^2\Sigma^+$ rovibronic transitions would be separated by approximately 0.04 cm^{-1}. The unobserved transitions could coincide with those of other isotopomers. Such coincidences could account for the high intensities of the bandheads for low abundance isotopomers.

In conclusion, we have been able to fit 5032 transitions using 31 spectroscopic constants with an overall standard deviation of 0.0024 cm^{-1}. Furthermore, this set of constants can predict line positions in many bands not yet studied. These predictions facilitated the assignment of newly observed, unexplored branches in many bands with high level of confidence. In fact, such branches have been observed in (v,v) bands with v as high as 20 and have been assigned . It is only a matter of time to incorporate them in the main body of data to get a new improved set of spectroscopic constants.

References

1 C. M. Olmstead, *Z. wiss. Photogr.* **4**, 255 (1906).

2 O. H. Walters and S. Barratt, *Proc. Roy. Soc. London A* **118**, 120 (1928).

3 P. Mesnage, *Ann. Phys.* **12**, 5 (1939).

4 M. M. Patel and N. R. Shah, *Ind. J. Pure Appl. Phys.* **8**, 681 (1970).

5 S. G. Shah, M. M. Patel, and A. B. Darji, *J. Phys. B: Atom. Molec. Phys.* **5**, L191 (1972)

6 S. G. Shah and M. M. Patel, *Ind. J. Pure Appl. Phys.* **15**, 728 (1977).

7 M. L. P. Rao, D. V. K. Rao, P. T. Rao, and P. S. Murty, *Fizika* **9**, 25 (1977).

8 W. T. M. L. Fernando, M. Douay, and P. F. Bernath, *J. Mol. Spectrosc* **144**, 344 (1990).

9 M. A. Johnson, C. W. Webster, and R. N. Zare, *J. Chem. Phys.* **75**, 5575 (1981); M. A. Johnson and R. N. Zare, *J. Chem. Phys.* **82** , 4449 (1985).

10 M. A. Johnson, C. Noda, J. S. McKillop, and R. N. Zare, *Can. J. Phys.* **62**, 1467 (1984).

11 C. A. Leach, J. R. Waldeck, C. Noda, J. S. McKillop, and R. N. Zare, *J. Mol. Spectrosc.* **146**, 465 (1991).

12 D. Zhao, P. H. Vaccaro, A. A. Tsekouras, C. A. Leach, and R. N. Zare, *J. Mol. Spectrosc.* **148**, 226 (1991).

13 C. A. Leach, A. A. Tsekouras, and R. N. Zare, *J. Mol. Spectrosc.* **153**, 59 (1992).

14 G. Herzberg, "Molecular Spectra and Molecular Structure, I. Spectra of Diatomic Molecules", Krieger, Malabar, 1989.

15 P. J. Dagdigian, H. W. Cruse, and R. N. Zare, *J. Chem. Phys.* **60**, 2330 (1974).

16 W. E. Ernst, J. Kändler, C. Noda, J. S. McKillop, and R. N. Zare, *J. Chem. Phys.* **85** , 3735 (1986); C. A. Leach, W. E. Ernst, J. Kändler, C. Noda, J. S. McKillop, and R. N. Zare, *J. Chem. Phys.*, **95**, 9433 (1991).

17 C. Linton, J. Mol. Spectrosc. 69, 351 (1978); M. Dulick, P. F. Bernath, and R. W. Field, Can. J. Phys. 58, 703 (1980).

18 S. Gerstenkorn and P. Luc, "Atlas du Spectre d'Absorption de la Molécule d'Iode", Centre National de la Recherche Scientifique, Paris, 1978; S. Gerstenkorn and P. Luc, *Rev. Phys. Appl.* **14**, 791 (1979).

19 R. N. Zare, A. L. Schmeltekopf, W. J. Harrop, and D. L. Albritton, *J. Mol. Spectrosc.* **46**, 37 (1973).

20 A. J. Kotlar, R. W. Field, J. I. Steinfeld, and J. A. Coxon, *J. Mol. Spectrosc.*, **80**, 86 (1980).

21 J. H. Van Vleck, *Phys. Rev.*, **33**, 467 (1929).

22 J. L. Dunham,. *Phys. Rev.*, **41**, 721 (1932).

23 T. Törring and K. Döbl, *Chem. Phys. Lett.* **115**, 328 (1985).

24 D. L. Albritton, A. L. Schmeltekopf, and R. N. Zare, "Molecular Spectroscopy: Modern Research," K. Narahari Rao, ed., **II**, 1, Academic Press, New York, 1976.

25 C. H. Townes and A. L. Schawlow, "Microwave Spectroscopy," Dover, New York, 1975.

26 Ch. Ryzlewicz, H.-U. Schütze-Pahlmann, J. Hoeft, and T. Törring, *Chem Phys.*, **71**, 389 (1982); W. E. Ernst, G. Weiler, and T. Törring, *Chem Phys. Lett.*, **121**, 494 (1985).

Appendix A. The C $^2\Pi$ and X $^2\Sigma^+$ Hamiltonians

The X $^2\Sigma^+$ state follows Hund's case b coupling scheme. If hyperfine splittings are not taken into account, the rotational energy levels for the $^2\Sigma^+$ state are given by the expressions [14, 19, 20]:

$$E(F_1) = B_v N (N+1) - D_v [N (N+1)]^2 + H_v [N (N+1)]^3 + {}^1/_2 [\gamma_v + \gamma_{Dv} N (N+1)] N$$

$$\text{with } J = N + {}^1/_2 \qquad \text{(A.1a)}$$

$$E(F_2) = B_v N (N+1) - D_v [N (N+1)]^2 + H_v [N (N+1)]^3 - {}^1/_2 [\gamma_v + \gamma_{Dv} N (N+1)] (N+1)$$

$$\text{with } J = N - {}^1/_2 \qquad \text{(A.1b)}$$

The C$^2\Pi$ state follows Hund's case a coupling scheme, since it has strong spin-orbit coupling (A = 756 cm^{-1}). The $^2\Pi$ state energy levels are calculated by diagonalizing a 2x2 matrix using the spin-orbit terms as a basis set [17].[1]

$$H_{11}=\langle ^2\Pi_{1/2}|\mathcal{H}|^2\Pi_{1/2}\rangle \qquad \text{(A.2a)}$$

$$H_{22}=\langle ^2\Pi_{3/2}|\mathcal{H}|^2\Pi_{3/2}\rangle \qquad \text{(A.2a)}$$

$$H_{12}=\langle ^2\Pi_{1/2}|\mathcal{H}|^2\Pi_{3/2}\rangle \qquad \text{(A.2a)}$$

$$\begin{aligned} H_{11} = &-{}^1/_2 [A_v + A_{Dv} x^2 + A_{Hv} (x^4+x^2-1)] \\ &+ B_v x^2 - D_v (x^4+x^2-1) + H_v[x^6+(x^2-2) (x^2-1)] \\ &+ {}^1/_2 p_v (1\pm x) + {}^1/_2 p_{Dv}(1\pm x)(x^2-{}^1/_4) + {}^1/_2 q_v (1\pm x)^2 + {}^1/_2 q_{Dv} (1\pm x)^2(x^2-{}^1/_4) \end{aligned} \qquad \text{(A.3a)}$$

$$\begin{aligned} H_{22} = &{}^1/_2 (A_v + A_{Dv} (x^2-2) + A_{Hv} [(x^2-2)^2 +x^2-1]) \\ &+ B_v (x^2 -2) - D_v [(x^2-2)^2 +x^2-1] + H_v [(x^2-2)^2+2(x^2-2) (x^2-1)+x^2(x^2-1)] \\ &+ {}^1/_2 q_v (x^2 -1) + {}^1/_2 q_{Dv} (x^2-1)(x^2-{}^1/_4) \end{aligned} \qquad \text{(A.3b)}$$

$$H_{12} = H_{21} = -B_v\sqrt{x^2-1} +2D_v\sqrt{x^2-1}(x^2-1) -H_v\sqrt{x^2-1} [(x^2-2)^2+x^2(x^2-2)+2(x^2-1)+x^4]$$

---

[1] References are found at the end of Chapter 4.

$$-{}^{1}/_{4}p_{v}\sqrt{x^{2}-1}\ -{}^{1}/_{4}p_{Dv}(x^{2}-{}^{1}/_{4})-{}^{1}/_{2}q_{v}\sqrt{x^{2}-1}(1\pm x)\ -{}^{1}/_{2}q_{Dv}\sqrt{x^{2}-1}(1\pm x)(x^{2}-{}^{1}/_{4}) \tag{A.3c}$$

where $x = J + {}^{1}/_{2}$ and the double signs refer to different Λ-doublets. Van Vleck transformations have removed off-diagonal blocks arising from interactions between different vibrational levels or different electronic states. The latter are treated in the unique perturber approximation which is described by the phenomenological constants o, p, and q. The Λ-doubling constants o and o_D were not included because they could not be determined independently in the single perturber approximation. The rotational energy levels are given by the expression:

$$E(^{2}\Pi) = {}^{1}/_{2}\,(H_{11} + H_{22}) \pm {}^{1}/_{2}\sqrt{(H_{22}-H_{11})^{2}+4H_{12}^{2}} \tag{A.4}$$

where the + sign refers to the $^{2}\Pi_{3/2}$ state and the - sign to the $^{2}\Pi_{1/2}$ state.

The transition wavenumbers are calculated by taking the appropriate differences of energy levels in the C and X states as shown in Fig. A.1.

$$\Delta E = E(^{2}\Pi,J) - E(^{2}\Sigma,J) \tag{A.5}$$

When data from more than one vibrational band were included, we used the following expressions for the vibrational and the total energy of a rovibronic level:

$$E_{vib} = \omega_{e}\,(v+{}^{1}/_{2}) - \omega_{e}x_{e}\,(v+{}^{1}/_{2})^{2} \tag{A.6}$$

$$E_{tot} = E_{el} + E_{vib} + E_{rot} \tag{A.7}$$

where the appropriate expressions for E_{rot} are substituted from Eqs. (A.1) or (A.4) and $E_{el} = T_{e} + Y_{00}$.

The rotational constants can be written as a power series in v [20, 22].

$$B_{v} = Y_{01} + Y_{11}\,(v+{}^{1}/_{2}) + Y_{21}\,(v+{}^{1}/_{2})^{2} \tag{A.8a}$$

$$D_{v} = -[Y_{02} + Y_{12}\,(v+{}^{1}/_{2}) + Y_{22}\,(v+{}^{1}/_{2})^{2}] \tag{A.8b}$$

$$H_{v} = Y_{03} \tag{A.8c}$$

$$\gamma_v = G_{00} + G_{10} (v+{}^1/_2) \tag{A.8d}$$

$$\gamma_{Dv} = G_{01} \tag{A.8e}$$

$$A_v = A_{00} + A_{10} (v+{}^1/_2) + A_{20} (v+{}^1/_2)^2 \tag{A.8f}$$

$$A_{Dv} = A_{01} + A_{11} (v+{}^1/_2) \tag{A.8g}$$

$$A_{Hv} = A_{02} \tag{A.8h}$$

$$p_v = p_{00} + p_{10} (v+{}^1/_2) \tag{A.8i}$$

$$p_{Dv} = p_{01} \tag{A.8j}$$

$$q_v = q_{00} + q_{10} (v+{}^1/_2) \tag{A.8k}$$

$$q_{Dv} = q_{01} \tag{A.8l}$$

Similarly, band origins are expressed as:

$$\nu_{vv} = \Delta\nu + \Delta\omega_e (v+{}^1/_2) - \Delta\omega_e x_e (v+{}^1/_2)^2 \tag{A.8m}$$

The vibrational constants appear only in differences because only $\Delta v = 0$ data were used in the fit.

$$\Delta\omega_e = \Delta\omega_e' - \Delta\omega_e'' \tag{A.9a}$$

$$\Delta\omega_e x_e = \Delta\omega_e' \; x_e' - \Delta\omega_e'' \; x_e'' \tag{A.9b}$$

Also since only one band system was considered

$$\Delta\nu = T_e' - T_e'' + Y_{0\,0}' - Y_{0\,0}'' \tag{A.9c}$$

where, of course, $T_e'' = 0$.

Appendix B. Computer Code for Spectroscopic Calculations

The following program listings include the computer code written in FORTRAN language to calculate energy levels, transition wavenumbers, and rotational line strengths for a $^2\Pi$ - $^2\Sigma$ band system. All routines are Fortran functions and all have hyperfine counterparts where the total angular momentum quantum number F can be specified. An example of how these routines can be used is given in the program FORTRATS.FOR which calculates Fortrat diagrams for a range of bands. The same routines were incorporated in the fitting program used for the determination of the spectroscopic constants.

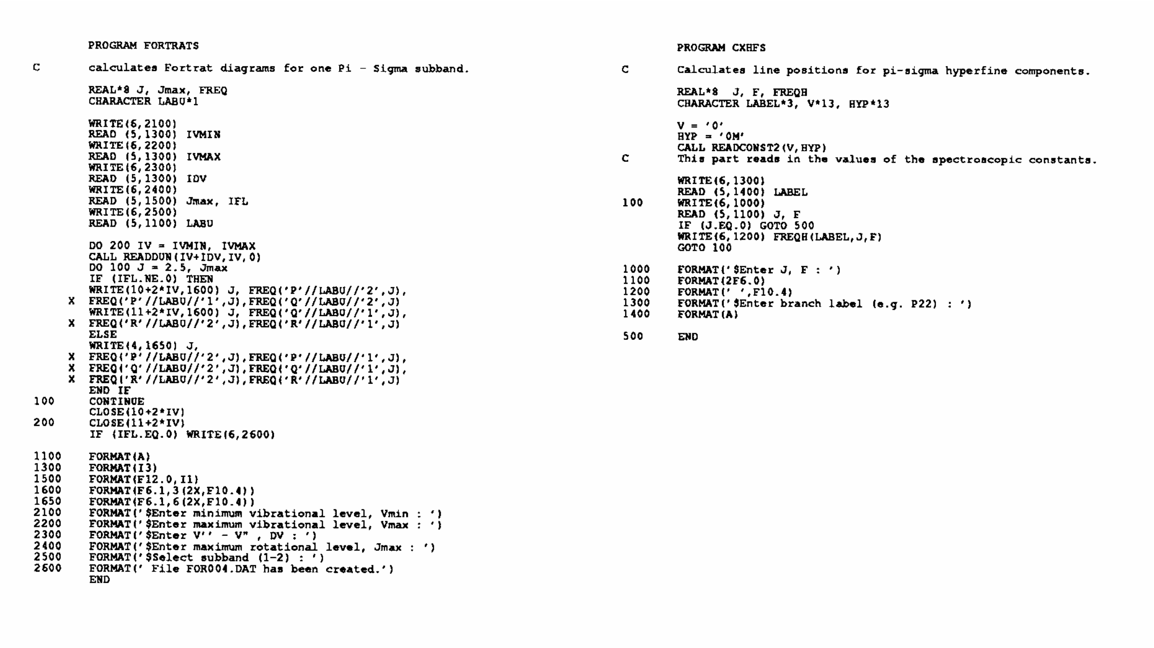

```
        PROGRAM FORTRATS

C       calculates Fortrat diagrams for one Pi - Sigma subband.

        REAL*8 J, Jmax, FREQ
        CHARACTER LABU*1

        WRITE(6,2100)
        READ (5,1300) IVMIN
        WRITE(6,2200)
        READ (5,1300) IVMAX
        WRITE(6,2300)
        READ (5,1300) IDV
        WRITE(6,2400)
        READ (5,1500) Jmax, IFL
        WRITE(6,2500)
        READ (5,1100) LABU

        DO 200 IV = IVMIN, IVMAX
        CALL READDUN(IV+IDV,IV,0)
        DO 100 J = 2.5, Jmax
        IF (IFL.NE.0) THEN
        WRITE(10+2*IV,1600) J, FREQ(’P’//LABU//’2’,J),
     X  FREQ(’P’//LABU//’1’,J),FREQ(’Q’//LABU//’2’,J)
        WRITE(11+2*IV,1600) J, FREQ(’Q’//LABU//’1’,J),
     X  FREQ(’R’//LABU//’2’,J),FREQ(’R’//LABU//’1’,J)
        ELSE
        WRITE(4,1650) J,
     X  FREQ(’P’//LABU//’2’,J),FREQ(’P’//LABU//’1’,J),
     X  FREQ(’Q’//LABU//’2’,J),FREQ(’Q’//LABU//’1’,J),
     X  FREQ(’R’//LABU//’2’,J),FREQ(’R’//LABU//’1’,J)
        END IF
100     CONTINUE
        CLOSE(10+2*IV)
200     CLOSE(11+2*IV)
        IF (IFL.EQ.0) WRITE(6,2600)

1100    FORMAT(A)
1300    FORMAT(I3)
1500    FORMAT(F12.0,I1)
1600    FORMAT(F6.1,3(2X,F10.4))
1650    FORMAT(F6.1,6(2X,F10.4))
2100    FORMAT(’$Enter minimum vibrational level, Vmin : ’)
2200    FORMAT(’$Enter maximum vibrational level, Vmax : ’)
2300    FORMAT(’$Enter V’’ - V" , DV : ’)
2400    FORMAT(’$Enter maximum rotational level, Jmax : ’)
2500    FORMAT(’$Select subband (1-2) : ’)
2600    FORMAT(’ File FOR004.DAT has been created.’)
        END
```

```
        PROGRAM CXHFS

C       Calculates line positions for pi-sigma hyperfine components.

        REAL*8  J, F, FREQH
        CHARACTER LABEL*3, V*13, HYP*13

        V = ’0’
        HYP = ’0M’
        CALL READCONST2(V,HYP)
C       This part reads in the values of the spectroscopic constants.

        WRITE(6,1300)
        READ (5,1400) LABEL
100     WRITE(6,1000)
        READ (5,1100) J, F
        IF (J.EQ.0) GOTO 500
        WRITE(6,1200) FREQH(LABEL,J,F)
        GOTO 100

1000    FORMAT(’$Enter J, F : ’)
1100    FORMAT(2F6.0)
1200    FORMAT(’ ’,F10.4)
1300    FORMAT(’$Enter branch label (e.g. P22) : ’)
1400    FORMAT(A)

500     END
```

```
      REAL*8 FUNCTION LINSTRH(BRANCH,J,F)

C     calculates the F-dependent contribution of line strengths.
C     FACTOR = (2J"+1)(2J'+1)sixJ(J',F',I,F",J",1)^2

      CHARACTER BRANCH*3
      REAL*8 J, F, FACTOR, LINSTR
      PARAMETER I = 2.5

      GOTO (300, 400, 500) ICHAR(BRANCH(1:1))-79
      RETURN

C     P branches
300   FACTOR = (J+F+I)*(J+F-I)*(J+F+I+1)*(J+F-I-1)
     X          /(4*J*F*(2*F-1)*(2*F+1))
      GOTO 700
C     Q branches
400   FACTOR = (2*J+1)*(I*(I+1)-F*(F+1)-J*(J+1))**2
     X          /(4*J*F*(J+1)*(F+1)*(2*F+1))
      GOTO 700
C     R branches
500   FACTOR = (J+F+I+2)*(J+F-I+2)*(J+F+I+3)*(J+F-I+1)
     X          /(4*(J+1)*(F+1)*(2*F+1)*(2*F+3))

700   LINSTRH = LINSTR(BRANCH,J) * FACTOR
      RETURN
      END

*=======================================================================

      REAL*8 FUNCTION LINSTR(BRANCH,J)

C     calculates line strengths for a Sigma - Pi transition
C     Ref.: Zare, Angular Momentum.

      COMMON /STRENGTH/ Y
      CHARACTER BRANCH*3
      REAL*8 J, X, Y

      DECODE (1,1000,BRANCH(2:2)) I1
      DECODE (1,1000,BRANCH(3:3)) I2
      IFL = I1 * 2 + I2 - 2
      GOTO (300, 400, 500) ICHAR(BRANCH(1:1))-79
      RETURN

C     P branches
300   X = DSQRT(4 * (J-1-.5) * (J-1+1.5) + (Y - 2)**2)
      DEN = 32 * J
      JP = 2 * J - 1
      GOTO (311, 312, 321, 322) IFL
311   LINSTR = (JP*JP + JP * (JP*JP-8+2*Y) / X) / DEN
      RETURN
312   LINSTR = (JP*JP - JP * (JP*JP  -2*Y) / X) / DEN
      RETURN
321   LINSTR = (JP*JP - JP * (JP*JP-8+2*Y) / X) / DEN
      RETURN
322   LINSTR = (JP*JP + JP * (JP*JP  -2*Y) / X) / DEN
      RETURN

C     Q branches
400   X = DSQRT(4 * (J-.5) * (J+1.5) + (Y - 2)**2)
      DEN = 32 * J * (J + 1)
      JQ = 2 * J + 1
      GOTO (411, 412, 421, 422) IFL
411   LINSTR = (JQ * (JQ * JQ - 2 + (JQ**3-8*J-8+2*Y) / X)) / DEN
      RETURN


412   LINSTR = (JQ * (JQ * JQ - 2 - (JQ**3-8*J  -2*Y) / X)) / DEN
      RETURN
421   LINSTR = (JQ * (JQ * JQ - 2 - (JQ**3-8*J-8+2*Y) / X)) / DEN
      RETURN
422   LINSTR = (JQ * (JQ * JQ - 2 + (JQ**3-8*J  -2*Y) / X)) / DEN
      RETURN

C     R branches
500   X = DSQRT(4 * (J+1-.5) * (J+1+1.5) + (Y - 2)**2)
      DEN = 32 * (J + 1)
      JR = 2 * J + 3
      GOTO (511, 512, 521, 522) IFL
511   LINSTR = (JR*JR + JR * (JR*JR  -2*Y) / X) / DEN
      RETURN
512   LINSTR = (JR*JR - JR * (JR*JR-8+2*Y) / X) / DEN
      RETURN
521   LINSTR = (JR*JR - JR * (JR*JR  -2*Y) / X) / DEN
      RETURN
522   LINSTR = (JR*JR + JR * (JR*JR-8+2*Y) / X) / DEN
      RETURN

1000  FORMAT(I1)

      END

*=======================================================================

      REAL*8 FUNCTION FREQ(BRANCH,J)

C     Calculates wavenumbers for BaI C2Pi - X2Sigma+

      REAL*8 J, F, FREQH
      CHARACTER BRANCH*3

      F = 0
      FREQ = FREQH(BRANCH,J,F)
      RETURN
      END

*=======================================================================

      REAL*8 FUNCTION FREQH(BRANCH,J,F)

C     Calculates wavenumbers for BaI C2Pi - X2Sigma+
C     Hyperfine structure is included.

      REAL*8 J, F, FFS0P, FFS0M, FFP1P, FFP1M, FFP2P, FFP2M
      CHARACTER BRANCH*3

      DECODE (1,1000,BRANCH(2:2)) I1
      DECODE (1,1000,BRANCH(3:3)) I2
      IFL = I1 * 2 + I2 - 2

      GOTO (300, 400, 500) ICHAR(BRANCH(1:1))-79
      RETURN

300   GOTO (311, 312, 321, 322) IFL
C     P branches
311   FREQH = FFP1M(J-1,F-1) - FFS0M(J,F)
      RETURN
312   FREQH = FFP1P(J-1,F-1) - FFS0P(J,F)
      RETURN
321   FREQH = FFP2M(J-1,F-1) - FFS0M(J,F)
      RETURN
322   FREQH = FFP2P(J-1,F-1) - FFS0P(J,F)
      RETURN

400   GOTO (411, 412, 421, 422) IFL
C     Q branches
411   FREQH = FFP1P(J,F) - FFS0M(J,F)
      RETURN
412   FREQH = FFP1M(J,F) - FFS0P(J,F)
      RETURN
421   FREQH = FFP2P(J,F) - FFS0M(J,F)
      RETURN
422   FREQH = FFP2M(J,F) - FFS0P(J,F)
      RETURN

500   GOTO (511, 512, 521, 522) IFL
C     R branches
511   FREQH = FFP1M(J+1,F+1) - FFS0M(J,F)
      RETURN
512   FREQH = FFP1P(J+1,F+1) - FFS0P(J,F)
      RETURN
521   FREQH = FFP2M(J+1,F+1) - FFS0M(J,F)
      RETURN
522   FREQH = FFP2P(J+1,F+1) - FFS0P(J,F)
      RETURN

1000  FORMAT(I1)

      END

*=======================================================================

      REAL*8 FUNCTION FS0P(J)

      REAL*8 J, F, SOLVES, FS0M, FFS0P, FFS0M

      FS0P = SOLVES(J,0.D0,-1)
      RETURN
      ENTRY FS0M(J)
      FS0M = SOLVES(J,0.D0,+1)
      RETURN
      ENTRY FFS0P(J,F)
      FFS0P = SOLVES(J,F,-1)
      RETURN
      ENTRY FFS0M(J,F)
      FFS0M = SOLVES(J,F,+1)
      RETURN
      END

*=======================================================================

      REAL*8 FUNCTION SOLVES(J,F,IX)

      COMMON /SIROTCON/ ESI, BS, DS, HS, GS, GDS
      COMMON /SIHYPCON/ B, C, Q

      REAL*8 J, F, N, B, C, Q
      REAL*8 BS, DS, HS, GS, GDS, ESI
      REAL*8 H11, H22, H12, J1, J2, CC1, CC2, YY1, YY2, E, D

      N = J - .5 * IX
      H11 = -.5*(GS+GDS*N*(N+1))*(N+1)
      H22 = +.5*(GS+GDS*N*(N+1))* N
      SOLVES = N*(N+1)*(BS + N*(N+1)*(-DS + N*(N+1)*HS)) + ESI
      IF (F.NE.0) GOTO 50
      IF (IX) 10, 100, 20
10    SOLVES = SOLVES + H11
      RETURN
20    SOLVES = SOLVES + H22


      RETURN

50    J1 = N - .5
      J2 = N + .5
      CC1 = F*(F+1)-J1*(J1+1)-8.75
      CC2 = F*(F+1)-J2*(J2+1)-8.75
      YY1 = (3*CC1*(CC1+1)-35*J1*(J1+1))/(320*J1*(J1+1))
      YY2 = (3*CC2*(CC2+1)-35*J2*(J2+1))/(320*J2*(J2+1))
      E = DSQRT((F+N-2)*(F-N+3)*(F+N+4)*(N-F+3))
      D = .15*(F*(F+1)-(N-.5)*(N+1.5)-8.75)/((2*N-1)*(2*N+3))
      H11 = (-B+C/(2*N-1))*CC1/(2*(2*N+1))-Q*YY1+H11
      H22 = ( B+C/(2*N+3))*CC2/(2*(2*N+1))-Q*YY2+H22
      H12 = E/(2*(2*N+1))*(B+.5*C+Q*D)
      SOLVES = SOLVES + .5*(H11+H22+IX*DSQRT((H11-H22)**2+4*H12*H12))
100   RETURN
      END

*=======================================================================

      REAL*8 FUNCTION FP1P(J)

      REAL*8 J,F,SOLVEP, FP1M, FP2P, FP2M, FFP1P, FFP1M, FFP2P, FFP2M

      FP1P = SOLVEP(J,0.D0,+1,-1)
      RETURN
      ENTRY FP1M(J)
      FP1M = SOLVEP(J,0.D0,-1,-1)
      RETURN
      ENTRY FP2P(J)
      FP2P = SOLVEP(J,0.D0,+1,+1)
      RETURN
      ENTRY FP2M(J)
      FP2M = SOLVEP(J,0.D0,-1,+1)
      RETURN

      ENTRY FFP1P(J,F)
      FFP1P = SOLVEP(J,F,+1,-1)
      RETURN
      ENTRY FFP1M(J,F)
      FFP1M = SOLVEP(J,F,-1,-1)
      RETURN
      ENTRY FFP2P(J,F)
      FFP2P = SOLVEP(J,F,+1,+1)
      RETURN
      ENTRY FFP2M(J,F)
      FFP2M = SOLVEP(J,F,-1,+1)
      RETURN
      END

*=======================================================================

      REAL*8 FUNCTION SOLVEP(J,F,S,IX)

      COMMON /ELECTRON/ EPI, A, AD, AH
      COMMON /PIROTCON/ BP, DP, HP
      COMMON /PIHYPCON/ APH, BC, D, Q
      COMMON /PILAMDOU/ Q0, QD, P0, PD, PH, O0, OD, OH

      REAL*8 J, X, H11, H12, H22, DE
      REAL*8 EPI, A, AD, AH, BP, DP, HP
      REAL*8 Q0, QD, P0, PD, PH, O0, OD, OH
      REAL*8 APH, BC, D, Q, F, HYP, HYP1, OM, SIG, CC, YY
      INTEGER*4 S

      X = J+.5
      H22 = (AD*.5+BP)*(X*X-2)+(AH*.5-DP)*((X*X-2)**2+(X*X-1))
```

```
    X   +HP*((X*X-2)**3+2*(X*X-2)*(X*X-1)+X*X*(X*X-1))
    X   +(Q0+QD*(X*X-.25))*(X*X-1)*.5
        H11 = (-AD*.5+BP)*X*X-(AH*.5+DP)*(X**4+(X*X-1))
    X   +HP*(X**6+2*X*X*(X*X-1)+(X*X-2)*(X*X-1))
    X   + O0+(OD+OH*(X*X-.25))*(X*X-.25)
    X   +(P0+(PD+PH*(X*X-.25))*(X*X-.25))*(1+S*X)*.5
    X   +(Q0+ QD                 *(X*X-.25))*(1+S*X)**2*.5
        H12 = -BP*DSQRT(X*X-1)+2*DP*DSQRT(X*X-1)*(X*X-1)
    X   -HP*DSQRT(X*X-1)*((X*X-2)**2+X*X*(X*X-2)+2*(X*X-1)+X**4)
    X   -(P0+(PD+PH*(X*X-.25))*(X*X-.25))*DSQRT(X*X-1)*.25
    X   -(Q0+ QD                 *(X*X-.25))*DSQRT(X*X-1)*.5*(1+S*X)

        IF (F.LE.1) GOTO 100
        SIG = .5 * IX
        OM = 1 + SIG
        CC = F*(F+1)-J*(J+1)-8.75
        YY = (3*CC*(CC+1)-35*J*(J+1))/(80*(2*J-1)*(2*J+3))
        HYP = (APH+BC*SIG)*OM*CC/(2*J*(J+1))-Q*YY*(1-3*OM*OM/(J*(J+1)))
        HYP1 = D * CC * (J + .5) / (4*J*(J+1))
        H11 = H11 + HYP - S * HYP1
        H22 = H22 + HYP

100     SOLVEP = .5*(H11+H22+IX*DSQRT((H11-H22-A)**2+4*H12*H12))+EPI
        RETURN

        END

*=========================================================================

        SUBROUTINE READCONST(V)

C       This part is run once to read in the values of the spectroscopic
C       constants that are used in the following units.

        COMMON /ELECTRON/ EPI, A, AD, AH
        COMMON /PIROTCON/ BP, DP, HP
        COMMON /PILAMDOU/ Q0, QD, P0, PD, PH, O0, OD, OH
        COMMON /PIHYPCON/ APH, BC, D, Q
        COMMON /SIROTCON/ ESI, BS, DS, HS, GS, GDS
        COMMON /SIHYPCON/ B, C, QS
        COMMON /STRENGTH/ Y
        COMMON /LOCAL/ IREP, IVP1, IVS1

        PARAMETER CC = 2.99792458D8

        REAL*8 ESI, EPI, A, AD, AH, BP, DP, HP
        REAL*8 Q0, QD, P0, PD, PH, O0, OD, OH
        REAL*8 BS, DS, HS, GS, GDS, Y, VALUE
        REAL*8 APH, BC, D, Q, CONV, B, C, QS
        REAL*8 Y00, Y10, Y20, Y01, Y11, Y21, Y02, Y12, Y22, Y03
        REAL*8 X00, X10, X20, X01, X11, X21, X02, X12, X22, X03
        REAL*8 A00, A10, A20, A01, A11, A21, A02, G00, G10, G01
        REAL*8 Q00, Q10, Q20, Q01, Q11, Q02, P00, P10, P20, P01, P11, P02
        CHARACTER LABEL*3, V*13, HYP*13

        IFLNOHYP = -1
        ENTRY READCONST2(V,HYP)

        OPEN (10, NAME = 'CMVX15$DUA0:[THANOS.BAI.ARRAYS]CONST'//V,
    X   TYPE='OLD', FORM = 'FORMATTED', READONLY)

        DO 10 I = 1, 20
        READ(10,1050,END=20) LABEL, VALUE
        IF (LABEL.EQ.'ESI') ESI = VALUE
        IF (LABEL.EQ.'EPI') EPI = VALUE
        IF (LABEL.EQ.'A  ') A   = VALUE



        IF (LABEL.EQ.'AD ') AD  = VALUE
        IF (LABEL.EQ.'AH ') AH  = VALUE
        IF (LABEL.EQ.'BP ') BP  = VALUE
        IF (LABEL.EQ.'DP ') DP  = VALUE
        IF (LABEL.EQ.'HP ') HP  = VALUE
        IF (LABEL.EQ.'Q0 ') Q0  = VALUE
        IF (LABEL.EQ.'QD ') QD  = VALUE
        IF (LABEL.EQ.'P0 ') P0  = VALUE
        IF (LABEL.EQ.'PD ') PD  = VALUE
        IF (LABEL.EQ.'PH ') PH  = VALUE
        IF (LABEL.EQ.'BS ') BS  = VALUE
        IF (LABEL.EQ.'DS ') DS  = VALUE
        IF (LABEL.EQ.'HS ') HS  = VALUE
        IF (LABEL.EQ.'GS ') GS  = VALUE
        IF (LABEL.EQ.'GDS') GDS = VALUE
        IF (LABEL.EQ.'O0 ') O0  = (A/BP)*P0/8
        IF (LABEL.EQ.'OD ') OD  = (A/BP)*PD/8
        IF (LABEL.EQ.'OH ') OH  = (A/BP)*PH/8
10      CONTINUE
20      CLOSE (10)
        Y = A / BP

        IF (IFLNOHYP) RETURN

        OPEN (10, NAME = 'CMVX15$DUA0:[THANOS.BAI.ARRAYS]HFS'//HYP,
    X   TYPE='OLD', FORM = 'FORMATTED', READONLY)
        CONV = 10000/CC
        DO 50 I = 1, 10
        READ(10,1050,END=60) LABEL, VALUE
        IF (LABEL.EQ.'APH') APH = VALUE * CONV
        IF (LABEL.EQ.'BC ') BC  = VALUE * CONV
        IF (LABEL.EQ.'D  ') D   = VALUE * CONV
        IF (LABEL.EQ.'Q  ') Q   = VALUE * CONV
        IF (LABEL.EQ.'GS ') GS  = VALUE * CONV
        IF (LABEL.EQ.'B  ') B   = VALUE * CONV
        IF (LABEL.EQ.'C  ') C   = VALUE * CONV
        IF (LABEL.EQ.'QS ') QS  = VALUE * CONV
50      CONTINUE
60      CLOSE(10)

        RETURN

        ENTRY READDUN(IVP,IVS,IFL)

        IF (IREP.NE.0) GOTO 200
        OPEN (10, NAME = 'CMVX15$DUA0:[THANOS.BAI.ARRAYS]DUNHAM',
    X   TYPE='OLD', FORM = 'FORMATTED', READONLY)

        DO 100 I = 1, 50
        READ(10,1050,END=200) LABEL, VALUE

        IF (LABEL.EQ.'Y00') Y00 = VALUE
        IF (LABEL.EQ.'Y10') Y10 = VALUE
        IF (LABEL.EQ.'Y20') Y20 = VALUE
        IF (LABEL.EQ.'A00') A00 = VALUE
        IF (LABEL.EQ.'A10') A10 = VALUE
        IF (LABEL.EQ.'A20') A20 = VALUE
        IF (LABEL.EQ.'A01') A01 = VALUE
        IF (LABEL.EQ.'A11') A11 = VALUE
        IF (LABEL.EQ.'A21') A21 = VALUE
        IF (LABEL.EQ.'A02') A02 = VALUE
        IF (LABEL.EQ.'Y01') Y01 = VALUE
        IF (LABEL.EQ.'Y11') Y11 = VALUE
        IF (LABEL.EQ.'Y21') Y21 = VALUE
        IF (LABEL.EQ.'Y02') Y02 = VALUE
        IF (LABEL.EQ.'Y12') Y12 = VALUE
        IF (LABEL.EQ.'Y22') Y22 = VALUE
        IF (LABEL.EQ.'Y03') Y03 = VALUE
        IF (LABEL.EQ.'Q00') Q00 = VALUE
        IF (LABEL.EQ.'Q10') Q10 = VALUE
        IF (LABEL.EQ.'Q20') Q20 = VALUE
        IF (LABEL.EQ.'Q01') Q01 = VALUE
        IF (LABEL.EQ.'Q11') Q11 = VALUE
        IF (LABEL.EQ.'Q02') Q02 = VALUE
        IF (LABEL.EQ.'P00') P00 = VALUE
        IF (LABEL.EQ.'P10') P10 = VALUE
        IF (LABEL.EQ.'P20') P20 = VALUE
        IF (LABEL.EQ.'P01') P01 = VALUE
        IF (LABEL.EQ.'P11') P11 = VALUE
        IF (LABEL.EQ.'P02') P02 = VALUE
        IF (LABEL.EQ.'X00') X00 = VALUE
        IF (LABEL.EQ.'X10') X10 = VALUE
        IF (LABEL.EQ.'X20') X20 = VALUE
        IF (LABEL.EQ.'X01') X01 = VALUE
        IF (LABEL.EQ.'X11') X11 = VALUE
        IF (LABEL.EQ.'X21') X21 = VALUE
        IF (LABEL.EQ.'X02') X02 = VALUE
        IF (LABEL.EQ.'X12') X12 = VALUE
        IF (LABEL.EQ.'X03') X03 = VALUE
        IF (LABEL.EQ.'G00') G00 = VALUE
        IF (LABEL.EQ.'G10') G10 = VALUE
100     IF (LABEL.EQ.'G01') G01 = VALUE

200     CLOSE(10)
        IREP = 1
        IVP1 = -1
        IVS1 = -1
300     IF (IVP1.EQ.IVP) GOTO 400
        VVP = IVP + .5
        VVP2 = VVP * VVP
        EPI= Y00 + VVP * Y10 + VVP2 * Y20
        A  = A00 + VVP * A10 + VVP2 * A20
        AD = A01 + VVP * A11 + VVP2 * A21
        AH = A02
        BP = Y01 + VVP * Y11 + VVP2 * Y21
        DP=-(Y02 + VVP * Y12 + VVP2 * Y22)
        HP = Y03
        Q0 = Q00 + VVP * Q10 + VVP2 * Q20
        QD = Q01 + VVP * Q11
        P0 = P00 + VVP * P10 + VVP2 * P20
        PD = P01 + VVP * P11
        PH = P02
        Y = A / BP
        IVP1 = IVP

400     IF (IVS1.EQ.IVS) GOTO 500
        VVS = IVS + .5
        VVS2 = VVS * VVS
        ESI= X00 + VVS * X10 + VVS2 * X20
        BS = X01 + VVS * X11 + VVS2 * X21
        DS=-(X02 + VVS * X12)
        HS = X03
        GS = G00 + VVS * G10
        GDS= G01
        IVS1 = IVS

500     IF (IFL.EQ.0) RETURN

        WRITE(9,1100) 'VP ',FLOAT(IVP)
        IF (EPI.NE.0) WRITE(9,1100) 'EPI',EPI
        IF (A  .NE.0) WRITE(9,1100) 'A  ',A
        IF (AD .NE.0) WRITE(9,1100) 'AD ',AD



        IF (AH .NE.0) WRITE(9,1100) 'AH ',AH
        IF (BP .NE.0) WRITE(9,1100) 'BP ',BP
        IF (DP .NE.0) WRITE(9,1100) 'DP ',DP
        IF (HP .NE.0) WRITE(9,1100) 'HP ',HP
        IF (Q0 .NE.0) WRITE(9,1100) 'Q0 ',Q0
        IF (QD .NE.0) WRITE(9,1100) 'QD ',QD
        IF (P0 .NE.0) WRITE(9,1100) 'P0 ',P0
        IF (PD .NE.0) WRITE(9,1100) 'PD ',PD
        IF (PH .NE.0) WRITE(9,1100) 'PH ',PH
        WRITE(9,1100) 'VS ',FLOAT(IVS)
        IF (ESI.NE.0) WRITE(9,1100) 'ESI',ESI
        IF (BS .NE.0) WRITE(9,1100) 'BS ',BS
        IF (DS .NE.0) WRITE(9,1100) 'DS ',DS
        IF (HS .NE.0) WRITE(9,1100) 'HS ',HS
        IF (GS .NE.0) WRITE(9,1100) 'GS ',GS
        IF (GDS.NE.0) WRITE(9,1100) 'GDS',GDS
        CLOSE(9)

1050    FORMAT(A,X,G17.10)
1100    FORMAT(A,'      ',PG17.10)

        RETURN
        END
```

Chapter 5. BaI Product State Distributions

Introduction

The reaction Ba + HI → BaI + H was studied under crossed-beam and beam-gas conditions. Ba was always in a single state ($^1S_0$) and HI in its ground electronic and vibrational state, $X^1\Sigma^+$ v=0. In a crossed-beam experiment [1] only the rotational levels of HI with J equal to 0 and 1 were populated with a ratio 3:1, whereas under beam-gas conditions 92 % of the total population was spread over 9 rotational levels. The internal states of the products were known precisely: BaI ($X^2\Sigma^+$,v,J) and H ($^2S_{1/2}$). In this state-to-state study a handful of reagent states yielded dozens of vibrational levels and hundreds of rotational levels per vibrational level in the BaI products. This segmentation of populations was detrimental to the signal level, but provided the means to observe in great detail the dynamics of this reaction.

The reaction is only slightly exoergic by 7.3 ± 2.0 kcal mol^{-1} [1] and the presence of a possible 2.6 kcal mol^{-1} activation barrier has been suggested [2], but not investigated yet. A limited number of theoretical studies [3, 4] have been performed on this and similar systems. These studies based on classical trajectory calculations did not include any barrier which should primarily arise from spin-uncoupling in both reagent molecules.

Experimental

All the experiments were done with the apparatus described in detail in Chapter 2. In the crossed-beam experiments a neat Ba beam reacted with a supersonic HI beam and the BaI product was probed with phase-sensitive detection of LIF. The raw data included LIF spectra of BaI and Ba and TOF scans for HI. In the beam-gas experiments the same Ba beam reacted with HI gas at room temperature and BaI was probed with photon counting of the SDLIF. Again BaI and Ba spectra constituted the main volume of the data, but transmission spectra of the monochromator were indispensable for the analysis of the data.

All experiments were attempted many times, because very often one of the many components of the apparatus would become unreliable and cast doubt on the validity of the data. In addition, lacking a procedure for the absolute calibration of the reagent beams number densities or for the determination of absolute product yield, all data to be compared had to be accumulated during a single experimental run. This limitation implied that either an run would last for many hours (typically 30 hours) or the data would not be a complete set for analysis.

Crossed-Beam Results

Long range scans of the subbands of the BaI $C^2\Pi$ - $X^2\Sigma^+$ $\Delta v = 0$ sequence under various collision energies provided the first qualitative pictures of the BaI rotational and vibrational distributions. Figure 5.1a shows a typical spectrum originating from a crossed-beam experiment when the average collision energy was 32 kJ mol^{-1}. The features that stand out are 4 pairs of bandheads, an oscillatory pattern to the blue of the bandheads, and three broad peaks to the red. The bandheads are easily assigned to the (v,v) P_1 and Q_{12} branches with v = 0, 1, 2, and 3. These pairs of bandheads are formed at very similar J values in each vibrational band, but as v increases these J values decrease gradually. From the analysis presented in Chapter 4 we know that the bandheads for the (0,0) P_1 and Q_{12} branches are formed at J = 448 and 442, respectively, and for the (3,3) P_1 and Q_{12} branches at J = 435 and 429.

The relative intensities of the pair of bandheads within each band do not reflect the rotational distributions, because their J values are so similar. Rather, the intensities are a consequence of the geometry of the reagent beams and the probe laser polarization. The narrow widths of the velocity distributions of the two beams and their fixed

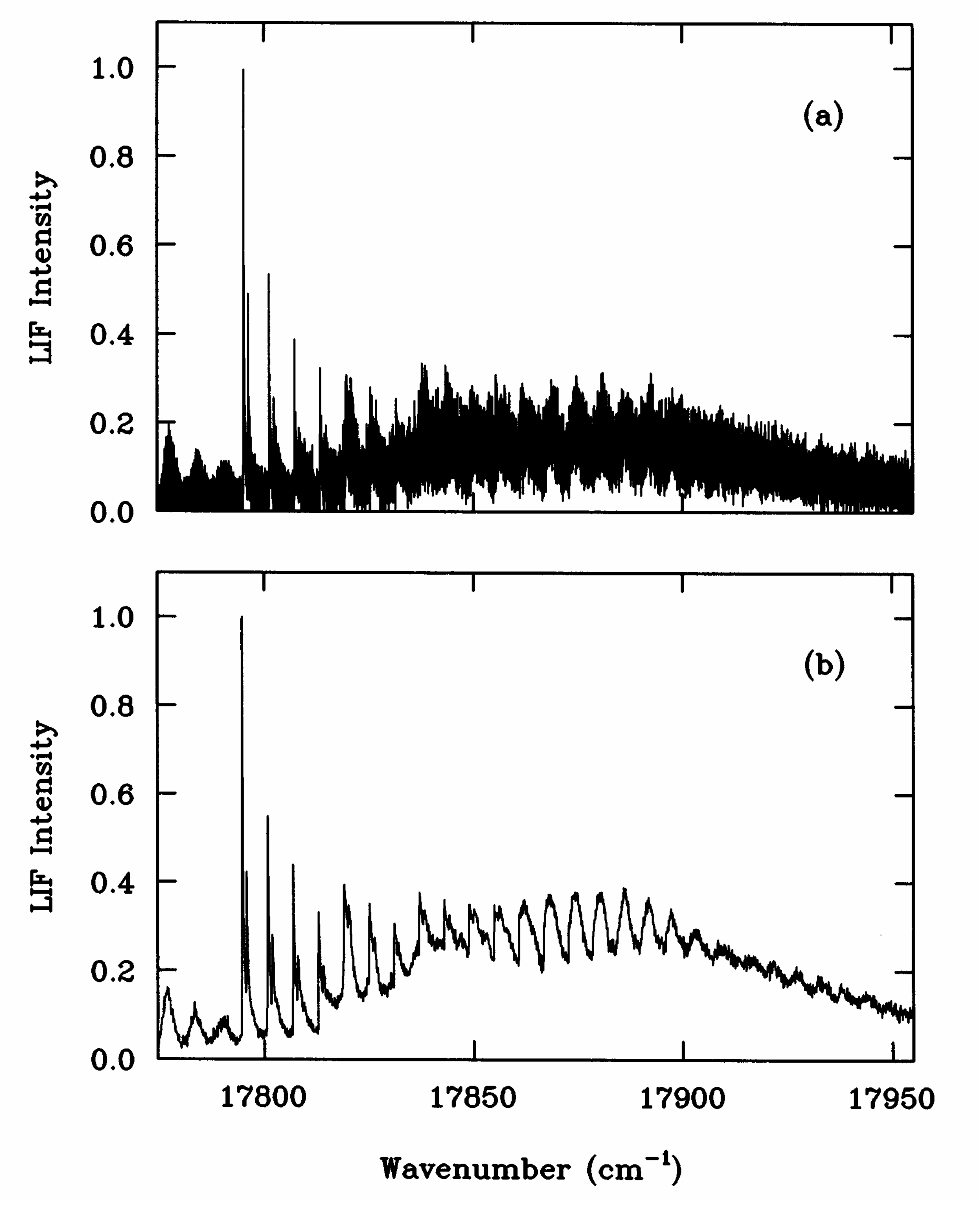

Figure 5.1. (a) LIF spectrum of the BaI $C^2\Pi_{1/2}$ - $X^2\Sigma^+$ $\Delta v=0$ sequence recorded during a crossed-beam study of Ba + HI reaction using a HI/N_2 supersonic beam. (b) The spectrum shown in (a) after gross numerical smoothing.

geometry cause the relative velocity vector, $\mathbf{v}_{rel}$, to point preferentially along the detection axis (see Fig. 2.2). This is also the direction of the laser electric field vector, **E**. Because of the kinematic constraint, $\mathbf{J}_{BaI}$ is always perpendicular to $\mathbf{v}_{rel}$ and $\mathbf{J}_{BaI}$ lies in aplane perpendicular to **E**. BaI $C^2\Pi$ - $X^2\Sigma^+$ is a perpendicular transition and P and R branch members have maximum intensity when **E** is normal to $\mathbf{J}_{BaI}$, whereas Q branch members reach their maximum intensity when **E** is parallel to $\mathbf{J}_{BaI}$ [5].

The "broad" peaks at wavenumbers just below the (0,0) bandheads consist of sequences of resolved rovibronic transitions belonging to the (0,0), (1,1), and (2,2) P_{12} branches. They will be discussed in great detail later. Suffice it for the moment to say that the most intense lines have $J \approx 420$.

The remainder of the spectrum consists of an almost regular sequence of vibrational bands, whose profile becomes more apparent after gross numerical smoothing [6] (see Fig. 5.1b). In view of the extensive overlap of branches belonging to different vibrational bands (see Fortrat diagram in Fig. 4.1b), it is surprising that some features stand out and allow a direct count of vibrational levels. Although not explicitly investigated these features are believed to belong to the "steep" Q_1 and R_{12} branches.

The high energy tail of the vibrational sequence has been exploited to determine a lower bound for the dissociation energy of BaI, $D_0^0(\mathrm{BaI})$, based on energy balance arguments [1]. The value determined was 76.8 ±1.7 kcal mol^{-1}. In light of more recent studies of rotational distributions of many vibrational levels, this lower bound could be raised by as much as 1 kcal mol^{-1}, because approximately that much rotational energy ($J \approx 100$) is found in high ($v \approx 24$) vibrational levels.

The difficulties arising from branch overlaps are also the major factor for rendering the determination of the product vibrational distribution a nearly impossible task. It is far from being clear that the "rise" in the spectrum around $v = 12$ for a crossed-beam experiment is a genuine effect of the relative populations in that region being larger

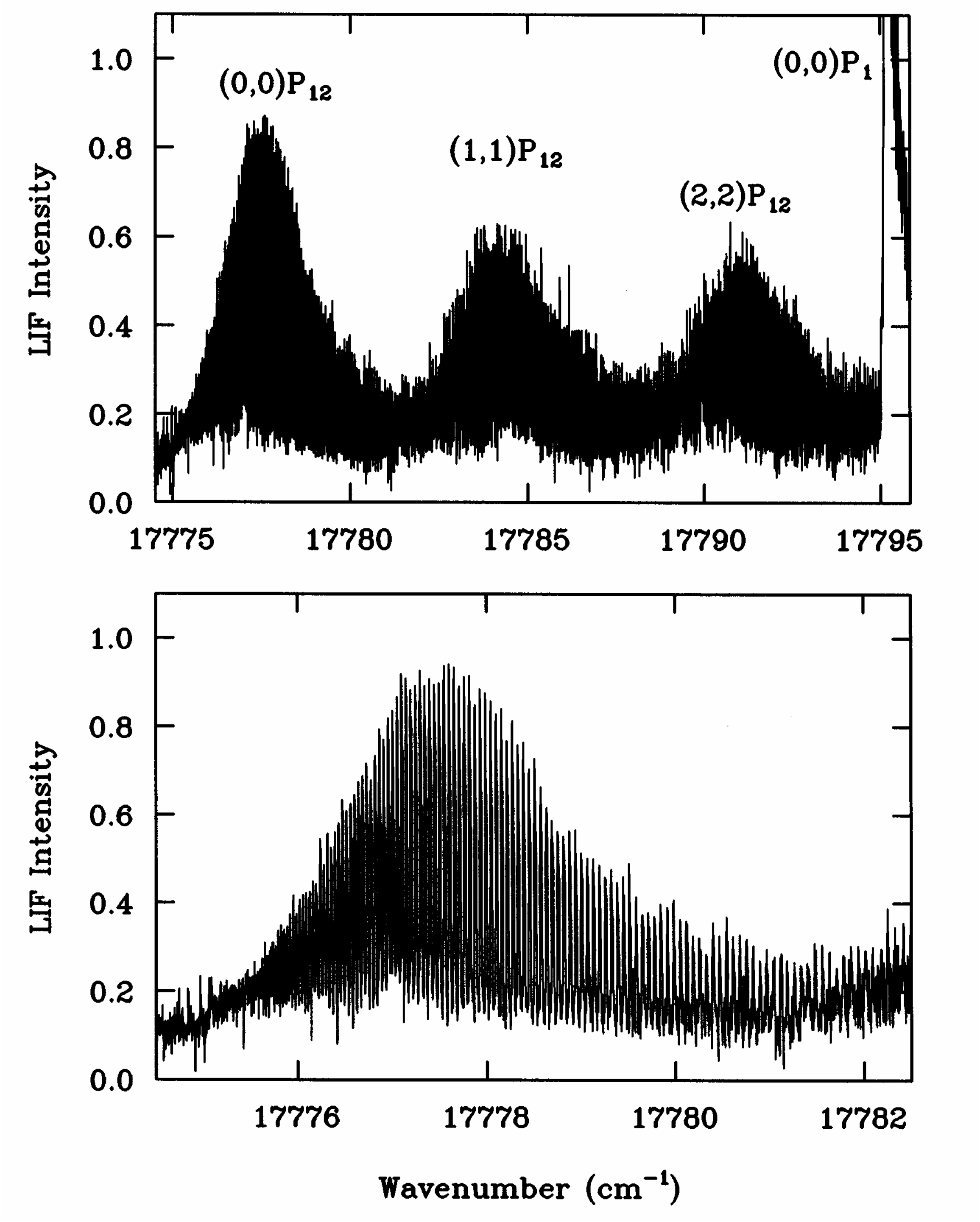

Figure 5.2. (a) LIF spectrum of the BaI $C^2\Pi_{1/2}$ - $X^2\Sigma^+$ (v,v) P_{12} branch members for v = 0, 1, and 2 recorded during a crossed-beam experiment of Ba + HI reaction similar in conditions to the one shown in Fig. 5.1. (b) Expanded view of the low-wavenumber section of the spectrum in (a) displaying the complete, fully-resolved rotational distribution of BaI (v=0).

than that in v = 0. The spectrum in Fig. 5.1a is similar to Fig. 6 of Ref. [1] with the only major difference being the excitation laser power used. We believe that the "rise" in that spectrum is caused by saturation effects. Furthermore, it is interesting to note that theintensity of single rovibronic transitions in the vicinity of 17777 cm^{-1}, which belong to the (0,0) P_{12} branch, is almost the same as the total intensity of all overlapping transitions anywhere in the same spectrum. The only places where the intensity exceeds that of the (0,0) P_{12} branch members are where members of other branches of the (0,0) band are present, viz., the P_1 and Q_{12} bandheads at 17795 cm^{-1}, the Q_1 and R_{12} "steep" branches at 17820 cm^{-1}, and the R_1 branch members at 17838 cm^{-1}.

Figure 5.2a shows an expanded view of the lower wavenumber region of Fig. 5.1. Well resolved rovibronic transitions of the (0,0), (1,1), and (2,2) P_{12} branches can be seen. The spread of all three rotational distributions is comparable, but their intensities decrease as the vibrational quantum number increases. This trend shows that the vibrational distribution of BaI is anything but inverted under crossed-beam conditions.

Figure 5.3a shows a long range scan of the $C^2\Pi_{3/2}$ - $X^2\Sigma^+$ $\Delta v=0$ sequence recorded during a crossed-beam experiment conducted with a faster HI beam. The translational energy of the reagent was estimated to be 51 kJ mol^{-1}. Some striking differences from the "slower" experiment are worth pointing out. Most notably, P_2 bandheads appear indicating that rotational levels are formed with J values as high as 508. This is not surprising since more energy is available to the system. The same argument also explains why more vibrational levels are observed to be populated. In this case it is hard to decide if the rise in the middle of the spectrum reflects a higher vibrational population or not. Without information on rotational distributions for the different vibrational levels we can only speculate how the peaks of the rotational distributions change with v. The fact that the P_{21} bandheads grow in intensity as v increases could simply reflect the fact that the peaks of the rotational distributions are

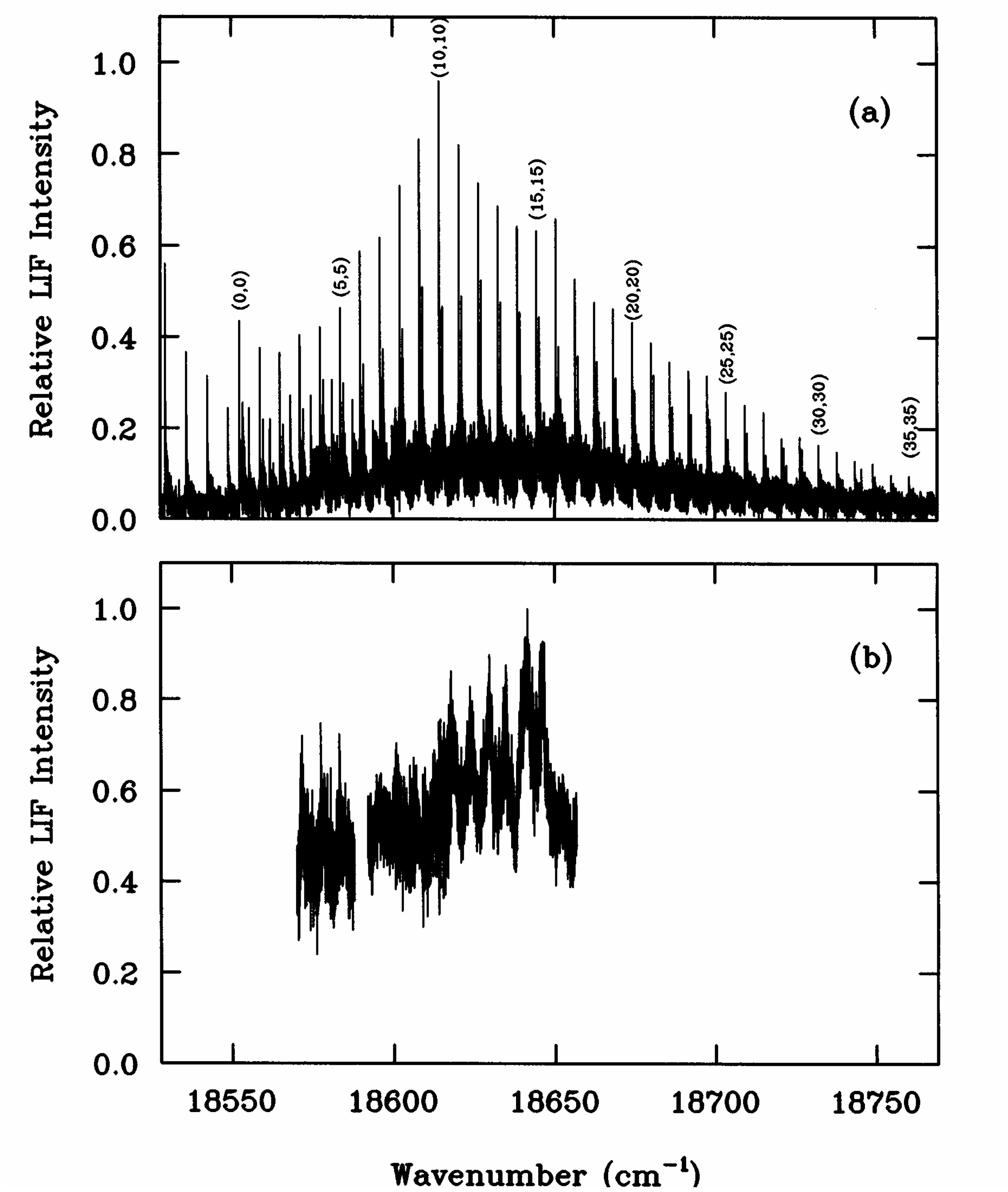

Figure 5.3. (a) LIF spectrum of the BaI $C^2\Pi_{1/2}$ - $X^2\Sigma^+$ $\Delta v=0$ sequence recorded during a crossed-beam study of Ba + HI reaction using a HI/He supersonic beam. The vibrational assignment of selected P_{21} and Q_2 bandheads is indicated. (b) LIF spectrum of the BaI $C^2\Pi_{1/2}$ - $X^2\Sigma^+$ $\Delta v=0$ sequence recorded during a crossed-beam study of Ba + HI reaction using a HI/Ar/N_2 supersonic beam. Numerical smoothing has been performed on the data to reveal the main structure.

moving from values around 500 for v=0 to lower J values that correspond to the P_{21} bandheads, i.e., J=400 for v=11.

Figure 5.3b shows a portion of a similar scan recorded under considerably lower collision energies. The average collision energy was 22 kJ mol $^{-1}$. In this case signal level was very low and caused the scan to remain fragmented and incomplete. As expected from energy balance none of the bandheads are formed. Again we observed an oscillatory pattern, but it is unclear from this scan which band is most intense.

Of prime importance to our efforts to determine specific opacity functions was the extraction of rotational distributions for different vibrational levels under varying collision energies. Figure 5.2 shows the region of the spectrum that was used for the extraction of the rotational populations. Under carefully chosen conditions the highest populated rotational levels were below those that give rise to the P_{12} (or P_2) bandheads. Bandheads require spectral simulations for the determination of rotational state distributions and were avoided in our studies. As seen from the Fortrat diagram in Fig. 4.1b, no branches overlap in the region approximately 6 cm^{-1} to the blue of the (0,0) P_{12} or P_2 bandhead, and rovibronic transitions in this "isolated" region are fully resolved.

As seen in Fig 5.2b, the BaI (v=0) rotational distribution does not extend past this 6-cm^{-1} interval [7]. This fact provided a first indication of the rotational distribution and allowed the measurement of the distributions of the next highest vibrational levels.

Rotational populations are extracted from the assigned spectra by measuring the heights of the rotational lines from a constant baseline. This baseline was determined from the region of the spectrum with wavenumbers lower than that of the bandhead, where it is known that there are no P_{12} or P_2 branch members. No digital smoothing was performed on the spectra, because it did not improve the smoothness of the rotational distributions nor did it affect the subsequent calculations of the opacity function. Measurement of the heights was preferred over integration of line profiles because of the uncertainty in those profiles. Although hyperfine splittings and Doppler broadening are well understood phenomena, there is a host of underlying transitions even in this "isolated" region of the C - X spectrum. Contributions from the high-v region of the $\Delta v=-1$ sequence are not expected to yield strong signals with sharp features and were suppressed with the use of low excitation power. The presence of lines arising from isotopomers (see Chapter 4) other than the most abundant ^{138}BaI added an inescapable systematic source of error in our measurements of the line intensities used to determine the rotational populations. Any attempt to simulate these contributions was hindered by the complete lack of information about the hyperfine structure of the transitions of the odd-mass isotopomers that carry nonzero nuclear spin on Ba.

Rotational distributions were recorded for BaI (v=0, 1, 2) under a range of relative velocity distributions [8]. The results are shown in Figs. 5.4-5.6 and summarized in Table 5.1. In all experiments the width of the relative velocity distribution was approximately the same. The energy spread of the rotational distributions only slightly exceeded the collision energy width. When the rotational distributions of different vibrational levels are compared it becomes apparent that the peak of the distribution moves to lower rotational states, but the reduction in average rotational energy is greater than the increase in vibrational energy. Two explanations have been proposed for this behavior: (1) the product recoil energy is higher for higher product vibrational levels; and (2) the reaction probability is a function of the relative velocity and different sections of the relative velocity distribution give product in different vibrational levels.

Beam-Gas Results

The study of the reaction under beam-gas conditions has an advantage over the crossed-beam experiments which is also its major drawback. The reaction can be studied under a wide range of collision energies simultaneously, but the contributions of each of these different collision energies to the product formation cannot be separated from each

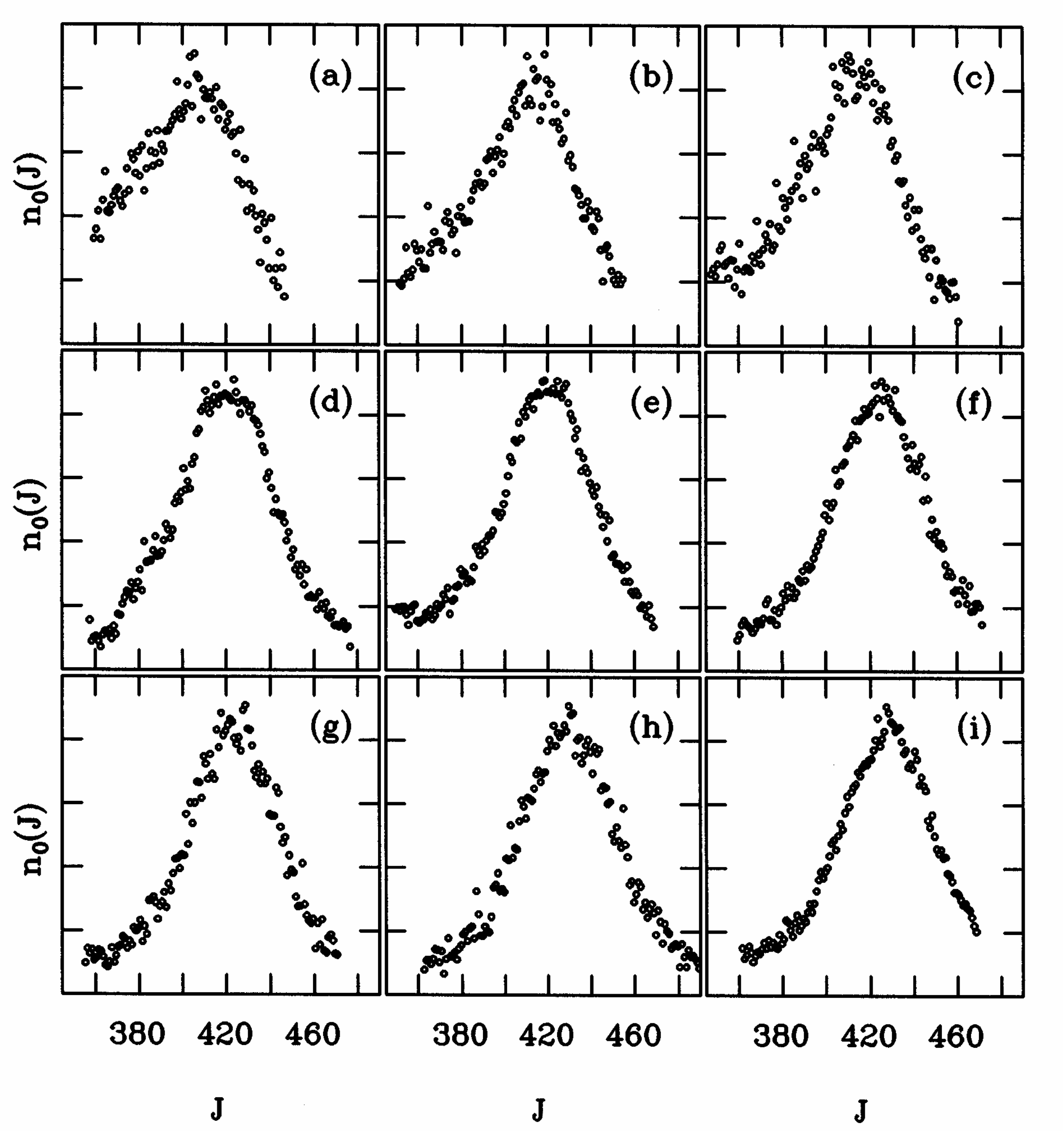

Figure 5.4. Rotational distributions of BaI (v=0) recorded during crossed-beam experiments of the Ba + HI reaction under varying relative velocity distributions. The data are shown in order of increasing mean relative velocity. The labels refer to the experimental conditions listed in Tables 3.1 and 5.1.

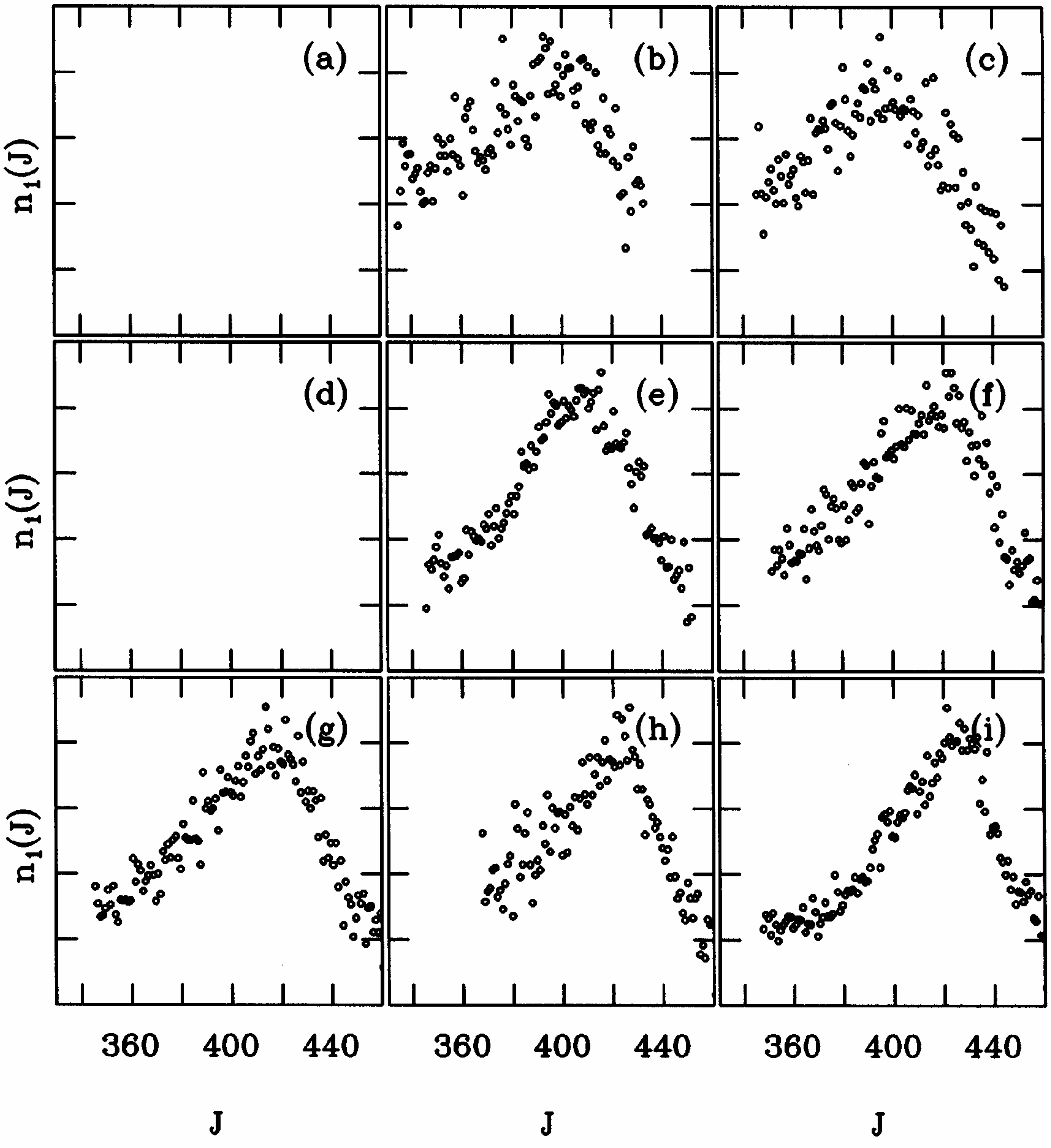

Figure 5.5. Rotational distributions of BaI (v=1) recorded during crossed-beam experiments of the Ba + HI reaction under varying relative velocity distributions. The data are shown in order of increasing mean relative velocity.

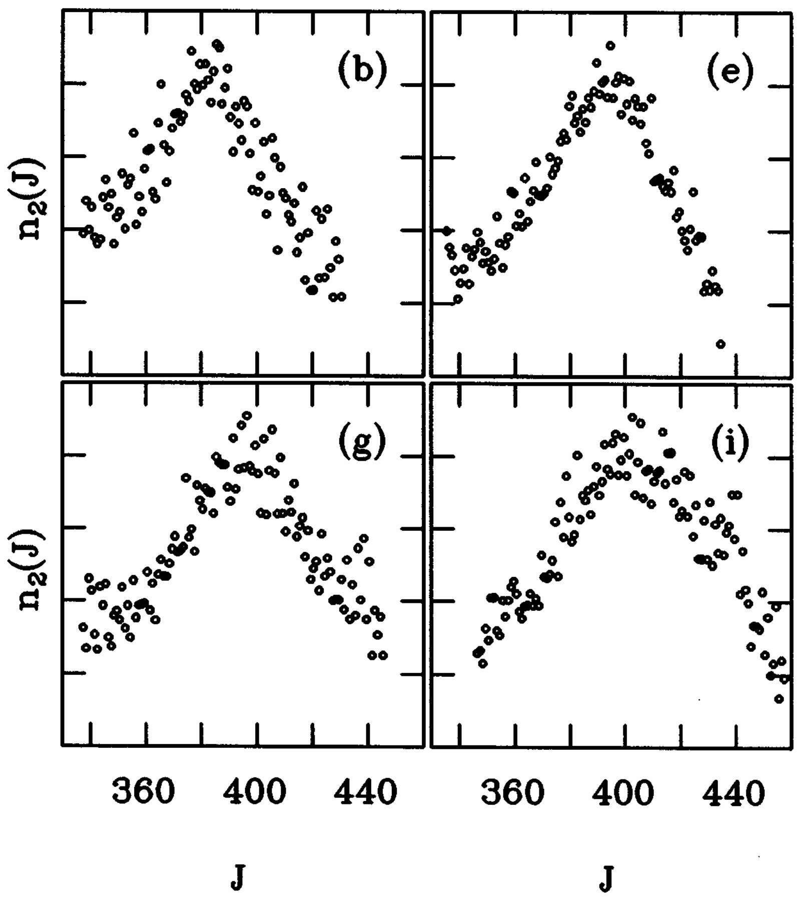

Figure 5.6. Rotational distributions of BaI (v=2) recorded during crossed-beam experiments of the Ba + HI reaction under varying relative velocity distributions. The data are shown in order of increasing mean relative velocity.

other. Crossed-beam experiments usually involve higher average collision energies than beam-gas experiments. Yet under our typical beam-gas conditions we observed BaI(v=0) in rotational levels higher than those observed during our typical crossed-beam experiment!

The beam-gas experiments presented below were initially aiming at conducting preliminary spectroscopic investigations of bands that had not been studied before. Later, these experiments were considered as a feasibility test for the SDLIF detection scheme

Table 5.1. Rotational distribution moments for crossed-beam experiments as a function of relative velocity and collision energy conditions. Units used are m s^{-1} and kJ mol^{-1}. Experiments are listed in order of increasing values of mean relative velocity.

Label	Relative Velocity		Collision Energy		v = 0		v = 1		v = 2	
	v_{mean}	FWHM	E_{mean}	FWHM	J_{mp}	FWHM	J_{mp}	FWHM	J_{mp}	FWHM
a[1]	875	234	25.7	14.2	405.5	52				
b	915	230	28.1	14.6	410.5	59	392.5	62	385.5	56
c	919	227	28.3	14.4	410.5	62	395.5	60		
d	959	217	30.7	14.3	415.5	59				
e	961	210	30.8	13.8	418.5	63	415.5	61	394.5	58
f	965	208	31.1	13.7	425.5	58	423.5	64		
g	996	191	33.1	12.9	428.5	58	413.5	67	396.5	65
h	976	217	31.8	14.5	429.5	61	426.5	55		
i	1035	200	35.7	14.1	427.5	57	421.5	65	402.5	65

[1] Experiment labels used in Figs. 5.4, 5.5, 5.6, 6.3, 6.4, and 6.5.

under crossed-beam conditions. Both means proved to be interesting ends in themselves as our understanding of the BaI spectroscopy as well as that of the Ba + HI reaction dynamics were greatly expanded.

Figure 5.7a shows a long-range scan of the BaI $C^2\Pi_{3/2}$ - $X^2\Sigma^+$ $\Delta v=0$ sequence recorded under beam-gas conditions [9]. Most of the "noise" is real, but mostly unresolved structure. Some of the "noise" can be identified as I_2 transitions. I_2 is a contaminant in the reaction chamber generated by the decomposition of HI on the hot walls of the Ba source chamber. Not much can be said about the rotational distributions because very little structure is resolved. Some low-v bandheads are seen indicating high rotational excitation. The vibrational distribution becomes apparent in Fig. 5.7b which shows the same spectrum after gross numerical smoothing. Vibrational levels with v between 0 and 30 were populated with a peak in the distribution near v=12. Although a systematic comparison of yields in different vibrational levels has not been completed, studies of the BaI (v) rotational distributions with v=4, 8, 12, and 16 showed that the v=12 level has undoubtedly more population.

Using SDLIF we were able to record rotational distributions for BaI (v) with v=0, 4, 8, 12, and 16 and collect preliminary data for v between 18 and 24 [10]. The principle of the SDLIF scheme has been described in Chapter 4. Here we emphasize on the extraction of population information from the spectra. First, we need to know the transmission spectrum of the "detection window" which is a window in wavenumber space. This spectrum was recorded with the use of scattered laser light (see Chapter 2). To facilitate numerical manipulations of the information derived from the BaI spectra and to simulate these spectra, the transmission spectrum was fit by a simple empirical function of the form:

$$T(\sigma) = T_0 \, (\sigma - p_1)^3 \, \exp\left[-\left(\frac{\sigma - p_2}{p_3} \right)^2 \right] \tag{5.1}$$

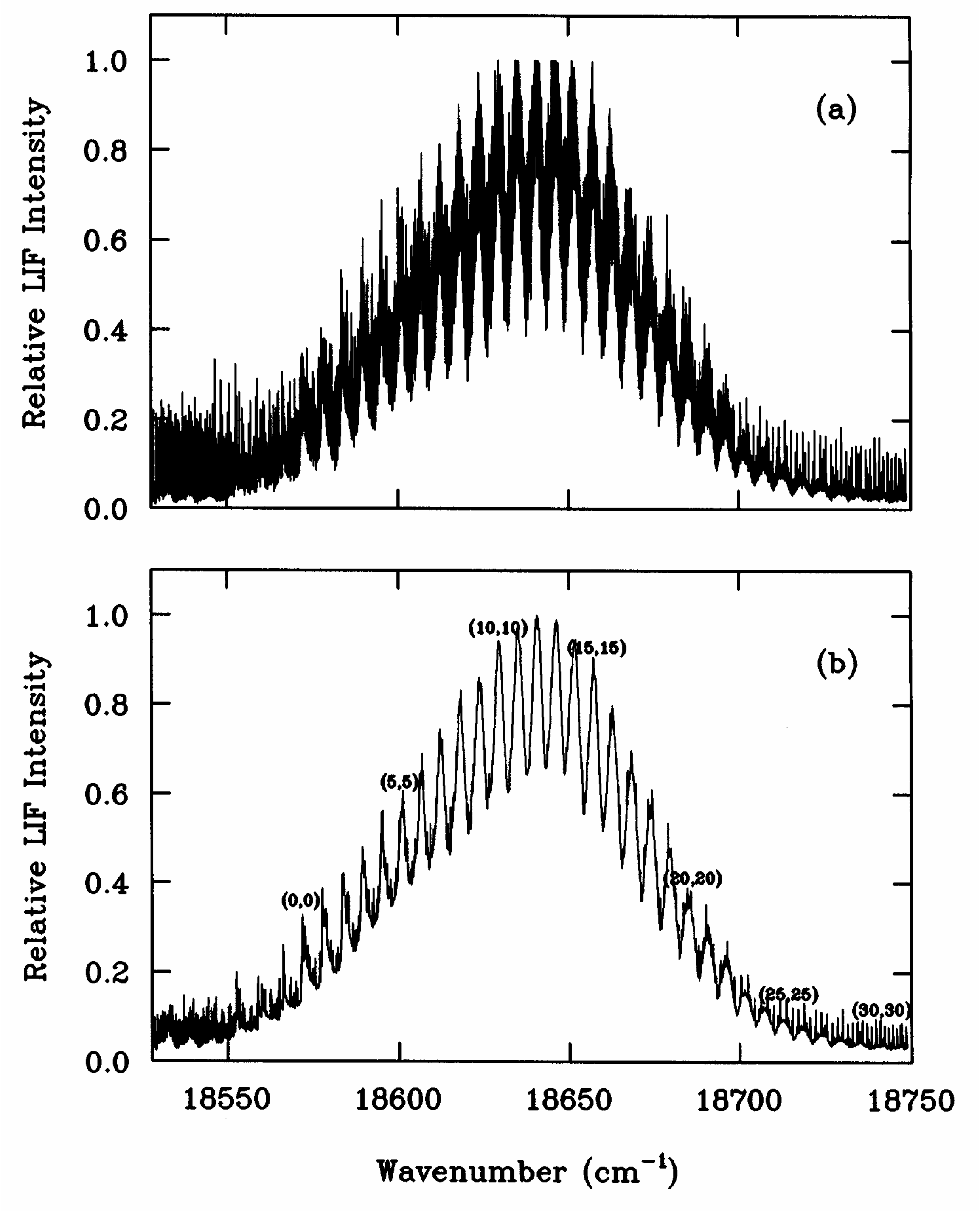

Figure 5.7. (a) LIF spectrum of the BaI $C^2\Pi_{3/2}$ - $X^2\Sigma^+$ $\Delta v=0$ sequence recorded during a beam-gas experiment of Ba + HI reaction. (b) The spectrum shown in (a) after gross numerical smoothing. Vibrational bands are labeled at the "steep" sections of the Q_{21} and R_2 branches.

defined only for $\sigma > p_1$, where $T(\sigma)$ is the transmission probability at wavenumber σ and T_0, p_1, p_2 and p_3 are adjustable parameter. A typical transmission spectrum and the associated fit are shown in Fig. 5.8.

If F(J',J") is the wavenumber of a certain rovibronic transition, S(J',J") is its line strength, and $n_v(J")$ is the population of the BaI ($^2\Sigma^+$,v,J") level being probed, then the fluorescence transmitted through the monochromator is

$$I(J") = n_v(J")\ S(J',J")\ \sum_{m=-1}^{1} S(J',J'-m)\ T\big[F(J',J'-m)\big] \qquad (5.2)$$

The sum includes the transmission probability of all possible three emission paths (P, Q, R branches). Our spectra consist of a superposition of signals corresponding to members of all branches or bands that exist near F(J',J"). The position and the width of the transmission spectrum were chosen in such a way that members of only one branch would contribute to the SDLIF spectrum. In this case measurement of the transmitted intensities could be readily converted to rotational populations.

This approach was fruitful for large sections of the spectra. Unfortunately, as mentioned in Chapter 4, co-observation of "crossing" branches could not be avoided. The interference usually manifested itself as a drastic change in the baseline. Our analysis of the spectra determined the line intensities of interest from the heights of those lines measured above the local baseline. Light numerical smoothing of the recorded spectra prior to the determination of the line intensities helped remove random noise.

These spectra were recorded using laser power of the order of 15 mW and biasing the PMT with 1500 V. The photon count rates were of the order of at most a few thousands events per second. Sources of photon noise were the Ba oven because of its high temperature and occasionally I_2 transitions; the latter could confirmed easily by direct comparison with the I_2 spectrum recorded concurrently (see Chapter 2). The

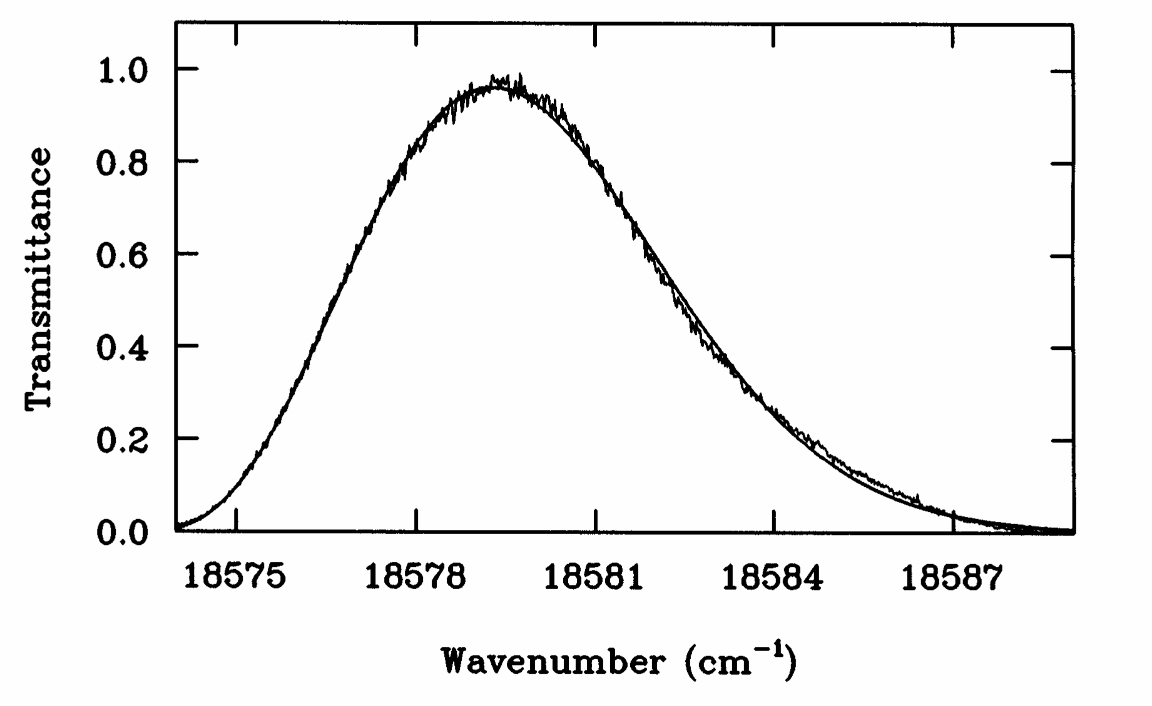

Figure 5.8. Monochromator transmission spectrum and associated fit. The fitting parameters (and related uncertainties) were $p_1 = 18573.39$ (2) cm^{-1}, $p_2 = 18571.07$ (1) cm^{-1}, and $p_3 = 4.02$ (2) cm^{-1}. The transmission maximum was 18579.29 cm^{-1} and the FWHM of the spectrum was 6.03 cm^{-1}.

origins of electronic noise we never identified, but the noise was only transient and its effect could usually be rectified through numerical smoothing.

The preferred scheme in these experiments involved excitation of BaI molecules via R_{21} branch members and detection of fluorescence arising from transitions in the P_{12} and Q_2 branches. The width of the monochromator transmission spectra could not encompass the whole range of wavenumbers where molecules from one vibrational level could fluoresce. Multiple scans were needed with corresponding transmission spectra overlapping extensively. A section of a rotational distribution could be determined from each scan and a weighted average of these sections gave the complete distribution in a particular vibrational level.

Rotational population distributions measured for BaI (v) with v=0, 4, 8, 12, 16, and 18 are shown in Fig 5.9 and summarized in Table 5.2. The experimental conditions were similar (Ba beam velocities, HI pressure, excitation laser power) and only one distribution for each vibrational level was used in any subsequent analysis. No error bars are shown in Fig. 5.9, but the scatter of the population of successive rotational states is indicative of the associated uncertainties. The regions of highest uncertainty are usually near J = 110, 220, and 350 where interference from the "crossing" branches occurs.

Certain clear trends can be deduced from the available data. The rotational distributions become narrower and their peaks move toward the middle of the populated ranges as the vibrational quantum number increases. As in the case of the crossed-beam results, the increase in vibrational energy does not match the decrease in the average rotational energy. Both explanations offered above could account for the observed effect. It is also interesting to note that the rotational distributions for v≥18 are very similar in shape and no significant variation in the peak position can be established. The low rotational energies involved and low correlation between impact parameters and product rotation could explain this effect.

Our results for BaI (v=8) do not agree very closely with the earlier beam-gas work [11]. The origins of this discrepancy can be traced to differences in the way the experiments were done and in the way the data were processed which arise from improved understanding of the spectroscopy. Noda et al. [11] scanned over the P_{12} branch, used considerably higher laser power which broadened the line profiles and increased overlaps, implemented a less refined measurement of the Ba beam velocity distribution, and relied on a limited number of measurements of the monochromator transmission spectrum. In addition, subsequent spectroscopic studies (presented in

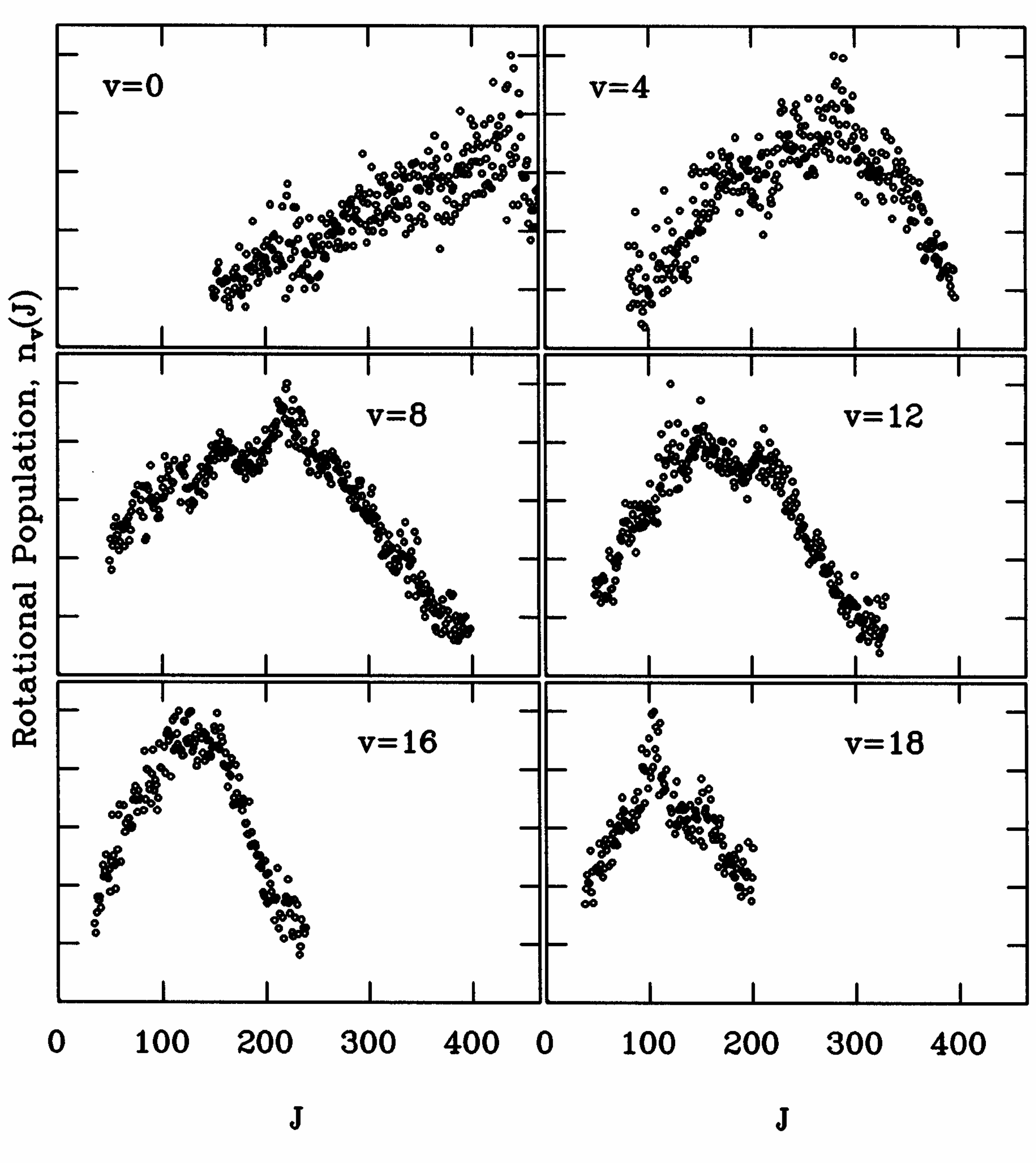

Figure 5.9. BaI (v) rotational state distributions for v = 0, 4, 8, 12, 16, and 18 recorded during beam gas experiments.

Chapter 4) have improved our knowledge of the position of the branches used to collect the fluorescence and the ones that interfere with the observation.

The most surprising result was the BaI (v=0) rotational distribution. This distribution seemingly defies the principle of energy conservation. The average available energy (translational and internal energy of reagents and exoergicity of the reaction) does not amount to the rotational energy of the most populated rotational level in the products. This unexpected result is most impressive when compared to a crossed-beam distribution (see Fig. 5.10). The immediate conclusion is that the relative velocity distribution in a beam-gas experiment is only in part reactive to produce BaI (v=0). The possible causes of this behavior will be discussed in the next chapter. Since the relative velocity varies slowly with velocity in the range where the whole crossed-beam distribution lies, the reactive section of $f(v_{rel})$ in the beam-gas experiment is flatter and extends to very high velocities. This explains why even levels with J=510 have been observed (they form the (0,0) P_2 bandhead), which did not happen in medium fast crossed-beam experiments.

In conclusion, the study of the Ba + HI reaction has provided information on the rotational distributions in many product vibrational levels. These results have been a challenge to obtain and an even greater challenge to interpret.

Table 5.2. BaI(v) rotational population distribution moments measured under beam-gas conditions. Total internal BaI energy is given in kJ mol^{-1}.

v	J_{mp}	J_{mean}	FWHM	E_{mean}	FWHM
0	438.5	341	206	40	42
4	280.5	249	182	30	25
8	220.5	208	200	31	27
12	144.5	181	160	33	18
16	115.5	130	114	35	9.5
18	104.5	118	102	37	7.6

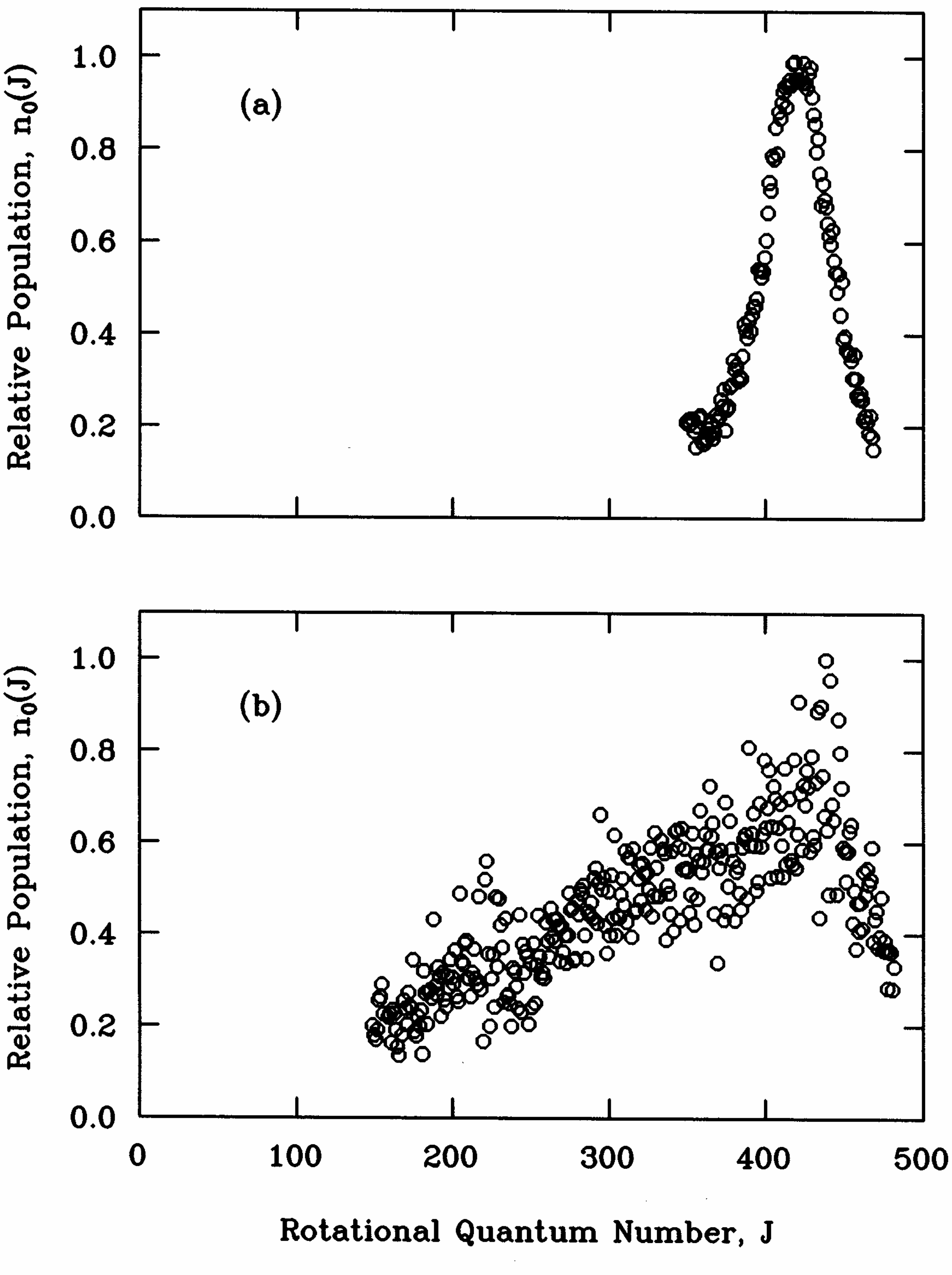

Figure 5.10. BaI (v=0) rotational distributions obtained under (a) crossed-beam and (b) beam-gas conditions.

References

1 P. H. Vaccaro, D. Zhao, A. A. Tsekouras, C. A. Leach, W. E. Ernst, and R. N. Zare, *J. Chem. Phys.* 93, 8544 (1990).

2 C. A. Mims, S.-M. Lin, and R. R. Herm, *J. Chem. Phys.* **57**, 3099 (1972).

3 A. Siegel and A. Schultz, *J. Chem. Phys.* **76**, 4513(1982).

4 D. Zhao and R. N. Zare, in preparation.

5 R. N. Zare, "Angular Momentum: Understanding Spatial Aspects in Chemistry and Physics," Wiley, New York, 1988.

6 P. Marchant and L. Marmet, *Rev. Sci. Intrum.* **54**, 1034 (1983).

7 C. A. Leach, A. A. Tsekouras, P. H. Vaccaro, R. N. Zare, and D. Zhao, *Faraday Discuss. Chem. Soc.*, **91**, 183 (1991).

8 P. H. Vaccaro, A. A. Tsekouras, D. Zhao, C. A. Leach, and R. N. Zare, *J. Chem. Phys.* **96**, 2786 (1992).

9 P. H. Vaccaro, A. A. Tsekouras, D. Zhao, and R. N. Zare, (unpublished results).

10 A. A. Tsekouras, C. A. Leach, K. S. Kalogerakis, and R. N. Zare, (in preparation).

11 C. Noda, J. S. McKillop, M. A. Johnson, J. R. Waldeck, and R. N. Zare, *J. Chem. Phys.* **85**, 856 (1986).

Chapter 6. Specific Opacity Functions

Introduction

In the preceding chapters we discussed how we carried out experiments on the Ba + HI reaction and what reactive data we collected. We are now going to combine all the available information in order to determine the specific reactive opacity functions for the formation of BaI in the vibrational levels studied. We will discuss crossed-beam data separately from beam-gas data because the energies involved and the spreads of the rotational distributions are so different. Finally, we will try to create a unified picture on how the reaction proceeds.

Definitions

The reaction

$$\mathrm{Ba + HI \rightarrow BaI + H} \qquad (6.1)$$

was chosen for this study because of its unique kinematic constraint [1], i.e., its extreme value for the ratio of the reduced masses before and after the reaction, which is

$$\mu(\mathrm{Ba\text{-}HI}) : \mu(\mathrm{BaI\text{-}H}) = 66 : 1. \qquad (6.2)$$

Another property of this reaction that makes it appropriate [2] for our study is its low exoergicity, $\Delta E \approx 7.5$ kcal mol^{-1} [3].

In the gas phase and at low pressures each colliding pair of reagents is an isolated system for which the conservation principles of energy and angular momentum can be applied readily to help interpret the experimental results. Energy conservation has been discussed in the previous chapter and now we will focus on angular momentum.

Each particle involved in the reaction has angular momentum, $\mathbf{J}$, arising from its rotation and from electronic motion and spin. In all cases reactions were done with Ba in its ground electronic state which has $J_{\mathrm{Ba}} = 0$. HI has angular momentum because of its rotation alone. In the crossed-beam work, 76 % of the HI molecules was in the ground rotational level and the remaining 24% was in the $J_{HI} = 1$ level; in the beam-gas experiments 92 % of the molecules was in rotational levels with $J \leq 8$. BaI was found to be highly rotationally excited, but H can only have exactly $J_H = {}^1/_2$ (or $F_H = 0$ or 1, if we include nuclear angular momenta too). [In general, we are going to ignore the nuclear spins assuming that they act as spectators during the reaction [4].] Approaching reagents or recoiling products possess orbital angular momentum, **L**, because of their relative motion. Its magnitude is given by the following equation.

$$|\mathbf{L}| = \mu\, v_{rel}\, b \tag{6.3}$$

where μ and v_{rel} are the reduced mass and the relative velocity of the two particles and b is the impact parameter of the collision. The impact parameter is defined as the distance of closest approach in the hypothetical absence of any interaction between the particles. Because of the large difference in reduced masses the relative motion of the reagents carries orders of magnitude more orbital angular momentum than the products.

The general equation for the conservation of angular momentum, viz.,

$$\mathbf{L}_{reag} + \mathbf{J}_{reag} = \mathbf{L}_{prod} + \mathbf{J}_{prod} \tag{6.4}$$

reduces to

$$\mathbf{L}_{reag} = \mathbf{J}_{BaI} \tag{6.5}$$

or[1]

$$\mu_{Ba\text{-}HI}\, v_{rel(Ba\text{-}HI)}\, b_{Ba\text{-}HI} = \hbar\, J_{BaI} \tag{6.6}$$

The quantities omitted in Eq. 6.5 are vector quantities. Their projections on the axis of the leading terms should average to 0. If the small angular momenta are not strongly correlated, the omission of the small terms has the effect of increasing the

---

[1] Strictly, $|\mathbf{J}_{BaI}| = \hbar\sqrt{J_{BaI}(J_{BaI}+1)}$ because $\mathcal{J}^2\, |J_{BaI}\rangle = \hbar\, J_{BaI}(J_{BaI}+1)$, but for notational brevity we will write $|\mathbf{J}_{BaI}| = \hbar\, J_{BaI}$.

uncertainties of the terms remaining in Eq. 6.5.

Equation 6.6 is key to elucidating the nature of the impact parameter. Given the measured distributions for both the reagent relative velocity and the product rotational levels, in principle, Equation 6.6 should be solved for b to provide the answer. This process could be followed only if the experiment were to be performed under an extremely narrow relative velocity distribution. As the relative velocity distribution spreads, a wider range of collision conditions is sampled, but at the same time the results become less well defined as more averaging over initial conditions is performed.

The experimental results have been the relative velocity distribution, $f(v_{rel})$, and the product rotational population distribution, $n_v(J)$, in a specific vibrational level v. We need to determine the reaction probability, $P_v(b)$, as a function of impact parameter averaged over all collision orientations and velocities, which is called the specific opacity function. Summed over all vibrational levels and averaged over all reactive impact parameter values, the specific opacity functions yield the total reaction cross section, σ [5],

$$\sigma = \int_0^\infty P(b)\ 2\pi b\ \ db \tag{6.7}$$

where

$$P(b) = \sum_v P_v(b) \tag{6.8}$$

which is related to the reaction rate constant through Eq. 6.9.

$$k = v_{rel}\, \sigma \tag{6.9}$$

The rate of product formation is

$$\frac{dn}{dt} = k\ \ n_{Ba}\ \ n_{HI} \tag{6.10}$$

where n_{Ba} and n_{HI} are the number densities of the reagents in the interaction region, and the rate of product removal is

$$\frac{dn}{dt} = -v'\ \ S\ \ n \tag{6.11}$$

where v' is the (average) laboratory-frame velocity of BaI, S is the area through which

BaI leaves the observation region (detection volume), and n is the product number density which is determined experimentally.

In the steady state approximation Eqs. 6.10 and 6.11 yield

$$n = \frac{k\ n_{Ba}\ n_{HI}}{v'\ S} \tag{6.12}$$

After substituting Eqs. 6.6-6.9 in Eq. 6.12 we get

$$n = n_{Ba}\ n_{HI}\ \frac{v_{rel}}{v'\ S}\int_0^{\infty} P(b)\ 2\pi b\ db \tag{6.13}$$

For product formed in a specific vibrational level, Eq. 6.13 becomes

$$n_v = n_{Ba}\ n_{HI}\ \frac{v_{rel}}{v'\ S}\int_0^{\infty} P_v(b)\ 2\pi b\ db \tag{6.14}$$

If we consider product formed under any collision velocity, Eq. 6.14 yields

$$n_v = \frac{n_{Ba}\ n_{HI}}{v'\ S}\int_0^{\infty}\int_0^{\infty} P_v(b)\ 2\pi b\ db\ v_{rel}\ f(v_{rel})\ dv_{rel} \tag{6.15}$$

and for a specific product rotational level

$$n_v(J) = \frac{n_{Ba}\ n_{HI}}{v'\ S}\int_0^{\infty}\int_0^{\infty} P_v(b)\ 2\pi b\ \delta(|\mathbf{J}| - |\mathbf{L}|)\ db\ v_{rel}\ f(v_{rel})\ dv_{rel} \tag{6.16}$$

where

$$|\mathbf{L}| = \mu\ v_{rel}\ b \tag{6.17}$$

J_{BaI} has been abbreviated to J, and μ, v_{rel}, and b refer to the reagents.

The product velocity, v', has been left out of the integrals because it is assumed to vary independently of the relative velocity. v' is very nearly equal to the velocity of the center of mass of the system [2]. We replace the factor in front of the integral by a constant which is different for each experiment.

Eq. 6.16 can be simplified by the elimination of the double integral and the δ function.

$$n_v(J) = A\int_0^{\infty} P_v(b)\ 2\pi b\ \frac{\partial b}{\partial J}\ v_{rel}\ f(v_{rel})\ dv_{rel} \tag{6.18}$$

where

$$b = \frac{\hbar\ J}{\mu\ v_{rel}} \tag{6.19}$$

and consequently

$$\frac{\partial b}{\partial J} = \frac{\hbar}{\mu \ v_{rel}} \qquad (6.20)$$

and thus the rotational population of BaI (v,J) is given by

$$n_v(J) = A \int_0^\infty P_v(b) \ b \ f(v_{rel}) \ dv_{rel} \qquad (6.21)$$

where all the constants have been incorporated into A.

We have derived Eq. 6.21 based on the definitions and on the conservation of angular momentum as it applies to the Ba + HI reaction. We will use Eq. 6.21 below as we try different models (functional forms) for the specific opacity functions.

The Energetic Limit

All studied phenomena are known to follow the principle of energy conservation. The BaI product was found to have very high internal excitation suggesting an almost complete conversion of the available energy in observable rotational and vibrational motion. Conservation of energy and the kinematic constraint allow us to derive an expression relating the final product state of BaI with a minimum value for the relative velocity [6]; velocities below this limiting value cannot form product in that state of BaI independent of impact parameter.

From energy conservation:

$$E_{rel\ (Ba\text{-}HI)} + \Delta E = E_{int(BaI)} + E_{rec\ (BaI\text{-}H)} \qquad (6.22)$$

where E_{rel} is the collision energy, ΔE is the exoergicity of the reaction, E_{int} is the rotational and vibrational energy of BaI measured above the (v=0,J=0) level, and E_{rec} is the recoil energy of the products. By dropping E_{rec} from Eq. 6.22, we get

$$E_{rel\ (Ba\text{-}HI)} + \Delta E \geq E_{int(BaI)} \qquad (6.23)$$

E_{rel} is a function of v_{rel}, E_{rot} is a function of J, and both are related via Eq. 6.6. Inequality 6.23 can be solved in many different ways depending on which variable is eliminated among the set of J, v_{rel}, and b, viz.,

$$b \leq b_{max}(v_{rel}) \qquad (6.24a)$$

$$b \le b_{max}(J) \tag{6.24b}$$

$$v_{rel} \le v_{max}(b) \tag{6.24c}$$

$$v_{rel} \ge v_{min}(J) \tag{6.24d}$$

$$J \le J_{max}(v_{rel}) \tag{6.24e}$$

$$J \le J_{max}(b) \tag{6.24f}$$

These conclusions are summarized in Fig. 6.1 where the heavy solid line represents the energetic limit to the formation of BaI (v=0) [7].

Opacity Function Models

I. Crossed-Beam Data

The simplest model describing collisions is the hard sphere model. This model has been proposed to describe the total opacity function [8]. Its functional form is

$$P(b) = H(b_{max}-b) \tag{6.25}$$

where H(x) is the Heavyside (step) function and b_{max} is the limiting value for the impact parameter.

From preliminary analysis it was found that b_{max} would be very nearly equal to $b_{max}(v_{rel})$ as defined in Eq. 6.24a. A nonlinear least-squares fit [9] was performed on the BaI (v=0) data set (Fig. 5.4) with the bond dissociation energy of BaI, $D_0^0(\mathrm{BaI})$, as the only adjustable parameter. The limitations of the model become apparent in Fig. 6.2a. A narrower range of impact parameters is required to describe the data.

Noda and Zare [10] in a theoretical approach to the same reaction proposed a constant product recoil energy model (CPR). In this model the expression 6.24a is used as an equality. A fit was performed using the same data with considerable success (see Fig. 6.2b). The fact that the simulated rotational distribution was narrower than the experimental one suggested that a small but finite spread in the opacity function would improve the simulation.

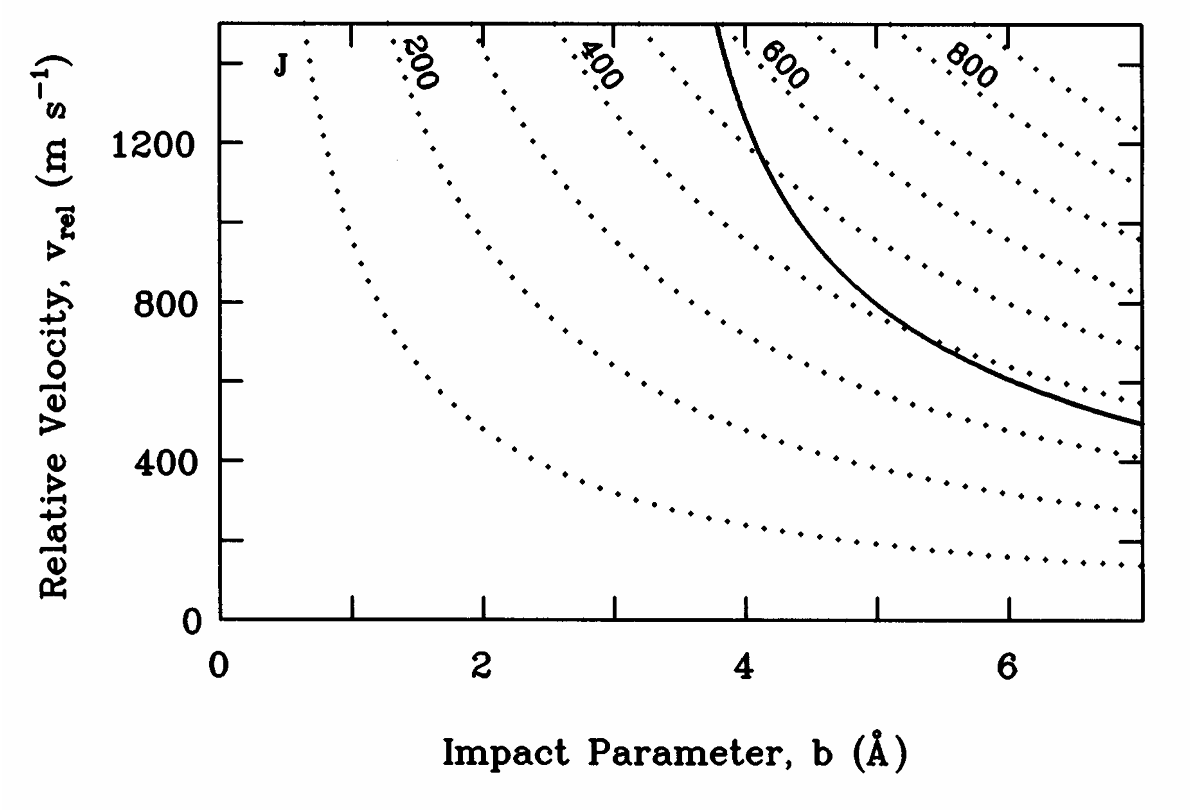

Figure 6.1. Energy limitations on the relative velocity and impact parameter. The solid line partitions the plane in reactive and nonreactive combinations of v_{rel} and b. The dotted hyperbolas correspond to combinations that lead to products of constant J which is indicated at the top.

A more sophisticated model was the so-called "truncated Gaussian" model, which was similar to a model tried before [11]. The general form of the opacity function was a Gaussian which was truncated by the energetic limit in accordance with Eq. 6.24a.

$$P_0(b) = \exp\left[-\frac{1}{2}\left(\frac{b-\beta_0}{\sigma_0}\right)^2\right] H\left[b_{max}(v_{rel}) - b\right] \qquad (6.26)$$

In a fit performed on all available data for BaI (v=0) rotational distributions, the adjustable parameters were β_0, σ_0, and $D_0^0(\mathrm{BaI})$. The results are shown in Fig. 6.2c and 6.3.Similar fits for BaI (v=1) and BaI (v=2) data are shown in Fig. 6.4 and 6.5.

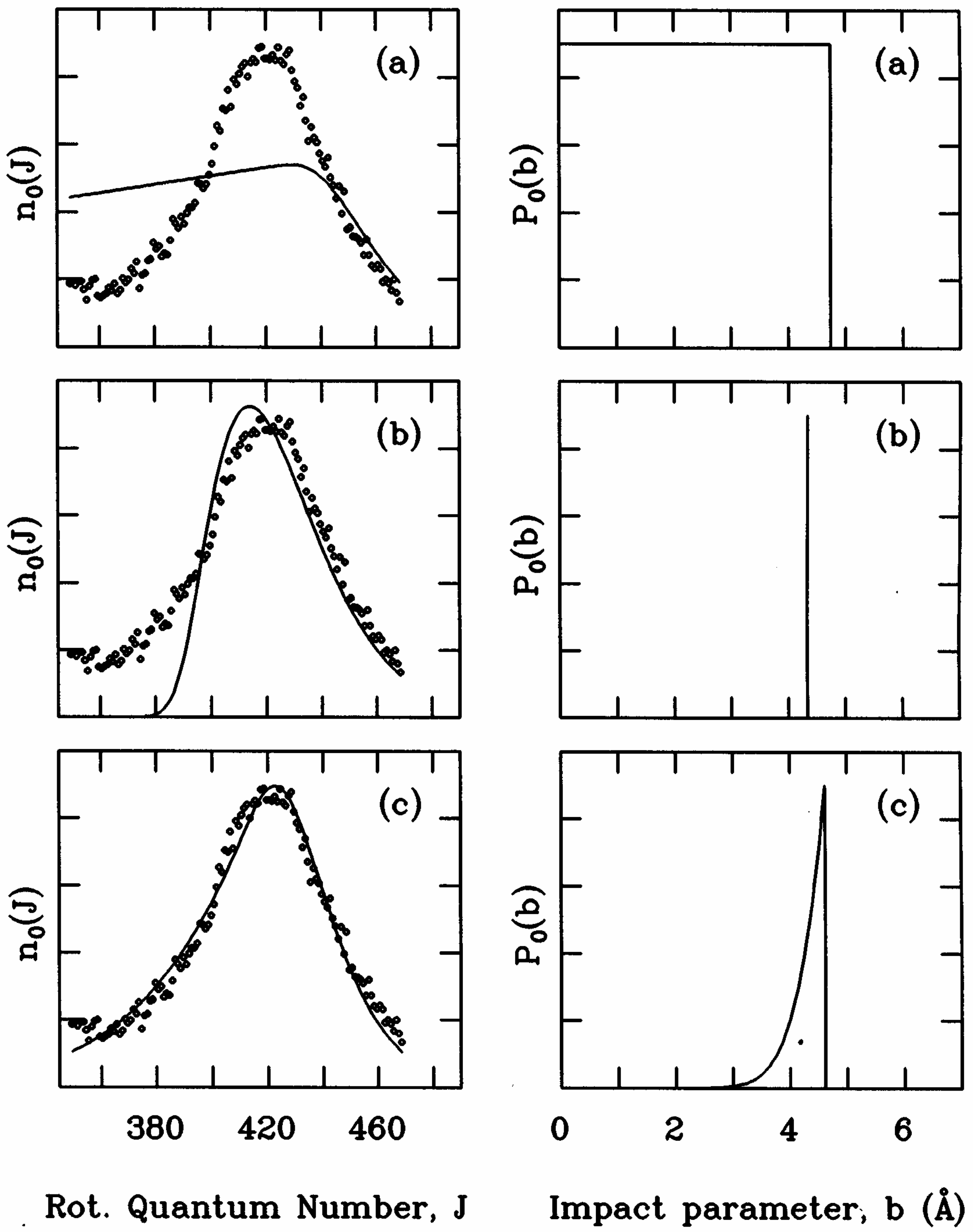

Figure 6.2. Rotational distributions simulations and specific opacity model for BaI (v=0). (a) Hard-sphere model [D_0^0(BaI) = 79.2 (2) kcal mol^{-1}]. (b) "Constant product recoil" model [D_0^0(BaI) - E_{rec} = 76.66 (4) kcal mol^{-1}]. (c) "Truncated Gaussian" model [β_0 = 6.09 (5) Å, σ_0 = 0.85 Å, D_0^0(BaI) = 78.42 (2) kcal mol^{-1}].

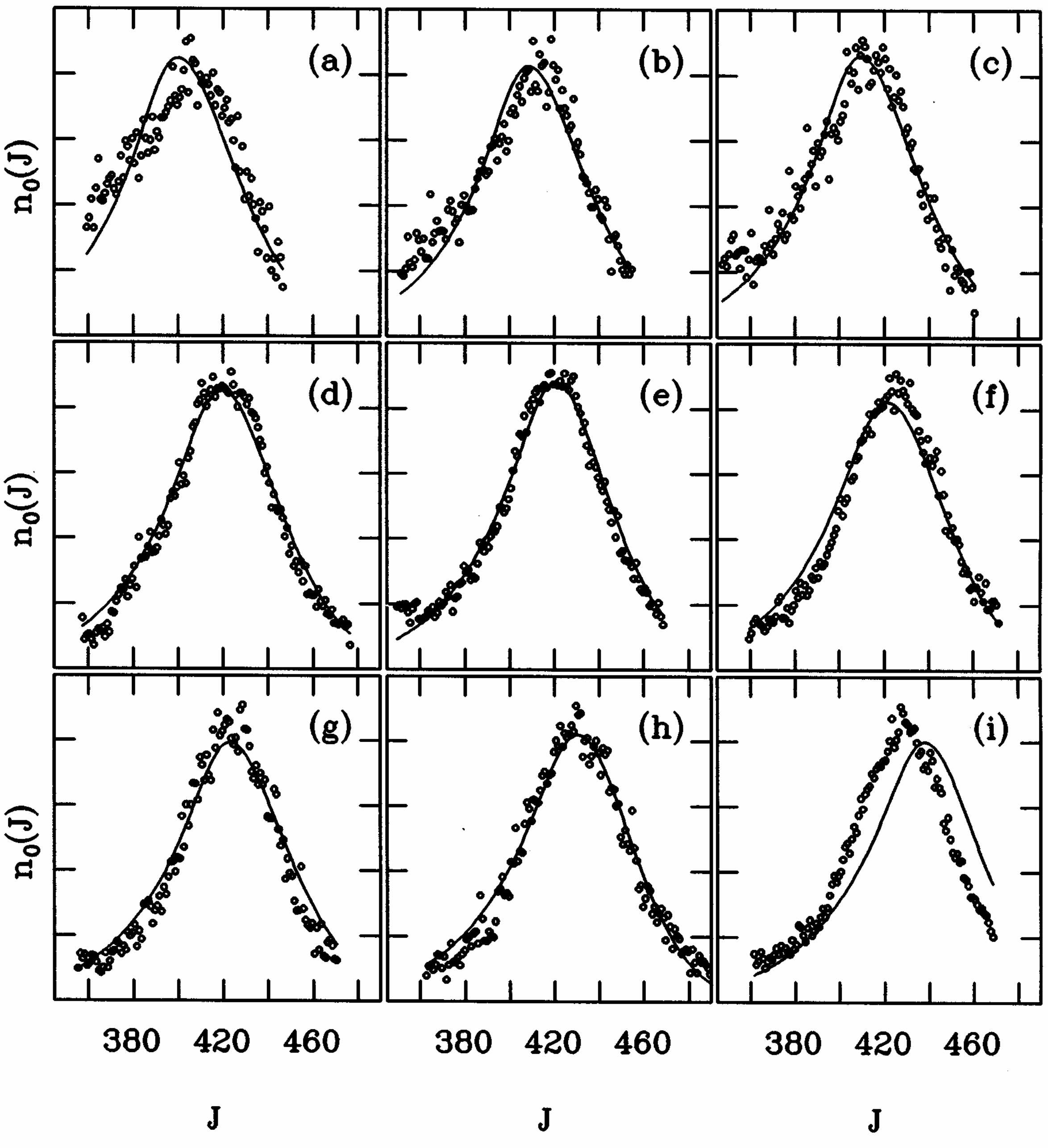

Figure 6.3. Experimental and simulated rotational distributions for BaI (v=0) obtained under various relative velocities (listed in order of increasing average relative velocity) and using the "truncated Gaussian" model. The parameter values were $\beta_0 = 5.1$ (1) Å, $\sigma_0 = 0.4$ (1) Å, and $D_0^0(\mathrm{BaI})$ = 78.48 (3) kcal mol^{-1}.

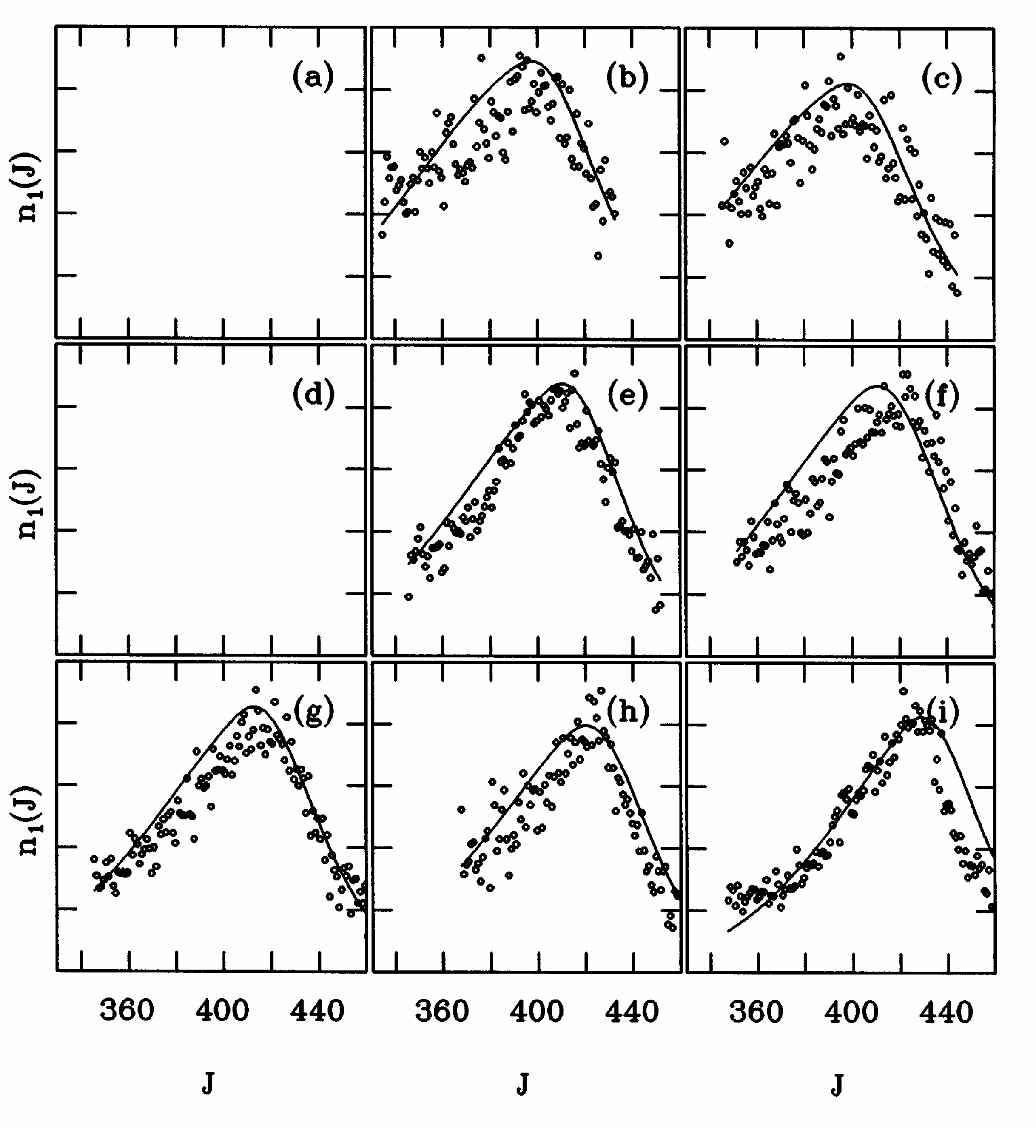

Figure 6.4. Experimental and simulated rotational distributions for BaI (v=1) obtained under various relative velocities (listed in order of increasing average relative velocity) and using the "truncated Gaussian" model. The parameter values were $\beta_1 = 4.39$ (4) Å, $\sigma_1 = 0.53$ (3) Å, and D_0^0(BaI) = 78.1 kcal mol^{-1}.

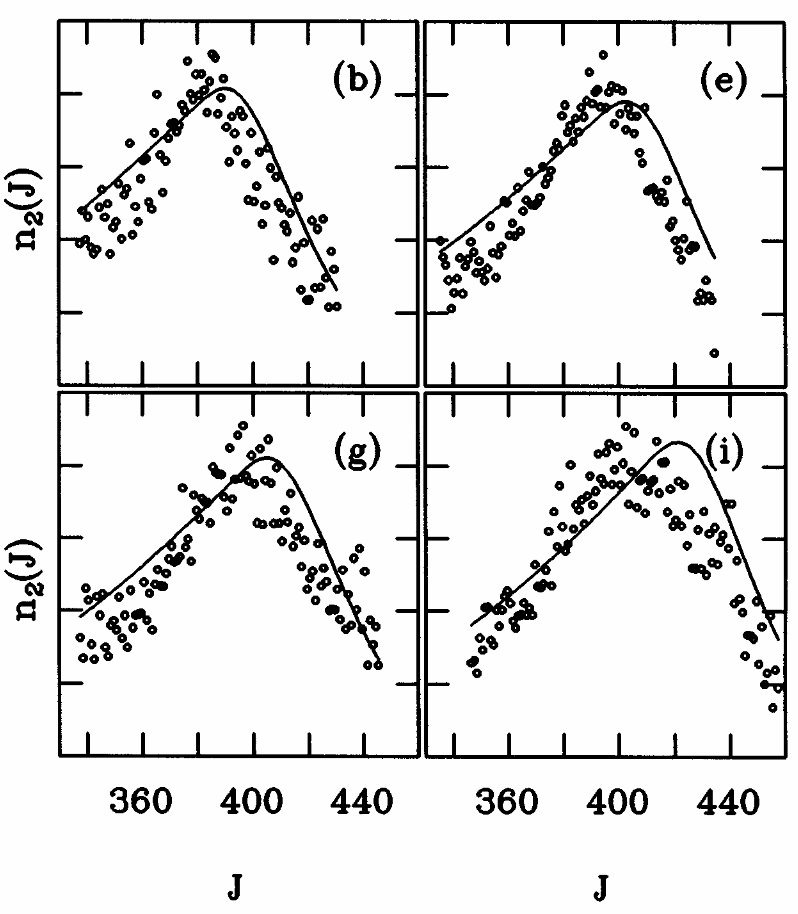

Figure 6.5. Experimental and simulated rotational distributions for BaI (v=2) obtained under various relative velocities (listed in order of increasing average relative velocity) and using the "truncated Gaussian" model. The parameter values were $\beta_2 = 4.9$ (4) Å, $\sigma_2 = 1.1$ (3) Å, and $D_0^0(\mathrm{BaI}) = 78.1$ kcal mol^{-1}.

II. Beam-Gas Data

The variation in the position of the maximum in the rotational distribution for each vibrational level of BaI is a very strong indication that different impact parameters lead preferentially to different vibrational states. The dynamic character of this behavior is confirmed by the fact that the reaction process is not solely governed be energetics, because the energy content of the products in different vibrational levels varies. This argument eliminates the hard-sphere model from further consideration.

The model used to fit the beam-gas rotational distributions was the "truncated Gaussian" model. Equation 6.26 was written in a more general form:

$$P_v(b) = \exp\left[-\frac{1}{2}\left(\frac{b-\beta_v}{\sigma_v}\right)^2\right] H\left[b_{\max,v}\left(v_{\text{rel}}\right)-b\right] \tag{6.27}$$

In this case the energy limitations affected a small section of the Gaussian form and then only for the lowest vibrational levels. Consequently, D_0^0(BaI) could not be determined from the data. It was set equal to a value compatible with the results for the BaI (v=0) rotational distributions measured under crossed-beam conditions, namely 78.1 kcal mol^{-1}.

In an initial fitting procedure σ_v was set equal to 0.2 Å for all v. The data for v=4 gave a good fit, but for higher v values the simulated distributions were narrower than the experimental ones. The calculations failed to reproduce the highly excited, sharply peaked experimental distribution for BaI (v=0). σ_v was allowed to increase for higher v values until the simulations matched the data. These results are shown in Figs. 6.6 and 6.7.

The rotational distribution for the lowest vibrational level exhibited a maximum at very high energies. Any doubts as to the accuracy of the experimental data were dispelled by repeated measurements using both possible SDLIF schemes and undispersed LIF. This observation was an indication that a significant portion of the relative velocity distribution is not reactive to form BaI (v=0). A "static" energy barrier of 2.6 kcal mol^{-1} has been proposed in the past [12]. It would seem unlikely that Ba (a polarizable atom) and HI (a weak dipole) would experience any long-range interaction other than dipole-induced dipole attraction. A "fixed" energy barrier should be present in the reaction path for any product vibrational level, but it had not been necessary to invoke a barrier to fit

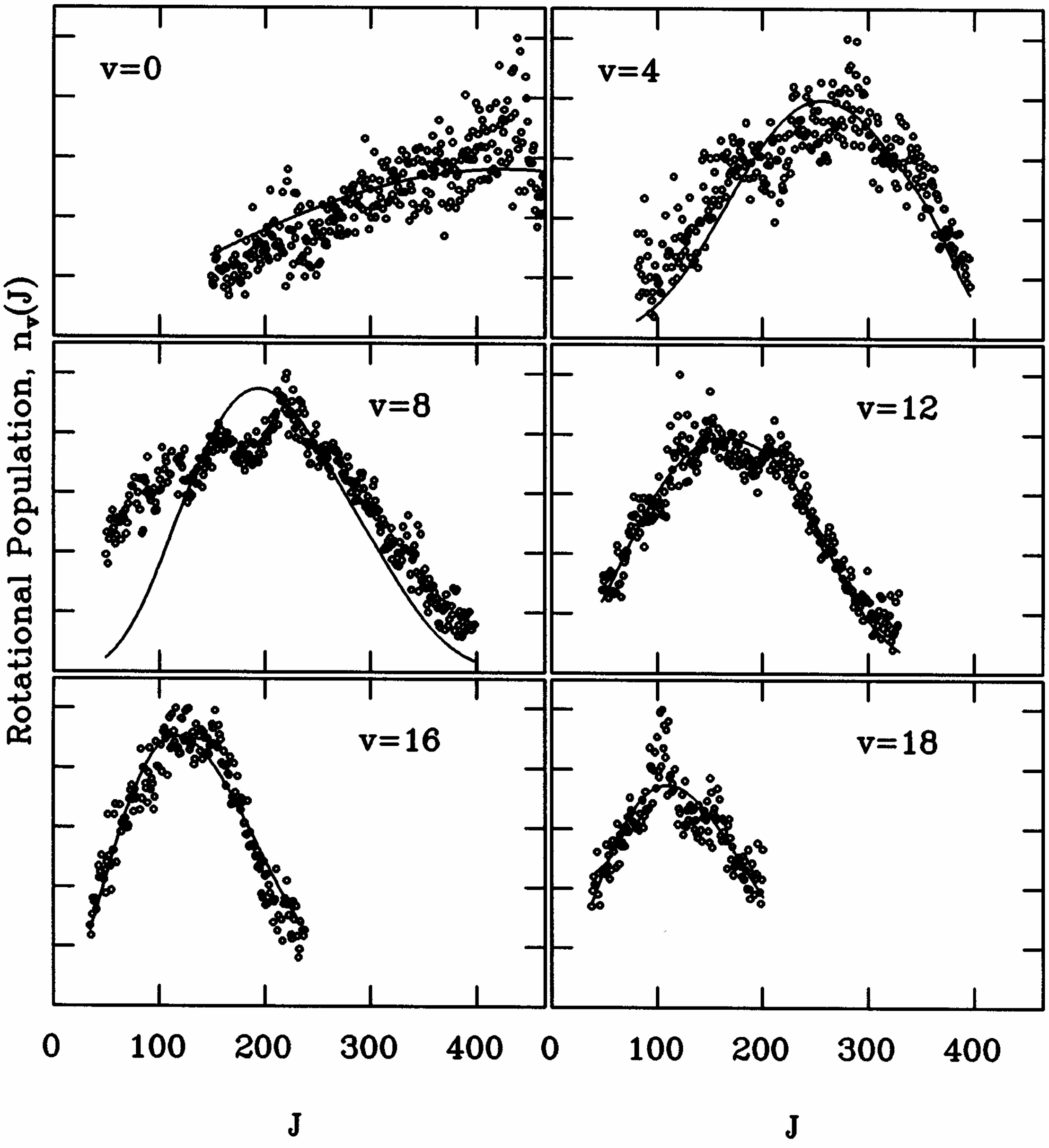

Figure 6.6. Experimental and simulated rotational distributions for BaI (v) obtained under beam-gas conditions and using the "truncated Gaussian" model. The parameter values used are shown in Fig. 6.7.

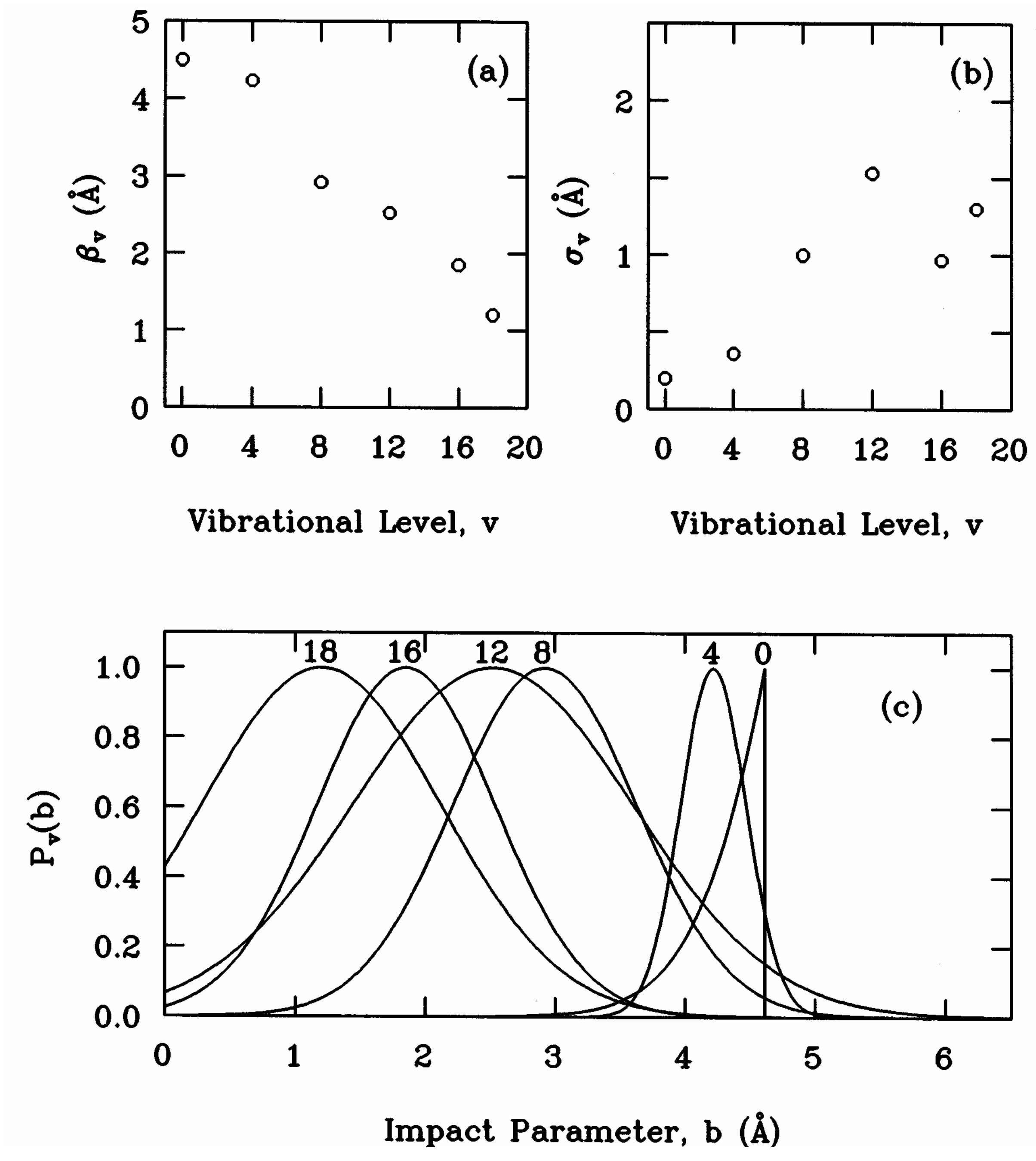

Figure 6.7. Specific opacity functions for BaI (v). (a) The most probable impact parameters and (b) the Gaussian widths for different product vibrational levels. (c) The full form of the specific opacity functions. Parameter values used: $\beta_4 = 4.23$ (3) Å, $\sigma_4 = 0.36$ (7) Å, $\beta_8 = 2.92$ (3) Å, $\sigma_8 = 1$ Å, $\beta_{12} = 2.52$ (4) Å, $\sigma_{12} = 1.53$ (9) Å, $\beta_{16} = 1.85$ (3) Å, $\sigma_{16} = 0.97$ (4) Å, $\beta_{18} = 1.2$ (1) Å, $\sigma_{18} = 1.3$ (1) Å.

the data for v between 4 and 18.

The possibility of the existence of a barrier is supported by the following argument. Although the SDLIF scheme cannot measure the populations of levels with J below 40, recent data not yet analyzed in detail indicate that the rotational populations at low J values are small, even for the highest vibrational levels investigated, viz., v between 18 and 24. This situation could be explained with the presence of an activation barrier: Low J products arise when both v_{rel} and b are small. Slow collisions are not reactive because of the barrier and small b values are rare because each impact parameter is weighted by its own value (cf. Eq. 6.7).

A different barrier is the "centrifugal" or "angular momentum" barrier (E_{cb}) which is part of the "line-of-centers" model of reactive scattering. A certain fraction of the initial kinetic energy (E_{rel}) proportional to b^2 becomes unavailable for direct collision and reduces the probability of reaction. The size of the barrier is given by

$$E_{cb} = E_{rel}\,\frac{b^2}{d^2} \tag{6.28}$$

where d is the critical distance at which any fixed barrier is overcome or at which the chemical transformation occurs. From its definition this barrier does not exclude any relative velocities in any given range of impact parameters. Such a barrier can only eliminate impact parameter values near or over d.

No satisfactory explanation can be given for the (unexpectedly) high rotational excitation of BaI (v=0). In any event, the data confirm that BaI (v=0) is formed under beam-gas conditions at impact parameters that are at least as high as those determined in the crossed-beam studies (cf. Fig. 5.10). This argument was the underlying spirit in the construction of Fig. 6.7. For v≥4, the opacity functions shown are determined from beam-gas experimental data and the other ones from crossed-beam data.

Theoretical studies of this reaction system are not very extensive. No ab initio energy surface is available for the BaIH system because of the large number of electrons.

Classical trajectory calculations have been carried out [13] on a LEPS potential. $P_v(b)$ was found to be a narrow, unimodal function of b and to overlap with the specific opacity functions for neighboring vibrational levels. In addition, the peak impact parameter values were found to decrease with increasing v, so that the specific opacity functions formed a nested set. the results of our studies are in qualitative agreement with these calculations.

Total Scattering Cross Section

Of particular relevance to the determination of the specific opacity functions presented above are measurements of the total scattering cross section of the Ba beam in HI gas. Briefly, the experiment was a beam-gas study of the Ba + HI reaction where BaI (v=8 or 12) was monitored with SDLIF in a few rotational levels as a function of HI pressure. The pressure measurements were critical to the ensuing calculations, but HI electron impact ionization data are not available to allow calibration of the ionization gauges used in our experiments. We assumed that HI behaves similarly to N_2, for which the gauges are calibrated, and that the error in the pressure was less than 10 %.

Ba atoms in the beam react continuously with HI molecules after they enter the main reaction chamber. The BaI signal measured at the point where the laser beam intersects the Ba beam is given by (cf. Eq. 6.21)

$$n_v(J) = \frac{n_{Ba}\ \ n_{HI}}{v'\ \ S} \int_0^\infty v_{rel}\ \ \sigma_{vJ}\ \ f(v_{rel})\ dv_{rel} \qquad (6.29)$$

When the reagent concentrations are changed, the signal level reflected that. An increase in HI pressure affected both n_{HI} and n_{Ba}, because HI molecules scattered ("absorbed") more Ba from its beam by some kind of scattering mechanism (elastic, inelastic, or reactive). The effective value of n_{Ba} at the probe region was

$$n_{Ba} = n_{Ba}^0\ \exp(-\sigma\ d\ n_{HI}) \qquad (6.30)$$

where n_{Ba}^0 is the value of n_{Ba} at the boundary of the chamber, d is the distance traveled by the Ba atoms through the HI gas, and σ is the total scattering cross section. Combining Eqs. 6.25 and 6.26, we get

$$n_v(J) = A\, n_{HI} \exp(-\sigma\, d\, n_{HI}) \tag{6.31}$$

where A has incorporated all constants.

The average intensity of several consecutive rovibronic transitions in the BaI $C^2\Pi_{3/2}$ - $X^2\Sigma^+$ (v,v) P_2 branch was recorded for each HI pressure. The measurements are shown in Fig. 6.8. The data were fit by Eq. 6.27 assuming ideal gas behavior for HI at the operating temperature (300 K) and that d = 4.5 cm. The total collision cross section was found to be 64 $Å^2$ from the BaI (v=8, J=279.5-282.5) measurements and 69 $Å^2$ from the BaI (v=12,J=150.5-184.5) measurements. These cross sections correspond in a hard sphere model to maximum impact parameters of 4.5 Å and 4.7 Å, respectively.

The hard sphere radii of Ba and HI are not very well known, but their sum is clearly less than 4.5 Å. We conclude, therefore, that the scattering cross section originates almost exclusively from reactive scattering. Furthermore, recalling that the maximum impact parameter value for the formation of BaI in any state is b_{max} = 4.5 Å which corresponds to BaI (v=0), we observe that the peak value of $P_0(b)$ must approach unity at b_{max} and that at any b value the total opacity function (cf. Eq. 6.8) has also a value of unity. In other words, the reaction occurs with very high probability whenever the impact parameter of a collision between Ba and HI is less or equal to 4.5 Å.

Conclusions

Crossed-beam and beam-gas product rational distributions have enable us to map out the specific opacity functions of the reaction Ba + HI → BaI + H. It was found that the opacity functions could be approximated by Gaussian functions of the impact parameter. All results are presented compactly in Fig. 6.7.

The position of the maximum follows a clear trend. The opacity function for BaI

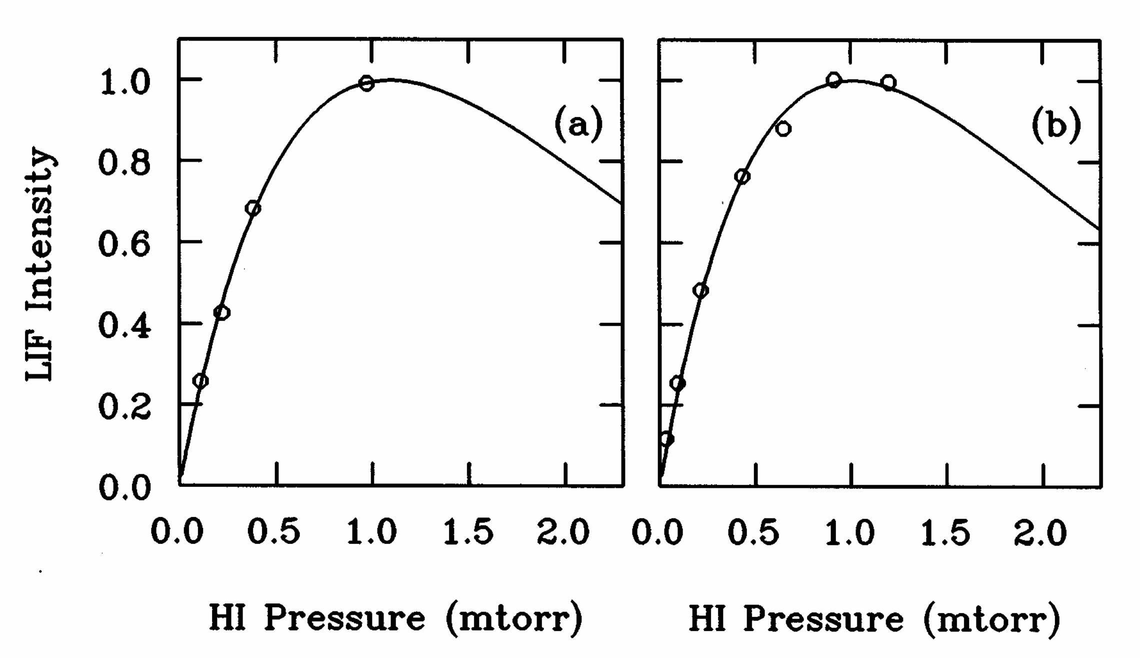

Figure 6.8. BaI (v) product yield as a function of HI pressure in beam-gas experiments. Results for (a) v = 8 and (b) v = 12.

(v=0) is sharply peaked at the energetic limit of the system with b = 4.5 Å. At higher vibrational levels, $P_V(b)$ becomes broader, more symmetric, and its peak value decreases. The implication is that the vibrational state in which BaI is formed is determined primarily by the impact parameter of the collision between Ba and HI, although the collision velocity and the orientation angle are expected to have some effect. A 1:1 mapping is found in which reactive collisions with large impact parameters correspond to BaI products in low states of vibrational excitation. This correlation becomes less exact for higher vibrational levels where the specific opacity functions overlap extensively.

Seen from a different perspective the present study provides a measure of atomic and molecular sizes. The apparent size of a Ba atom approached by a HI molecule is a function of the vibrational state BaI that will be formed.

The impact parameter values found can be compared with the equilibrium bond length of BaI, viz. 3.08 Å, which remains largely the same at the vibrational or rotational levels under consideration. Clearly the reaction starts taking place well before Ba and I have reached their final configuration.

This study has exploited the extreme case of a kinematically constrained system to deduce the nature of the specific opacity function. The same technique should be applicable to less kinematically constrained reactions to uncover the hidden role of the impact parameter in a chemical reaction.

References

1 D. R. Herschbach, *Faraday Discuss. Chem. Soc.* **33**, 281 (1962); D. R. Herschbach, *Adv. Chem. Phys.* **10**, 319 (1966).

2 S. Datz, D. R. Herschbach, and E. H. Taylor, *J. Chem. Phys.* **35**, 1549 (1961).

3 P. H. Vaccaro, D. Zhao, A. A. Tsekouras, C. A. Leach, W. E. Ernst, and R. N. Zare, *J. Chem. Phys.* **93**, 8544 (1990).

4 J. Vigué, P. Grangier, and A. Aspect, *Phys. Rev. A* **30**, 3317 (1984)

5 R. D. Levine and R. B. Bernstein, "Molecular Reaction Dynamics and Chemical Reactivity," Oxford University Press, New York, 1987.

6 C. A. Leach, A. A. Tsekouras, P. H. Vaccaro, R. N. Zare, and D. Zhao, *Faraday Discuss. Chem. Soc.* **91**, 183 (1991).

7 P. H. Vaccaro, A. A. Tsekouras, D. Zhao, C. A. Leach, and R. N. Zare, *J. Chem. Phys.* **96**, 2786 (1992).

8 A. Siegel and A. Schultz, *J. Chem. Phys.* **76**, 4513(1982).

9 D. W. Marquardt, *J. Soc. Ind. Appl. Math.* **11**, 431 (1962).

10 C. Noda and R. N. Zare, *J. Chem. Phys.* **86**, 3968 (1987).

11 C. Noda, J. S. McKillop, M. A. Johnson, J. R. Waldeck, and R. N. Zare, *J. Chem. Phys.* **85**, 856 (1986).

12 C. A. Mims, S.-M. Lin, and R. R. Herm, *J. Chem. Phys.* **57**, 3099 (1972).

13 D. Zhao and R. N. Zare, in preparation.

Appendix C. Computer Code for Simulations of Rotational Distributions

The following computer code written in FORTRAN language can simulate BaI rotational distributions using Eq. 6.21 given the velocity parameters of the reagents and adjustable parameters for the specific opacity function. The adjustable parameters are optimized with a nonlinear least-squares fit, the main algorithm of which procedure has been omitted from the following listing. The calculation of the relative velocity distribution is based on Eqs. 3.11 and 3.12. The model for the opacity function used is the "truncated Gaussian" model (see Eq. 6.26 and 6.24) expanded to include optionally a centrifugal barrier, a "fixed" energy barrier, or an attractive potential in conjunction with a centrifugal barrier.

```
        PROGRAM JAYS

C       to fit many rotational distributions.

        PARAMETER NEXP0 = 20, NDAT0 = 150, NN0 = NEXP0 * NDAT0
        COMMON /BLOCK1/ PARAM(40), ICON(40), NPARAM
        COMMON /BLOCK2/ DECDAT(NN0), DECTIM(NN0), IND(NN0), NDATA
        COMMON /BLOCK3/ NSTART, NEND, NUMBER
        COMMON /EXPVAR/ VAREXP(NEXP0,10), NXP
        COMMON /BLOCK5/ ACTION
        COMMON /BLK8/   NPT

        REAL*8 PARAM, DECDAT, DECTIM
        REAL*8 SIGMA(30), DELTA(30), BETA(30), PTEMP(30)
        REAL*8 ARRAY(30,30), ALPHA(30,30), DERIV(30,NN0)
        REAL*8 DECCAL(NN0), DERIT(NN0), WEIGHT(NN0), WSCALE
        REAL*8 CHIA, CHIB, VARNCE, LAMBDA, COSINE, NU, TAU
        REAL*8 DETERM, SIGMA0, STEP, DEL, REFCOS, EPSILN
        REAL*8 TEMP, PEMP, SXY, SX2, SY2, VAREXP
        DIMENSION NUMFIT(30), IXPST(NEXP0), IXPEN(NEXP0)
        CHARACTER DBYTE*9, TBYTE*8, FILEIN*40, ACTION*10

        DATA DEL          /      1.0D-5       /
        DATA REFCOS       /   7.071067812D-1  /
        DATA EPSILN       /      1.0D-6       /
        DATA TAU          /      0.3D-38      /
        DATA NU           /      1.0D+1       /
        DATA ILIMIT       /      12           /

        CALL DATE (DBYTE)
        CALL TIME (TBYTE)
        WRITE(7,7800) DBYTE, TBYTE
        WRITE(7,9900)

        IXP = 1
        NDATA = 0
        N = 1500
400     WRITE(6,6700)
        READ (9,6100,END=570) FILEIN
        OPEN(8,NAME=FILEIN,ACCESS='SEQUENTIAL',TYPE='OLD',READONLY,
     X  ERR=430,FORM='FORMATTED')
        GOTO 450
430     WRITE(6,6800) FILEIN(1:LENGTH(FILEIN))//CHAR(7)
        GOTO 400

450     WRITE(6,6900)
        READ (9,6200) NSTART
        IF (NSTART .EQ. 0) NSTART = 1
        WRITE(6,7000)
        READ (9,6200) NEND
        IF (NEND .EQ. 0) NEND = N
        WRITE(6,7100)
        READ (9,6300) WSCALE
        IF ( WSCALE .EQ. 0.0D0 ) WSCALE = 1

        DO 490 I = 1, NSTART - 1
490     READ(8,*,END=492) X, X
        GOTO 495
492     I = 1
        GOTO 550
495     DO 500 I = NDATA + 1, NDATA + NEND
        READ(8,*,END=550) DECTIM(I), DECDAT(I)
        WEIGHT(I) = WSCALE
500     IND(I) = IXP
550     CLOSE(8)
        IXPST(IXP) = NDATA + 1


        NDATA = I - 1
        IXPEN(IXP) = NDATA
        WRITE(7,7200) IXP, FILEIN, IXPST(IXP), IXPEN(IXP), WSCALE
        PRINT 7200, IXP, FILEIN, IXPST(IXP), IXPEN(IXP), WSCALE

        DO 560 IVAR = 1, 6
        WRITE(6,7300) IVAR, IXP
560     READ (9,6300) VAREXP(IXP,IVAR)
C       VAREXP holds velocity and other parameters for the IXPth experiment.

        IXP = IXP + 1
        GOTO 400

570     NXP = IXP - 1
        CLOSE(9)
        NSTART=1
        NEND = NDATA
        NUMBER = NEND - NSTART + 1

600     CALL GETPARAM ( 1 )

        CALL START

        WRITE(6,7400)
        READ (5,6300) LAMBDA
        LAMBDA = LAMBDA * NU

        WRITE(6,7500)
        READ (5,6200) NPT
        IF (NPT.EQ.0) NPT = 100000

        WRITE(6,7600)
        READ (5,6200) NREP

        WRITE(6,7700)
        READ (5,6100) ACTION

        CLOSE(5)

        SIGMA0 = 0.0D0
        DO 800 N = 1, NUMBER
800     SIGMA0 = SIGMA0 + 1.0D0 / WEIGHT(N)**2

        NFIT = 0
        DO 900 I=1, NPARAM
        IF ( ICON(I) .NE. 1 ) GO TO 900
        NFIT = NFIT + 1
        NUMFIT(NFIT) = I
900     CONTINUE
        PRINT *,'Rotational Distribution Data from ',NXP,' files.'
******************************************************************

        IPASS  = 0
        NFINIS = 0
        DETERM = 0.0D0

        CHIA   = 0.0D0
        CALL CONCAL ( DECCAL )
        DO 930 IXP = 1, NXP
        SXY = 0
        SX2 = 0
        SY2 = 0
        DO 920 I = IXPST(IXP), IXPEN(IXP)
        SXY = SXY + DECCAL(I) * DECDAT(I+NSTART-1)
        SY2 = SY2 + DECDAT(I+NSTART-1) **2
920     SX2 = SX2 + DECCAL(I) **2
        NN = IXPEN(IXP) - IXPST(IXP) + 1
        VAREXP(IXP,7) = SXY / SX2
        VAREXP(IXP,8) = (SY2/SX2 - (SXY/SX2)**2) / (NN-1)
        VAREXP(IXP,10) = (SY2 - SXY**2/SX2) / (NN - NFIT - 1)
C       VAREXP(IXP,7) is the optimum amplitude coefficient for experiment IXP.
C       VAREXP(IXP,8) is the variance of VAREXP(IXP,7).
C       VAREXP(IXP,10) is the variance of the fit of VAREXP(IXP,7),reduced chi^2
        DO 930 I = IXPST(IXP), IXPEN(IXP)
930     DECCAL(I) = DECCAL(I) * VAREXP(IXP,7)

        DO 1000 N=1, NUMBER
1000    CHIA = CHIA + ( (DECDAT(N+NSTART-1) - DECCAL(N)) / WEIGHT(N) )**2
        CHIA = CHIA / (NUMBER - NFIT)

1500    WRITE(7,8000) IPASS
        PRINT *,'Pass : ', IPASS
        WRITE(7,8100)
        DO 1800 I=1, NPARAM
        PRINT *,PARAM(I)
        IF ( ICON(I) .NE. 0 ) GO TO 1600
        WRITE(7,8200) I, ' ', PARAM(I)
        GO TO 1800
1600    IF ( ICON(I) .NE. 1 ) GO TO 1700
        WRITE(7,8300) I, PARAM(I), SIGMA(I), DELTA(I)
        GO TO 1800
1700    WRITE(7,8200) I, 'c', PARAM(I)
1800    CONTINUE
        IF (IPASS.EQ.0) GOTO 1850
        WRITE(7,8400) DETERM, LAMBDA*DBLE(AMIN0(1,IPASS))
        WRITE(7,8500) COSINE, STEP
1850    WRITE(7,8600) CHIA
        PRINT *, CHIA

        IF ((NREP .NE. 0) .AND. (NFIT .NE. 0)) GO TO 1900
        NFINIS = 4
        WRITE(7,8700) IPASS
        GO TO 4060

1900    IF ((IPASS .LT. NREP) .OR. (NREP .LT. 0)) GO TO 2000
        WRITE(7,8700) IPASS
        NFINIS = 2
        LAMBDA = 0.0D0
        GO TO 2600

2000    IPASS  = IPASS + 1
        ISUB   = 0
        LAMBDA = LAMBDA / NU

        DO 2200 K=1, NFIT
        K0    = NUMFIT(K)
        TEMP = PARAM(K0)
        PARAM(K0) = (1.0D0 + DEL)*TEMP
        IF (TEMP .EQ. 0.0D0) PARAM(K0) = DEL
        CALL CONCAL ( DERIT )
        DO 2030 IXP = 1, NXP
        SXY = 0
        SX2 = 0
        DO 2020 I = IXPST(IXP), IXPEN(IXP)
        SXY = SXY + DERIT(I) * DECDAT(I+NSTART-1)
2020    SX2 = SX2 + DERIT(I) **2
        VAREXP(IXP,7) = SXY / SX2
        DO 2030 I = IXPST(IXP), IXPEN(IXP)
2030    DERIT(I) = DERIT(I) * VAREXP(IXP,7)

        DO 2100 N=1, NUMBER


        DERIV(K,N) = (DERIT(N) - DECCAL(N)) / DEL
2100    IF (TEMP .NE. 0.0D0) DERIV(K,N) = DERIV(K,N) / TEMP
2200    PARAM(K0) = TEMP

        DO 2300 K=1, NFIT
        BETA(K) = 0.0D0
        DO 2300 N=1, NUMBER
2300    BETA(K) = BETA(K) + DERIV(K,N)*(DECDAT(N+NSTART-1)-DECCAL(N))/
     1          WEIGHT(N)**2

        DO 2450 K=1, NFIT
        DO 2450 I=1, K
        ALPHA(I,K) = 0.0D0
        DO 2400 N=1, NUMBER
2400    ALPHA(I,K) = ALPHA(I,K) + DERIV(K,N)*DERIV(I,N)/WEIGHT(N)**2
2450    ALPHA(K,I) = ALPHA(I,K)

        DO 2500 I=1, NFIT
2500    BETA(I) = BETA(I) / DSQRT( ALPHA(I,I) )

2600    DO 2800 K=1, NFIT
        DO 2700 I=1, NFIT
2700    ARRAY(I,K) = ALPHA(I,K) / DSQRT( ALPHA(I,I) ) /
     1               DSQRT( ALPHA(K,K) )
2800    ARRAY(K,K) = ARRAY(K,K) + LAMBDA

        CALL MATINV( ARRAY, 30, NFIT, DETERM )
        IF (DETERM .NE. 0.0D0) GO TO 2850

        WRITE(7,10600) IPASS
        GO TO 4900

2850    IF ( NFINIS .NE. 0 ) GO TO 4000

        DO 3000 I=1, NFIT
        N          = NUMFIT(I)
        DELTA(N) = 0.0D0
        DO 2900 K=1, NFIT
2900    DELTA(N) = DELTA(N) + ARRAY(I,K)*BETA(K)
        DELTA(N) = DELTA(N) / DSQRT( ALPHA(I,I) )
3000    PTEMP(I) = PARAM(N)

        TEMP   = 0.0D0
        PEMP   = 0.0D0
        COSINE = 0.0D0
        DO 3010 I=1, NFIT
        N      = NUMFIT(I)
        COSINE = COSINE + DELTA(N)*BETA(I)
        TEMP   = TEMP + DELTA(N)**2
3010    PEMP   = PEMP + BETA(I)**2
        COSINE = COSINE / DSQRT(TEMP) / DSQRT(PEMP)

        STEP   = 1
3020    DO 3040 I=1, NFIT
        IF (DABS(STEP*DELTA(NUMFIT(I))) .GE. EPSILN*DABS(TAU+PTEMP(I)))
     1                                 GO TO 3120
3040    CONTINUE

        WRITE(7,8800) IPASS - 1
        NFINIS = 1
3060    LAMBDA = 0.0D0
3080    DO 3100 I=1, NFIT
3100    PARAM(NUMFIT(I)) = PTEMP(I)
        GO TO 2600

3120    DO 3140 I=1, NFIT
```

```
        N = NUMFIT(I)
3140    PARAM(N) = PTEMP(I) + STEP*DELTA(N)

        CHIB = 0.0D0
        CALL CONCAL ( DECCAL )
        DO 3155 IXP = 1, NXP
        SXY = 0
        SX2 = 0
        SY2 = 0
        DO 3150 I = IXPST(IXP), IXPEN(IXP)
        SXY = SXY + DECCAL(I) * DECDAT(I+NSTART-1)
        SY2 = SY2 + DECDAT(I+NSTART-1) **2
3150    SX2 = SX2 + DECCAL(I) **2
        NN = IXPEN(IXP) - IXPST(IXP) + 1
        VAREXP(IXP,7) = SXY / SX2
        VAREXP(IXP,8) = (SY2/SX2 - (SXY/SX2)**2) / (NN-1)
        VAREXP(IXP,10) = (SY2 - SXY**2/SX2) / (NN - NFIT - 1)
        DO 3155 I = IXPST(IXP), IXPEN(IXP)
3155    DECCAL(I) = DECCAL(I) * VAREXP(IXP,7)
        PRINT *,IPASS, LAMBDA
        DO 3160 N=1, NUMBER
3160    CHIB = CHIB + ( (DECDAT(N+NSTART-1) - DECCAL(N)) / WEIGHT(N) )**2
        CHIB = CHIB / (NUMBER - NFIT)

        IF (CHIB .LE. CHIA) GO TO 3200

        ISUB = ISUB + 1
        IF (ISUB .LE. ILIMIT) GO TO 3180
        WRITE(7,8900) IPASS - 1
        NFINIS = 3
        GO TO 3060

3180    IF (COSINE .LT. REFCOS) GO TO 3190

        STEP = 5.0D-1 * STEP
        GO TO 3020

3190    LAMBDA = LAMBDA*NU
        GO TO 3080

3200    DO 3300 I=1, NFIT
3300    SIGMA(NUMFIT(I)) = DSQRT(CHIB*ARRAY(I,I) / ALPHA(I,I))
3400    CHIA = CHIB
        GO TO 1500

*****************************************************************
4000    DO 4020 K=1, NFIT
        DO 4020 I=1, NFIT
4020    ARRAY(I,K) = CHIA * ARRAY(I,K) / DSQRT( ALPHA(I,I) ) /
     1                  DSQRT( ALPHA(K,K) )

        DO 4040 K=1, NFIT
        SIGMA(NUMFIT(K)) = DSQRT(ARRAY(K,K))
        DO 4040 I=K, NFIT
        IF (I .EQ. K) GO TO 4040
        ARRAY(I,K) = ARRAY(I,K) / DSQRT( ARRAY(I,I) ) /
     1                  DSQRT( ARRAY(K,K) )
4040    CONTINUE

4060    VARNCE = DBLE(FLOAT(NUMBER)) * CHIA / SIGMA0
        WRITE(7,9000)
        WRITE(7,9100)
        DO 4600 IXP = 1, NXP
4600    WRITE(7,9300) IXP, VAREXP(IXP,7), DSQRT(VAREXP(IXP,8))
        WRITE(7,9900)
        DO 4175 I=1, NPARAM


        IF ( ICON(I) .NE. 0 ) GO TO 4100
        WRITE(7,9200) I, ' ', PARAM(I)
        GO TO 4175
4100    IF ( ICON(I) .NE. 1 ) GO TO 4150
        WRITE(7,9300) I, PARAM(I), SIGMA(I)
        GO TO 4175
4150    WRITE(7,9200) I, 'c', PARAM(I)
4175    CONTINUE
        WRITE(7,9900)
        DO 4178 IXP = 1, NXP
4178    WRITE(7,10000) IXP, VAREXP(IXP,10)
        WRITE(7,9400) CHIA
        WRITE(7,9500) VARNCE
        WRITE(7,9600) DSQRT(VARNCE)

        IF (ACTION(1:1).NE.'Y') GOTO 4200
        OPEN(9,NAME='resu',TYPE='NEW',FORM='FORMATTED')
        DO 4180 I = 1, NUMBER
4180    WRITE(9,10100) DECTIM(I+NSTART-1),DECDAT(I+NSTART-1),DECCAL(I)
        CLOSE(9)

4200    IF ((NREP .EQ. 0) .OR. (NFIT .EQ. 0)) GO TO 4500

        WRITE(7,9700)
        DO 4400 K=1, NFIT, 4
        K0 = MIN0(4, NFIT-K+1)
        IF (K0 .EQ. 0) K0 = 4
        DO 4300 I=1, NFIT
4300    WRITE(7,9800) (ARRAY(I,N), N=K, K-1+K0)
4400    WRITE(7,9900)

4500    CALL PREND

4900    CALL DATE (DBYTE)
        CALL TIME (TBYTE)
        WRITE(7,7900) DBYTE, TBYTE

6100    FORMAT(A)
6200    FORMAT(I6)
6300    FORMAT(D24.0)
6700    FORMAT('$Rotational distribution data file : ')
6800    FORMAT(' Unable to access ',A,'.')
6900    FORMAT('$Enter index for first point [1] : ')
7000    FORMAT('$Enter index for last point [N] : ')
7100    FORMAT('$Enter scaled factor for equal weighting [1] : ')
7200    FORMAT(' ',12X,'Experiment',I2,'. ',A,'Data points ',I4,
     X  ' through ',I4,' with weight ',F5.2,'.')
7300    FORMAT('$Enter variable #',I2,' for experiment ',I2,' : ')
7400    FORMAT('$Enter starting value for lambda: ')
7500    FORMAT('$Enter data count interval for intermediate output: ')
7600    FORMAT('$Enter desired number of iterations: ')
7700    FORMAT('$Enter Y/N''s for desired output (RESU,VB,PB,VREC): ')
7800    FORMAT(' ',31X,'Run started on ',A,' at ',A,'.')
7900    FORMAT(' ',31X,'Run ended on ',A,' at ',A,'.')
8000    FORMAT(1H0/1H0, 16X, 19HLeast Squares Pass:, I3)
8100    FORMAT(1H0, 16X, 9HParameter, 11X, 15HParameter Value, 17X,
     1          11HUncertainty, 20X, 9HIncrement/)
8200    FORMAT(1H , 19X, I2, A1, 9X, D24.16)
8300    FORMAT(1H , 19X, I2, 1H*, 3X, 3( 6X, D24.16 ))
8400    FORMAT(1H0, 36X, 12HDeterminant:,D24.16, 6X,
     1          7HLambda:, D24.16)
8500    FORMAT(1H , 41X, 7HCosine:, D24.16, 8X, 5HStep:, D24.16)
8600    FORMAT(1H0,52X,20HReduced Chi Squared:,D24.16)
8700    FORMAT(1H0, 16X, 19HLeast Squares Pass:, I3, 5X,
     1          33HITERATION LIMIT HAS BEEN ACHIEVED)
8800    FORMAT(1H0, 16X, 19HLeast Squares Pass:, I3, 5X,
     1          29HCONVERGENCE HAS BEEN ACHIEVED)
8900    FORMAT(1H0, 16X, 19HLeast Squares Pass:, I3, 5X,
     1          36HITERATION SUBLIMIT HAS BEEN ACHIEVED)
9000    FORMAT(1H1/1H0/1H0, 48X, 32HOUTPUT FROM FINAL LEAST SQUARES ,
     1          4HPASS)
9100    FORMAT(1H0,28X,9HParameter,21X,15HParameter Value,21X,
     1          11HUncertainty/)
9200    FORMAT(1H ,31X, I2, A1, 19X, D24.16)
9300    FORMAT(1H ,31X, I2, 1H*, 9X, 2(10X, D24.16))
9400    FORMAT(1H0,41X,'Reduced Chi Squared :',D24.16)
9500    FORMAT(1H0,52X,'Variance :',D24.16)
9600    FORMAT(1H0,42X,'Standard Deviation :',D24.16)
9700    FORMAT(1H0/1H0,50X,31HCOVARIANCE - CORRELATION MATRIX/)
9800    FORMAT(1H , 5X, 4( 4X, D24.16 ))
9900    FORMAT(1H )
10000   FORMAT(' ',24X,'Reduced Chi Squared for experiment',I2,' :',
     X           D24.16)
10100   FORMAT(F6.1,2F14.6)
10600   FORMAT(1H0/1H0, 40X, 42HFATAL ERROR: Zero Determinant encountered ,
     1          8Hon pass:, I3/)

        END
```

```
        SUBROUTINE CONCAL (DECCAL)

C       Calculates the rotational population distribution for
C       the Ba + HI --> BaI + H system given the parameters for
C       shifted Maxwell distributions of the reactants in the beams
C       or Maxwell distributions of the reactants in a beam and a gas
C       and an adjustable BaI dissociation energy and assuming that
C       only energetically accessible states can be populated.
C       An entrance channel energy barrier is assumed that includes
C       a centrifugal barrier.
C       Alternatively, an attractive dipole-induced dipole potential
C       is taken into account in determining the centrifugal barrier position.

C       The relative velocity distribution is calculated at the
C       beginning and evaluated with spline interpolation.
C       The convolution is done in a single integral over vrel
C       from a J-dependent lower limit to oo.

        PARAMETER NEXP0 = 20, NDAT0 = 150, NN0 = NEXP0 * NDAT0
        PARAMETER LW = 2000, LIW = 500
        PARAMETER EPSREL = 1.D-15, EPSABS = 1.D-5

        COMMON /BLOCK1/ PARAM(40), ICON(40), NPARAM
        COMMON /BLOCK2/ DECDAT(NN0), DECTIM(NN0), IND(NN0), NDATA
        COMMON /BLOCK3/ NSTART, NEND, NUMBER
        COMMON /EXPVAR/ VAREXP(NEXP0,10), NXP
        COMMON /ENERGY/ EJ(700)
        COMMON /BLK2/   FACT, CF
        COMMON /BLK3/   B0, BETA
        COMMON /BLK4/   J
        COMMON /BLK7/   Vmin(NEXP0), Vmax(NEXP0), VMP(NEXP0)
        COMMON /BLK8/   NPT
        COMMON /BLKFV/  IXP

        REAL*8 PARAM, DECTIM, DECDAT, DECCAL(NEXP0*NDAT0), EJ
        REAL*8 FACT, CF, Y, VAREXP, B0, BETA
        REAL*8 ABSERR, W(LW), FF, Vmin, Vmax, VMP, Vmn
        REAL*8 Ebar, RR
        REAL*4 J
        DIMENSION IW(LIW)

        EXTERNAL FF, D01AJF

        B0   = PARAM(1)
        BETA = PARAM(2)
C       Parameters describing the Gaussian opacity function.
        D00BAI = PARAM(3)
        DD = D00BAI * 4.184
C       Dissociation energy converted from kcal/mol to kJ/mol.
        Ebar = PARAM(4) * 4.184
C       PARAM(5) is the stationary reaction energy barrier in kcal/mol.
        RR = PARAM(5)
C       RR is the intermolecular distance in Angstrom at the saddle point.
C       PARAM(6) is related to an attractive potential ~ R^-6.

        DO 300 I = NSTART, NEND
        IXP = IND(I)
        J = DECTIM(I)
        E = DMAX1(EJ(J-.5)-DD, Ebar+(FACT/(RR*CF))**2*J*(J+1))
C       energetic limit in the product, barrier to reaction
C       Energies in kJ/mol.
        IF (E.GT.0) THEN
        Vmn = CF * SQRT(E)
        ELSE
        Vmn = 0
        ENDIF


        Vmn = DMAX1(Vmin(IXP), Vmn, PARAM(6)*(J*(J+1))**.75)
C       ,,(centrifugal barrier + attractive potential) highest value
        IF (Vmn.LT.Vmax(IXP)) THEN
        IFAIL = -1
        CALL D01AJF (FF,Vmn,Vmax(IXP),EPSABS,EPSREL,Y,
     X                   ABSERR,W,LW,IW,LIW,IFAIL)
        ELSE
        Y = 0
        END IF
        IF (MOD(I,NPT).EQ.0) PRINT 400, Vmn, J, DECDAT(I), Y
300     DECCAL(I-NSTART+1) = Y
400     FORMAT(' ',F7.1,2X,F5.1,2X,F9.2,2X,G12.5)
1000    END

        DOUBLE PRECISION FUNCTION FF(V)

        COMMON /BLK2/ FACT, CF
        COMMON /BLK3/ B0, BETA
        COMMON /BLK4/ J
        REAL*8 FACT, CF, V, FV, B, B0, BETA, PB
        REAL*4 J

        B = FACT * SQRT(J*(J+1)) / V
        PB = DEXP(-.5 * ((B-B0) / BETA)**2)
        FF = FV(V) * B * PB
        RETURN
        END

        DOUBLE PRECISION FUNCTION FV(V)

        PARAMETER N = 20000, NEXP0 = 20
        COMMON /SPLINE/ K(N), C(N), ICOUNT(NEXP0), IVSTART(NEXP0)
        COMMON /BLKFV / IXP
        REAL*8 V, K, C

        IFAIL = -1
        CALL E02BBF (ICOUNT(IXP), K(IVSTART(IXP)),
     X          C(IVSTART(IXP)), V, FV, IFAIL)
C       calculates the velocity probability density precalculated and
C       splined in START.

        RETURN
        END
*******************************************************************

        SUBROUTINE START

C       To be executed once at the beginning of the fitting program.
C       Calculates the relative velocity distribution and determines
C       spline coefficients for it.
C       Also calculates the relevant rotational and hence total internal
C       energy levels and subtracts D00(HI).

        PARAMETER EPSREL = 1.D-5, EPSABS = 1.D0, N = 20000
        PARAMETER LW = 2000, LIW = 500, LWRK  = 6 * N + 16
        PARAMETER Vmax0 = 1.5D3, N1 = 1000, Jmin0 = 2.5, JMAX0 = 700.5
        PARAMETER NEXP0 = 20, NDAT0 = 150, NN0 = NEXP0 * NDAT0

        COMMON /BLOCK1/ PARAM(40), ICON(40), NPARAM
        COMMON /BLOCK2/ DECDAT(NN0), DECTIM(NN0), IND(NN0), NDATA
        COMMON /BLOCK3/ NSTART, NEND, NUMBER
        COMMON /EXPVAR/ VAREXP(NEXP0,10), NXP
        COMMON /ENERGY/ EJ(700)
        COMMON /SPLINE/ K(N), C(N), ICOUNT(NEXP0), IVSTART(NEXP0)
        COMMON /BLK1/   V01, VS1, VS2, ALPH1, ALPH2, V
```

```
        COMMON /BLK2/   FACT, CF
        COMMON /BLK7/   Vmin(NEXP0), Vmax(NEXP0), VMP(NEXP0)

        REAL*8 PARAM, DECTIM, DECDAT, JMIN, JMAX, VAREXP, MR
        REAL*8 V01, VS1, VS2, ALPHA1, ALPHA2, ALPH1, ALPH2
        REAL*8 WRK(LWRK), K, C, VV(N), FFV(N), I0, DERF
        REAL*8 FINT, ABSERR, W(LW), NORM1, NORM2, NORMV
        REAL*8 EJ, DD, FACT, CF, V, E, Vmin, Vmax, VMP, FSOP
        REAL*8 F1, F2, GAMMA1, GAMMA2, GA1, GA2, ALPH
        DIMENSION IW(LIW)

        EXTERNAL F, D01AJF

        PARAMETER PI = 3.14159265358979D0, CC = 2.99792458D8
        PARAMETER KBOLTZMANN = 1.38054D-23, NAVOGADRO = 6.022045D+23
        PARAMETER HPLANCK = 6.62617D-34 ! c in m/s, k in J/K, h in J s.
        PARAMETER MBARIUM = 137.905, MIODINE = 126.9044
        PARAMETER MHYDROGEN = 1.007825 ! atomic masses in gr/mol.
        PARAMETER D00HI = 70.43 ! kcal/mol

        WRITE(7,800)
        PRINT 800

        MR = .001 / (1/MBARIUM + 1/(MHYDROGEN + MIODINE)) / NAVOGADRO
C       reduced mass of reactants in kg/molecule pair.
        FACT = HPLANCK / (2 * PI * MR) * 1.D10
        CF = DSQRT(2000 / (MR * NAVOGADRO))

        ILVXP = 0

        DO IXP = 1, NXP
        V01 = VAREXP(IXP,1)
        VS1 = VAREXP(IXP,2)
        ALPHA1 = VAREXP(IXP,3)
        VS2 = VAREXP(IXP,4)
        ALPHA2  = VAREXP(IXP,5)

        ALPH1 = ALPHA1 * ALPHA1
        ALPH2 = ALPHA2 * ALPHA2
        ALPH = 1/ALPH1+1/ALPH2
        VV1 = VS1 - V01
        A = .5 * ALPH1 * EXP(- VV1 * VV1 / ALPH1)
        B = .5 * ALPHA1 * DSQRT(PI) * (1 + DERF(VV1 / ALPHA1))
        I0 = VV1 * A + (.5 * ALPH1 + VV1 * VV1) * B
        NORM1 = 1 / I0
        NORM2 = 2./(ALPH2*VS2*DEXP(-VS2*VS2/ALPH2)+DSQRT(ALPH2*PI)*
     X  (ALPH2*.5+VS2*VS2)*(1+DERF(VS2/DSQRT(ALPH2))))
        NORMV = NORM1 * NORM2

        DO 100 I = 1, N1
        V = Vmax0 * I / N1
        VV(I) = V
        IF (V.GT.V01) THEN
        IF (VS2.GT.0) THEN
        CALL D01AJF (F,V01,V,EPSABS,EPSREL,FINT,
     X                   ABSERR,W,LW,IW,LIW,IFAIL)
        FFV(I) = FINT * V * NORMV
        ELSE
        GAMMA1 = -V/ALPH2-VS1/ALPH1
        GAMMA2 =  V/ALPH2-VS1/ALPH1
        GA1 = GAMMA1/DSQRT(ALPH)
        GA2 = GAMMA2/DSQRT(ALPH)
        F1 = GAMMA1*DEXP(GA1*GA1)*(1-DERF(GA1))
        F2 = GAMMA2*DEXP(GA2*GA2)*(1-DERF(GA2))
        FFV(I) = DEXP(-V*V/ALPH2) * (F2 - F1) * V
        END IF


        ELSE
        FFV(I) = 0
        END IF
100     CONTINUE

        DO 200 I = 1, N1
        IF (FFV(I).NE.0) GOTO 250
200     CONTINUE
250     I1 = I
        Vmin(IXP) = VV(I1)
        DO 300 I = I1 + 1, N1
        IF (FFV(I).EQ.0) GOTO 350
300     CONTINUE
        I2 = N1
        GOTO 360
350     I2 = I
360     Vmax(IXP) = VV(I2)

        NN = I2 - I1 + 1

        DO 370 I = 1, NN
        IF (FFV(I1 + I -1).GT.FVM) THEN
        IM = I
        FVM = FFV(I1 + I -1)
        END IF
        VV(I) = VV(I1 + I - 1)
370     FFV(I) = FFV(I1 + I - 1)
        VMP(IXP) = VV(IM + 1)
        WRITE(7,900) IXP, JIDNNT(Vmin(IXP)), JIDNNT(Vmax(IXP)), NN,
     X          JIDNNT(VMP(IXP))
        PRINT 900, IXP, JIDNNT(Vmin(IXP)), JIDNNT(Vmax(IXP)), NN,
     X          JIDNNT(VMP(IXP))

        IVSTART(IXP) = ILVXP + 1
        ICOUNT(IXP) = NN + 4
C       calculate spline coefficients for the relative velocity distribution.
        CALL E01BAF(NN, VV, FFV, K(IVSTART(IXP)), C(IVSTART(IXP)),
     X          NN+6, WRK, LWRK, IFAIL)
        ILVXP = IVSTART(IXP) + ICOUNT(IXP) - 1

        END DO

        JMIN = 1000
        JMAX = 0
        DO I = NSTART, NEND
        JMIN = DMIN1(JMIN,DECTIM(I))
        JMAX = DMAX1(JMAX,DECTIM(I))
        END DO

        WRITE(7,1000) JMIN, JMAX
        PRINT 1000, JMIN, JMAX

        IV = JIDNNT(VAREXP(1,6))
        DD = D00HI * 4.184
C       Dissociation energy in kcal/mol.

        CALL READDUN(IV,IV,0)

        DO 400 IJ = JMIN0-.5, JMAX0-.5
400     EJ(IJ) = FSOP(IJ+.5D0) * HPLANCK * CC * NAVOGADRO * .1 + DD
C       EJ(IJ) is internal energy of BaI + D00(HI) in kJ/mol.

800     FORMAT('0',11X,'JAYS3 : Using a gaussian for opacity function.',/)
900     FORMAT(' ',12X,'Experiment',I2,'. Relative velocity range : ',
     X  I4,' to ',I4,' m/s with ',I4,' points;  Vmp = ',I4,' m/s.')
1000    FORMAT('0',24X,'Data range between J = ',F5.1,' and J = ',
```

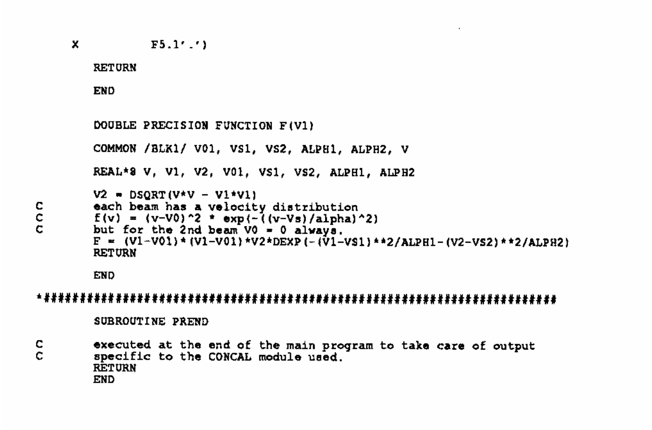

```
     X          F5.1'.')
        RETURN

        END


        DOUBLE PRECISION FUNCTION F(V1)

        COMMON /BLK1/ V01, VS1, VS2, ALPH1, ALPH2, V

        REAL*8 V, V1, V2, V01, VS1, VS2, ALPH1, ALPH2

        V2 = DSQRT(V*V - V1*V1)
C       each beam has a velocity distribution
C       f(v) = (v-V0)^2 * exp(-((v-Vs)/alpha)^2)
C       but for the 2nd beam V0 = 0 always.
        F = (V1-V01)*(V1-V01)*V2*DEXP(-(V1-VS1)**2/ALPH1-(V2-VS2)**2/ALPH2)
        RETURN

        END
*########################################################################

        SUBROUTINE PREND

C       executed at the end of the main program to take care of output
C       specific to the CONCAL module used.
        RETURN
        END
```